FROM SPIN-DRIVEN DIMERIZATION TO REDOX CHEMISTRY:

SPECTROSCOPIC STUDIES OF

NEUTRAL RADICALS AND PHOTOCATALYSTS

by

Anshu Kumar

_____

A Dissertation Submitted to the Faculty of the

DEPARTMENT OF PHYSICS

In Partial Fulfillment of the Requirements

For the Degree of

DOCTOR OF PHILOSOPHY

In the Graduate College

THE UNIVERSITY OF ARIZONA

2024

THE UNIVERSITY OF ARIZONA
GRADUATE COLLEGE

As members of the Dissertation Committee, we certify that we have read the dissertation prepared by: Anshu Kumar,
titled: From Spin-Driven Dimerization to Redox Chemistry: Spectroscopic Studies of Neutral Radicals and Photocatalysts

and recommend that it be accepted as fulfilling the dissertation requirement for the Degree of Doctor of Philosophy.

_____   Date: 06/17/2024
Vanessa Huxter

_____   Date: 06/17/2024
Arvinder Sandhu

_____   Date: 06/17/2024
John Schaibley

_____   Date: 06/17/2024
Leilei Peng

Final approval and acceptance of this dissertation is contingent upon the candidate's submission of the final copies of the dissertation to the Graduate College.

I hereby certify that I have read this dissertation prepared under my direction and recommend that it be accepted as fulfilling the dissertation requirement.

_____   Date: 06/17/2024
Vanessa Huxter
Dissertation Committee Chair
Assistant Professor of Chemistry

Acknowledgements

My journey has been filled with individuals and groups who have helped directly and indirectly. It is an impossible task to thank all of them for their influence and shaping my actions and thoughts. Without them, this thesis would not have been possible.

I would like to start by expressing my deepest gratitude to my advisor, Vanessa Huxter. Thank you for giving me an opportunity during the start of my graduate career, even though I did not have any background in experimental physics. I am incredibly grateful for your trust in me to work on challenging projects and for your invaluable insights during difficult times. Your expertise and passion have always motivated me. Working with you has been a great learning curve, teaching me how to be a good researcher beyond just being a good problem solver. I wish all the success and great research that will come to Huxter's lab in the future.

I am also deeply thankful to my committee members: Dr. Oliver Monti, Dr. Arvinder Sandhu, Dr. John Schaibley, and Dr. Leilei Peng, for their support, consideration, and invaluable guidance. My heartfelt thanks go to Lori Boyd for her time and assistance, your help has been indispensable. I would like to thank Dr. Mark Yanagihashi, the general chemistry lab manager, who helped me become a better mentor to my students with his wisdom and accommodating nature in times of need.

The work in this thesis would not have been possible without all the members of the Huxter group, particularly Dr. Alicia Swain, Benjamin Thompson, Grant Varun, and Laura Sawyer. I would like to thank Dr. Alicia Swain for being welcoming and introducing me to the experimental basics during my early graduate career. I will always cherish the memories of the times when we collaborated on difficult experiments; you being my lab partner made it easier. I want to thank Benjamin Thompson for our insightful discussions; it has been a pleasure working with you, and I know your work ethics will bring you lots of success. I would like to express my gratitude towards our collaborators: Gianneti Lab and Tomat Lab, who provided the molecules and compounds which I studied. I want to thank Dr. Aslam Shaikh and Mubarak Hossain, who were directly involved with the projects, and David Mills for helping me at times. This thesis would not have been possible without your help.

Land Acknowledgment

We respectfully acknowledge the University of Arizona is on the land and territories of Indigenous peoples. Today, Arizona is home to 22 federally recognized tribes, with Tucson being home to the O'odham and the Yaqui. Committed to diversity and inclusion, the University strives to build sustainable relationships with sovereign Native Nations and Indigenous communities through education offerings, partnerships, and community service.

Dedication

To Mummy, Papa, Didi, Soni,

who showed me to be gracious in adversity and supported me through it all.

To my wife, Daniela,

who gave me belief and been there through ups and downs.

To Manash, Subh and Arvi

you can achieve anything you set your heart to.

Table of Contents

List of Figures

11

List of Tables

List of Abbreviations

BBO	β-barium borate
MeCN	Acetonitrile
CS_2	Carbon disulfide
CCD	Charge-coupled device
TD1-Cu	Copper-hexaethyl tripyrrin-1,14-dione
DAS	Decay associated spectrum
ESA	Excited-state absorption
fs	Femtosecond
FROG	Frequency-Resolved Optical Gating
GSB	Ground state bleach
ISC	Intersystem crossing
IVR	Intramolecular vibrational redistribution
mJ	milijoule
^{n}Pr-DMQA$^{\bullet}$	N,N′-di-n-propyl-1,13-dimethoxyquinacridine
^{n}Pr-DMQA$^+$	N,N′-di-n-propyl-1,13-dimethoxyquinacridinium
DIPEA	N,N-Diisopropylethylamine
DMF	N,N-dimethylformamide
nm	Nanometer
NOPA	Noncolinear optical parametric amplifier
OAP	Off-axis parabolic

OPA	Optical parametric amplifier
PhB(OH)$_2$	Phenylboronic acid
PMT	Photomultiplier tube
ps	Picosecond
PG-FROG	Polarization gated frequency resolved optical gating
SNR	Signal-to-noise ratio
SAS	Species-associated spectra
SE	Stimulated emission
TCSPC	Time-Correlated Single Photon Counting
TA	Transient absorption
2DES	Two-Dimensional Electronic Spectroscopy
UV	Ultraviolet

Abstract

This thesis delves into the ultrafast photophysics of various photoredox catalysts and metal-ligand complexes, expanding our understanding of their dynamic behaviors and photophysical properties through meticulous optical spectroscopy studies. The core focus lies on the elucidation of complex electron and energy transfer mechanisms, which are fundamental to the application of these materials in photocatalytic processes and other relevant fields.

The study explores the temperature-dependent spin-driven dimerization in a copper(II)-bound tripyrrindione radical, TD1-Cu. It reveals that at low temperatures, TD1-Cu radicals undergo reversible dimerization, mediated by multicenter interactions and antiferromagnetic coupling between the unpaired electrons on the ligands. These insights into spin-coupled, temperature-controlled molecular dynamics offer potential applications in spintronics, molecular switches, and catalytic systems.

Further investigation focuses on a helical carbenium ion known as ^{n}Pr-DMQA^{+}, a red-light-activated organic photocatalyst, examining its role in the oxidative hydroxylation of phenylboronic acid. The longevity of the excited triplet state of ^{n}Pr-DMQA^{+} and the critical involvement of a sacrificial amine, DIPEA, in facilitating electron transfer processes highlight the capabilities of organic photocatalysts in sustainable chemistry under red-light activation.

Additionally, the research extends to the ultrafast dynamics of the ^{n}Pr-DMQA$^{•}$ radical, a stable neutral organic radical formed by reduction of the ^{n}Pr-DMQA^{+} cation. Through transient

absorption spectroscopy, the study delineates how the radical participates in rapid internal conversion processes. This work contributes significantly to our understanding of the stability and reactivity of organic radicals.

Overall, this thesis bridges significant gaps in our understanding of the fundamental properties of photoredox systems and lays the foundation for the development of novel photocatalysts. The methodologies and insights obtained pave the way for future innovations in photochemistry and photophysics, potentially revolutionizing approaches to sustainable and efficient photocatalytic applications.

Chapter 1:

Introduction and Thesis Perspective

1.1 Introduction

Neutral radicals, a fascinating class of molecules characterized by an unpaired electron on a non-ionic framework, occupy a unique position in the realm of atomic, molecular, and optical physics. These species, unlike their charged counterparts, maintain a neutral charge state while harboring an electron that is not engaged in bonding [1]. This unpaired electron imparts to neutral radicals a distinct set of properties, including high reactivity [2], anti-Kasha emission [2, 3] and the ability to engage in spin-dependent interactions [4-6], making them subjects of intense study within the scientific community. The significance of neutral radicals extends beyond their intriguing theoretical aspects; they find applications in a diverse range of fields, from materials science [7] to organic synthesis [8], facilitating novel pathways for the construction of complex molecular architectures through radical polymerization processes [9] and even in biological systems [10]. Additionally, neutral radicals have been employed in the design of molecular magnets, where the manipulation of spin states and coupling interactions can lead to materials with desirable magnetic properties, relevant for data storage technologies [11, 12].

Metal-bound radical systems garner attention for their prowess in electron transfer processes [13], thereby facilitating chemical reactivity. These systems are pivotal in numerous functions, from biological processes [14-19] to polymerization [13, 20, 21]. Transition metal complexes with organic ligands have found extensive application in photoredox catalysis [22-24], offering a pathway to facilitate complex chemical reactions under mild conditions through the generation of highly reactive radical species upon light absorption. Recently, a radical metal-ligand copper-hexaethyl tripyrrin-1,14-dione (TD1-Cu) complex was reported which is stable at ambient conditions and can be produced on milligram scale [3, 25-27]. This remarkable complex boasts a

non-innocent ligand which participate in redox chemistry [25, 28], featuring an electron-rich planar π system with pyrrolic nitrogen donors capable of redox chemistry, forming a coordination complex with a copper (II) metal center. Notably, TD1-Cu hosts two unpaired electrons, one within the π system of the ligand and another residing in the d-orbital of the copper center, rendering it a stable radical under ambient conditions [26]. Part of the work presented in this thesis explores the unique spin-interaction effect in TD1-Cu complex as a function of temperature.

Since the landmark discovery of stable organic radicals by Moses Gomberg in the early 20th century [29], these enigmatic species have captured the attention of researchers, owing to their intriguing chemical structure characterized by unpaired electrons [30, 31]. Beyond their fundamental significance, organic radicals have exhibited remarkable potential across various applications, including radical polymerization initiation [32], radical batteries [33, 34], and materials showcasing two-photon absorption properties [35-37]. Concluding this introduction, our exploration also pivots to the realm of open-shell doublet organic radicals. These radicals are generally produced in-situ, leveraging either electrochemical [38, 39] or photochemical [40] means. This innovative generation process transforms a closed-shell singlet precursor into an open-shell doublet organic radical. Upon photoexcitation, this radical transitions into an excited state which boasts exceptional capabilities as a potent photoreducing agent [41]. Central to the discussions within this thesis is an in-depth examination of a unique photocatalytic duo: the closed-shell singlet species, N,N′-Di-n-propyl-1,13-dimethoxyquinacridinium (^{n}Pr-DMQA^{+}), and its corresponding reduced doublet radical form, N,N′-di-n-propyl-1,13-dimethoxyquinacridine (^{n}Pr-DMQA${}^{\bullet}$), both entities serve as potent photocatalysts [42, 43].

As we proceed, the remainder of Chapter 1 will delve into the sophisticated optical tools and methodologies instrumental in elucidating the excited-state dynamics of these molecular systems. The ultrafast spectroscopic instruments employed in this study are not only home-built but also require meticulous maintenance and calibration to meet the specific demands of each research project. Instrumentation automation has been handled using LabVIEW, ensuring precision and efficiency in data acquisition.

1.2 Steady-State Spectroscopy

1.2.1 Absorption

Absorption spectroscopy is a fundamental optical technique used to study the interaction between electromagnetic radiation and matter. It measures the amount of light absorbed by a sample as a function of wavelength or frequency, providing essential information about the electronic and structural properties of molecules. In steady-state absorption spectroscopy, the absorption spectrum obtained reflects the population of molecules in the ground state absorbing light and transitioning to various excited states under equilibrium conditions. This method offers invaluable insights into the electronic structure, energy levels, and transition probabilities of molecules, serving as a cornerstone in the photophysical characterization of chemical species.

Figure 1.1 shows an example of the absorption spectrum for ^{n}Pr-DMQA$^+$ cation in solvent mixture of ethanol and methanol. The intensity of absorption peaks in a spectrum is intrinsically linked to the "transition dipole moment", a vector quantity that describes the probability of a transition between two states. The transition dipole moment is a measure of the molecule's ability

to absorb light at a particular wavelength, correlating directly to the oscillator strength of the transition. A large transition dipole moment between ground state and higher lying states correlates to a higher oscillator strength, which in turn increases the absorption cross-section and the intensity of the absorption peak. This principle is crucial in understanding the absorption behavior of molecules like the ^{n}Pr-DMQA cation and radical systems, where specific transitions between ground and excited states dominate the absorption spectrum.

While absorption spectroscopy provides a wealth of information about allowed electronic transitions, certain states that are optically not allowed, or "forbidden," do not appear in the absorption spectrum. Despite their invisibility in these spectra, these states can play a critical role in the relaxation pathways of molecules, offering alternative routes for the dissipation of excited-state energy. For example, in the case of the ^{n}Pr-DMQA$^+$, the work presented in this thesis highlights transitions to optically forbidden triplet states due to spin selection rule might contribute to its photophysical behavior and excited-state dynamics, influencing its relaxation processes and photocatalytic efficiency.

In conclusion, absorption spectroscopy serves as a powerful tool for probing the electronic structure and photophysical properties of molecules like the ^{n}Pr-DMQA cation and radical. By understanding the principles underlying absorption peaks, transition dipole moments, and the role of both optically allowed and forbidden states, one can gain insights into the mechanisms governing light-matter interactions, laying the groundwork for advances in photophysics and photocatalysis.

1.2.2 Fluorescence
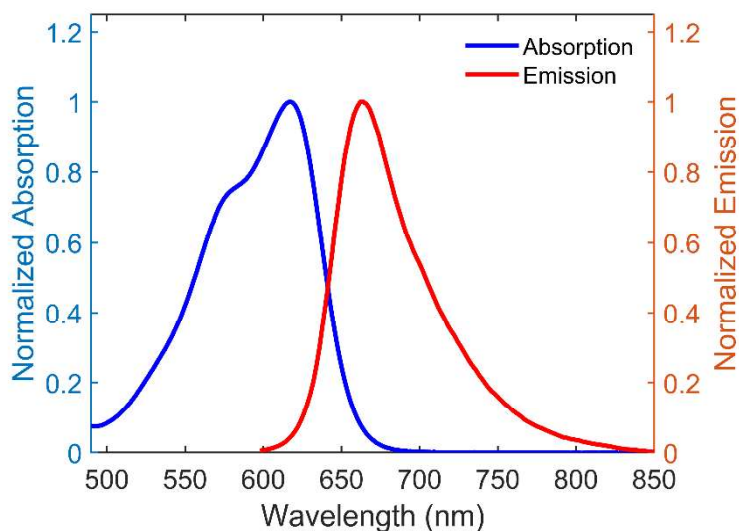
Figure 1.1: Representative absorption and emission spectrum of ^{n}Pr-DMQA^{+} cation at room temperature, in solution with ethanol and methanol in 4 to 1 v/v ratio. Absorption is presented by the blue trace while emission is shown in red.

Photoluminescent or fluorescence spectroscopy stands as a pivotal analytical tool in the realm of physical chemistry. This technique, by measuring the spectrum of light emitted by a sample upon excitation, plays a crucial role in assessing radiative pathway as well as inferring the presence of non-radiative routes. Specifically, in cases where a sample supposed to be non-emissive is contaminated with radiative impurities, emission spectroscopy can detect these anomalies to gauge sample purity. The exceptional sensitivity of fluorescence emission enables a range of distinctive applications and detection techniques, from experiments involving individual molecules [44] to the study of energy transfer processes [45].

Fluorescence spectroscopy provides important information about a molecule radiative state. Figure 1.1 shows emission from ^{n}Pr-DMQA$^+$ cation when dissolved in ethanol-methanol solvent mixture. This emission spectrum is collected by exciting a sample at one wavelength where it absorbs (λ_{ex} = 590 nm for emission trace in Figure 1.1) and collecting photons emitted due to fluorescence at different wavelengths to build an intensity vs wavelength plot. The associated excitation spectrum, obtained by keeping the detection wavelength fixed and scanning over the excitation wavelengths, reveals the various electronic transitions that the molecule can undergo, thereby providing a window into its energy levels that feed the lowest lying excited state [46]. Generally, excitation spectra closely mirror absorption spectra and is associated with the absorption of the emitting state. The intensity and position of the emission peaks can also shed light on the molecule's environment, such as solvent effects, and the presence of intermolecular interactions, offering clues about its behavior in different settings.

In essence, emission spectroscopy is a powerful technique that not only aids in the characterization and potential purity assessment of materials but also provides indispensable insights into the photophysical and photochemical properties of molecules, particularly photocatalysts, enabling the development of more efficient and selective catalytic processes.

1.3 Ultrafast Spectroscopy

Ultrafast spectroscopy, a pivotal tool in the arsenal of atomic, molecular, and optical physics, encompasses a range of techniques designed to probe the dynamics of molecules on femtosecond (10^{-15} s) to nanosecond (10^{-9} s) timescales and beyond. This enables the observation of fundamental

processes occurring at the speed of chemical reactions and the flow of energy within and between molecules. By capturing these fleeting moments, ultrafast spectroscopy offers unparalleled insights into the mechanistic underpinnings of complex systems, from elucidating the pathways of energy transfer and electron dynamics in molecular structures to unraveling the intricacies of spin manipulation. These insights are not merely academic; they have profound implications for the development of advanced materials, better photocatalysts, and innovative devices that leverage the principles of quantum dynamics. Through its ability to dissect the transient states and transitions that govern the behavior of molecules, ultrafast spectroscopy stands as a cornerstone in the quest to engineer the next generation of technological advancements.

1.3.1 Pulse Characterization

Pulse characterization holds paramount importance in the domain of ultrafast spectroscopy, enabling us to precisely understand and manipulate the temporal and spectral properties of ultrafast laser pulses. This knowledge is critical for optimizing the resolution and sensitivity of spectroscopic measurements, thereby unraveling the dynamics of molecular systems on femtosecond timescales. A common method for pulse compression, which is vital for achieving the shortest possible pulse durations, involves the use of a prism compression line. As detailed in previous work from our research group [47], this technique allows for the adjustment of pulse dispersion, compensating for the broadening effects inherent in pulse generation and propagation, thus sharpening the pulse for enhanced spectroscopic applications. Furthermore, pulse characterization often employs frequency doubling through β-barium borate (BBO) crystals. This process not only serves to estimate the temporal resolution of the pulse but also plays a crucial role

in determining the "time zero" – a reference point essential for accurate time-delay measurements in dynamic spectroscopic studies.

Additionally, an effective strategy for pulse characterization involves conducting frequency-resolved transient absorption (TA) measurements on non-resonant materials like fused silica or carbon disulfide. This approach, coupled with Frequency-Resolved Optical Gating (FROG) techniques, allows for the comprehensive retrieval of pulse parameters. FROG provides detailed information on the pulse's phase, along with its temporal and spectral profiles, offering a complete picture of the pulse's characteristics. Such detailed pulse analysis is indispensable for fine-tuning ultrafast spectroscopic experiments, ensuring the accurate capture of ultrafast processes. In summary, pulse characterization is essential to ultrafast spectroscopy, enabling the detailed examination of molecular dynamics with unprecedented precision.

1.3.2 Time-Correlated Single Photon Counting

Time-Correlated Single Photon Counting (TCSPC) is a powerful technique used to measure the time-resolved emission properties of fluorescent molecules [48]. It offers valuable insights into the dynamics of excited states, particularly their radiative lifetimes, by recording the time delay between a light pulse exciting the sample and the subsequent emission of a photon. This data enables the construction of decay curves that can be analyzed to determine lifetimes, providing critical information about the photophysical and photochemical processes of the molecule under study [49, 50]. TCSPC is particularly useful in studying photoredox catalysts that exhibit fluorescence, allowing researchers to explore their excited-state dynamics and understand their mechanisms of action. The ability to resolve fluorescence decay over time is essential in dissecting

the pathways and kinetics of such catalysts, which are often central to various chemical reactions and applications and has been highlighted in Chapter 3 where change in radiative lifetime of ^{n}Pr-DMQA^{+} has been associated with its role as a photocatalyst.
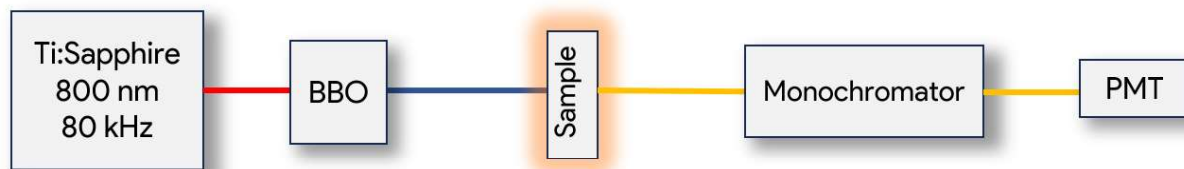
Figure 1.2: Simplified schematics of TCSPC.

In our laboratory, TCSPC measurements begin with a NIR Ti:Sapphire oscillator (Vitara-T, Coherent), generating sub-100 femtosecond pulses at 800 nm with a repetition rate of 80 MHz. These pulses are not optimal for directly exciting most organic molecules, as their absorption peaks generally lie at higher energies. To remedy this, the 800 nm pulses are frequency-doubled using a type I BBO crystal, producing 400 nm pulses. This wavelength is well-suited for exciting a variety of organic molecules, as they have some absorption in this region, and excited state radiative lifetime is independent of the excitation wavelength [46] while organic solvents usually absorb at even higher energies. The 400 nm pulse is then directed into a quartz cuvette containing the sample, with a typical path length of 0.5 to 2 mm. The fluorescence emitted from the sample is collected by a pair of 90-degree off-axis parabolic (OAP) mirrors. These mirrors collect, collimate, and focus the fluorescence efficiently, making the most of the emitted light that radiates in all directions. The 90-degree arrangement of the mirrors aids in separating the excitation pulse from the collected fluorescence signal. The fluorescence is then guided through an afocal system, which

focuses it onto the entrance slit of a monochromator. This monochromator is connected to a photomultiplier tube (PMT), which detects the fluorescence signal. The monochromator serves to filter out stray wavelengths, ensuring that only the intended fluorescence wavelengths reach the detector. Additionally, reflective neutral density filters are used to modulate the intensity of the fluorescence signal before it enters the monochromator, preventing saturation of the sensitive PMT detector.

In summary, TCSPC is a crucial technique for studying the dynamics of fluorescent molecules, offering precise measurements of excited-state radiative lifetimes and insights into photophysical and photochemical pathways. In our laboratory, a sophisticated setup involving a Ti:Sapphire laser, a BBO crystal, and a PMT enables detailed analysis of fluorescence decay curves, particularly for photoredox catalysts and organic molecules. The results from TCSPC measurements can complement other ultrafast measurements such as transient absorption (TA) in developing a complete understanding of intricate mechanisms underlying various chemical reactions and processes as illustrated in Chapter 3.

1.3.3 Transient Absorption

Transient absorption (TA) spectroscopy is a powerful technique for investigating the dynamic processes that occur in molecules following photoexcitation. This method provides an "ultrafast snapshot" of excited-state lifetimes, reaction intermediates, and photoinduced electronic and structural changes, thereby offering a comprehensive picture of molecular dynamics on timescales ranging from femtoseconds to nanoseconds and beyond. TA spectroscopy can reveal details about various types of signal contributions, such as ground state bleach (GSB), stimulated emission (SE),

and excited-state absorption (ESA), each providing unique insights into the photophysical and photochemical pathways of the system under study. GSB occurs when photoexcitation depopulates the ground state, leading to a reduced absorption at wavelengths corresponding to transitions from the ground state. SE reflects the emission of photons as an excited state relaxes radiatively to the ground state, typically appearing at wavelengths corresponding to the emission spectrum. ESA represents absorption of photons by molecules in excited states, leading to transitions to higher electronic states. A thorough understanding of these contributions and their meanings is critical for dissecting complex photoreactions. The methodology for global and targeted analysis of time and frequency-resolved spectra, as reviewed by Van Stokkum et al., [51] is indispensable for extracting and interpreting the wealth of information contained within TA spectroscopy data, offering a model-based analysis approach that combines kinetic schemes and spectrotemporal models to describe complex system dynamics concisely.
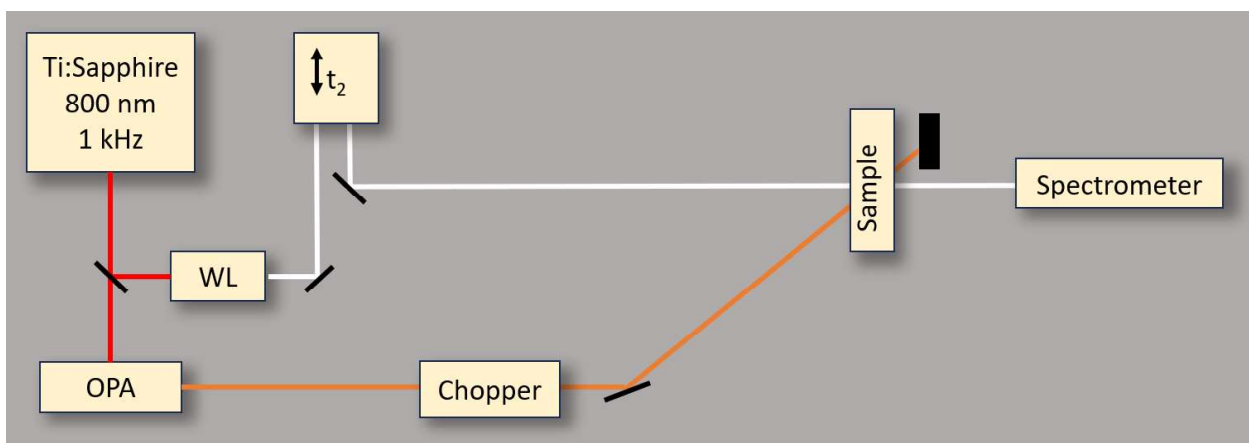
Figure 1.3: Simplified schematics of TA setup with white light probe.

In our laboratory, the TA spectroscopy setup is designed to capture these dynamic processes with high precision. The setup begins with a source, typically a visible or NIR laser system. We employ an optical parametric amplifier (OPA) to generate the pump pulses, while the probe pulses are created via self-focusing in an argon-filled tube to produce broadband white light. This configuration ensures a high-intensity pump to effectively initiate the photoexcitation process, whereas the probe remains sufficiently weak to avoid perturbing the sample further. The temporal delay between pump and probe pulses is achieved using a mechanical translation stage along the probe line, ensuring precise control over the timing of the interactions.

A crucial component of our setup is the pulse shaper, which acts as a chopper to alternately allow and block the pump beam from interacting with the sample. This mechanism is critical for acquiring differential measurements that form the basis of the TA signal. The pump and probe beams are focused at the sample position at a slight angle to ensure overlap at a single focal point, with the probe beam having a slightly smaller waist at the focal plane for optimal spatial overlap.

Determining "time zero" — the point at which the pump and probe lines length coincide — is achieved via cross-correlation measurements. This step is vital for accurately mapping the dynamics observed in the TA spectra to real-time processes. After interacting with the sample, the pump beam is blocked, and the probe beam is directed towards the spectrometer using a series of flat mirrors and a concave mirror to focus the beam into the entrance slit. This routing ensures that the beam is focused into the spectrometer and careful attention is paid to prevent CCD (charge-coupled device capable of photon detection and converting them to electronic impulses) saturation or damage by appropriately adjusting the beam intensity.

The spectrometer plays a pivotal role in performing frequency-resolved TA measurements, allowing for the separation of the various spectral components of the probe pulse after it has interacted with the sample. To minimize scatter and ensure accurate measurements, our lab incorporates several strategies, such as using a mask to contain the pump beam and set of irises around the probe beam to exclude scatter contributions. Additionally, the use of flat mirrors at right angles helps to further reduce scatter, ensuring that only the relevant signal reaches the CCD.

In summary, transient absorption spectroscopy provides invaluable insights into the ultrafast processes that govern the behavior of molecules in excited states. Through careful design and implementation of TA spectroscopy setups, combined with sophisticated global and targeted analysis techniques, researchers can unravel the complex dynamics of molecular systems with unprecedented detail. The ability to probe these dynamics sheds light on fundamental photophysical phenomena, offering pathways to the rational design of more efficient photocatalysts, materials, and devices based on the principles of molecular excited-state processes.

1.3.4 Two-Dimensional Electronic Spectroscopy

Two-Dimensional Electronic Spectroscopy (2DES) has emerged as a revolutionary ultrafast spectroscopic tool, playing a crucial role in dissecting the complex dynamics of electronic states within molecular systems. Its importance lies in its unique capability to elucidate the couplings between electronic states and to discern the contributions of different dynamic processes to the spectral lineshape, as highlighted by Fuller and Ogilvie [52]. The correlation maps generated at various population times provide profound insights into the energy transfer processes, revealing how excitation energies evolve and how states interact over time. The field has seen considerable

advancements since its first successful demonstration by the Jonas group in 1998 [53], marking

the onset of significant developments in multidimensional electronic spectroscopy [54-67].
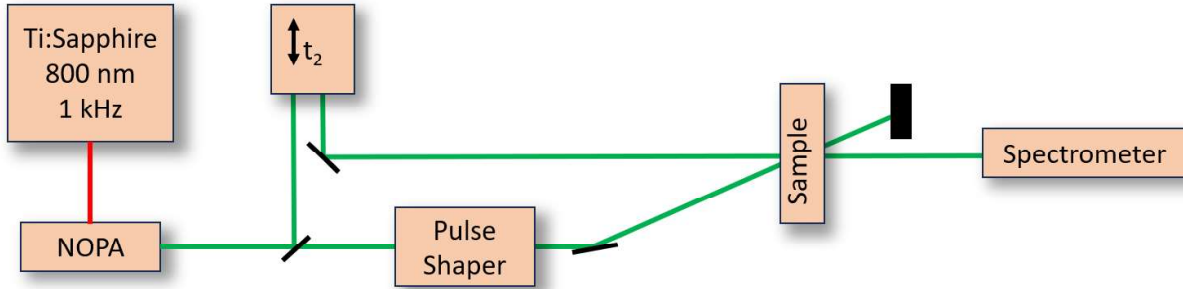
Figure 1.4: Simplified schematics of pump-probe geometry 2DES.

In our laboratory, 2DES is performed using a pump-probe geometry, an extension of the

transient absorption setup previously discussed, often referred to as pump-probe 2DES. This

method has been instrumental in the investigations presented in Chapter 2 of this thesis. A pivotal

component of our setup is the pulse shaper (see Sec. 1.3.3), which introduces a controllable time

delay between the first two light-matter interactions. This time delay is crucial as it is Fourier

transformed to generate the excitation frequency axis, providing a detailed correlation map in

2DES experiments. However, the pulse shaper's drawback includes a loss of power, which is

wavelength dependent and typically sees efficiencies below 40%. Moreover, the physical

dimensions of the birefringent crystal within the shaper limit the spectral bandwidth that can be

manipulated, as well as imposing specific polarization requirements on the pulses.

Phase cycling is an essential technique in pump-probe 2DES, employed to eliminate unwanted background signals and isolate the crucial information regarding the electronic transitions within the sample. Phase cycling, analogous to 2D NMR [68], involves varying the phases of consecutive pump pulses, allowing for constructive and destructive interference of different signal components, thus enabling background signals to be selectively canceled out. Through multiple phase cycling schemes significant signal-to-noise ratio (SNR) improvements can be achieved [69, 70]. By collecting multiple traces for the same coherent time delay with varying relative phases between the collinear pump pulses, one can effectively isolate the desired signals. We applied phase cycling scheme as described by Ogilvie et al [62] with two phases of 0 and $\pi/2$ between the pump pulses to effectively cancel out the extraneous signals and isolate relevant ones along with access to rephasing and nonrephasing signal contributions.

The 2DES correlation map plot may feature diagonal and cross-peaks. These peaks are indicative of strong electronic and/or vibronic coupling within the system. Notably, the signs of the signal contributions, as discussed in Sec. 1.3.3 namely ground state bleach (GSB), excited state absorption (ESA), and stimulated emission (SE), in 2DES are opposite to those observed in transient absorption (TA) spectroscopy. The resolution along the excitation axis offered by 2DES enables the recovery of individual contributions that are averaged in transient absorption (TA) measurements. In a TA experiment, the trace collected at a given population time corresponds to an integrated signal along the excitation axis of the 2DES plot at the same population time, resulting in an averaged response along the detection axis. This was particularly evident in the findings presented in Chapter 2, where 2DES provided unparalleled resolution in unraveling the intricate dynamics of TD1-Cu system which were hidden in TA measurements.

1.4 Outline of the Thesis

This thesis delves into the intricate dynamics of novel molecular systems and their catalytic processes through the lens of ultrafast spectroscopy, unveiling the pivotal role of electronic states, spin interactions, and solvent effects. Each chapter is structured to progressively build upon the fundamental understanding of these systems, leveraging advanced spectroscopic techniques to provide comprehensive insights into their behavior and mechanisms.

Chapter 2 explores the ultrafast properties of a stable neutral radical system, Cu(II) hexaethyl tripyrrin-1,14-dione (TD1-Cu), which exhibits temperature-dependent spin-tunable properties. This unique molecular complex, characterized by unpaired electrons localized on both the copper center and the tripyrrolic ligand, showcases switchable temperature-dependent spin coupling. Employing 2DES, the study investigates the system at room temperature, where monomeric forms predominate with short picosecond lifetimes, and at 77 K, were ferromagnetic and antiferromagnetic coupling mediate dimerization. This spin-driven reversible dimerization alters the optical properties, creating long-lived excitonic states, thus providing valuable insights into the interplay between spin interactions and molecular dynamics.

Chapter 3 focuses on the ultrafast study of a novel organic photocatalyst, N,N′-Di-n-propyl-1,13-dimethoxyquinacridinium (^{n}Pr-DMQA$^+$), through TA and TCSPC spectroscopy. This investigation sheds light on the optical properties of ^{n}Pr-DMQA$^+$ and elucidates the role of its triplet state in the catalytic process. The study reveals how the excited state cation captures an electron from an amine to form its reduced radical, which subsequently interacts with an oxygen molecule to generate the superoxide anion. This superoxide anion then reacts with arylboronic

acid, leading to the formation of aromatic alcohol after hydrolysis, thus uncovering the mechanistic pathways underpinning the photocatalytic activity of ^{n}Pr-DMQA^{+}.

Chapter 4 presents an ultrafast spectroscopic study of the reduced radical form of ^{n}Pr-DMQA^{+}, characterized by an additional electron on the central carbon. Employing TA, this chapter highlights the picosecond decay lifetime of the excited state, consistent with behaviors observed in other organic radicals. A notable finding is the radical's response similarity in polar and nonpolar solvents, with slightly longer excited state lifetime in the nonpolar solvent environment. This observation underscores the negligible influence of solvent polarity on the dynamics and stability of radical species.

Chapter 5 concludes the thesis with a summary of the key findings and implications of the research presented. This chapter synthesizes the insights gained from studying the dynamic behaviors and catalytic processes of TD1-Cu and ^{n}Pr-DMQA systems. It paves the way for further characterization of ^{n}Pr-DMQA^{+}'s catalytic processes and explores potential pathways by which ^{n}Pr-DMQA$^{\bullet}$ might manifest extreme reduction chemistry [43], thus setting the stage for advancing our understanding of catalysis and radical chemistry.

Each chapter of this thesis contributes to the broader knowledge of molecular dynamics, catalysis, and radical chemistry, offering a scaffold for future investigations into the fundamental processes governing the behavior of complex molecular systems.

Chapter 2:

Temperature-Dependent Spin-Driven Dimerization Determines the Ultrafast Dynamics of a Copper(II)-Bound Tripyrrindione Radical

2.1 Chapter Summary

Chapter 2 explores the ultrafast dynamics of the TD1-Cu complex, a novel system where spin-driven dimerization modulates photophysical properties across different temperatures. Employing two-dimensional electronic spectroscopy, this study reveals how temperature influences the complex's transition from a monomeric to a dimeric state, highlighting the significant differences in the excited state lifetimes. The insights from this chapter enhance our understanding of metal-ligand interactions and their implications for catalysis and redox processes, laying a foundational role in the thesis by linking molecular structure to dynamic photophysical behavior.

2.2 Introduction

Metal-bound radical systems are of particular interest for their ability to perform electron transfer and to enable chemical reactivity. They participate in a wide range of biological processes including photosynthesis and enzyme catalysis. For example, the oxidization of alcohols by the fungal enzyme galactose oxidase is facilitated by a combination of a copper metal center and a tyrosine radical cofactor [14, 15]. In natural light harvesting, the oxidation of chlorophyll, a macrocyclic chlorin with phytyl chain bound to a magnesium metal center, generates a cationic radical that enables water splitting [16-19]. Complexes consisting of a transition metal center bound to organic ligands have been widely used in photoredox catalysis [22-24]. Following optical excitation, these systems can form highly reactive radicals that permit challenging chemical transformations without the use of harsh conditions.

In this paper we present the ultrafast dynamics of a stable neutral radical complex featuring both a ligand-based and a metal-based unpaired spin: a hexaethyl tripyrrin-1,14-dione radical bound to a Cu(II) center (i.e., [Cu(TD1$^{\bullet}$)(H$_2$O)], abbreviated TD1-Cu) [3, 25-27]. This configuration is unusual and allows for the direct investigation of novel spin-mediated dynamics and interactions. The square planar TD1-Cu complex, shown in Figure 2.1(a), features a monodentate aqua ligand and a tridentate tripyrrindione, with an electron-rich planar π system capable of reversible one-electron oxidation and reduction chemistry that is of interest for catalytic and redox sensing applications. The neutral radical TD1-Cu complex has one unpaired electron formally in the π system of the tripyrrindione ligand and a second unpaired electron associated with the d^9 copper center. These unpaired spins are in near-orthogonal orbitals, resulting in an overall triplet ground state [26].
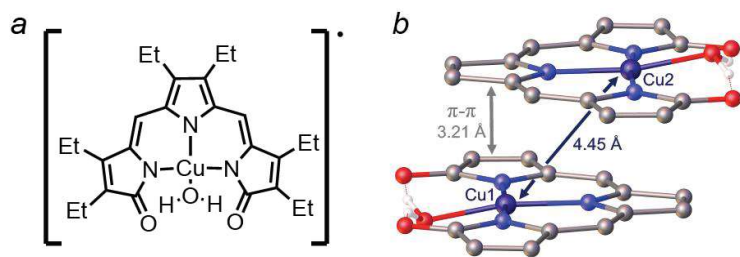
Figure 2.1: (a) Structure of TD1-Cu (i.e., [Cu(TD1•)(H2O)]) and (b) selected metrics of a representative π dimer observed in the crystal structure (CCDC 1496214). Carbon-bound hydrogen atoms and ethyl substituents are omitted for clarity.

Recently, our group reported the ultrafast dynamics of TD1-Cu at room temperature using transient absorption spectroscopy. These studies showed that the lifetime of the excited state of the monomer biradical form of TD1-Cu was sub 20 picoseconds [71]. At low temperature, metal-bound tripyrrindione radicals reversibly form π stacked dimers, as shown in Figure 2.1(b), mediated by multicenter interactions (also described as pancake bonding [72, 73]) and antiferromagnetic coupling between the unpaired electrons on the ligands [26, 74, 75]. Here we use time-resolved ultrafast spectroscopy to show that the formation of a spin-coupled dimer changes the electronic dynamics. In this paper we use temperature-dependent two-dimensional electronic spectroscopy (2DES) to observe ultrafast dynamics of TD1-Cu in its monomeric and dimeric forms. These measurements show that TD1-Cu forms excitonic dimers with long-lived excited states at low temperatures compared to the short excited-state lifetime of the room temperature radical monomer.

2.3 Result and Discussion
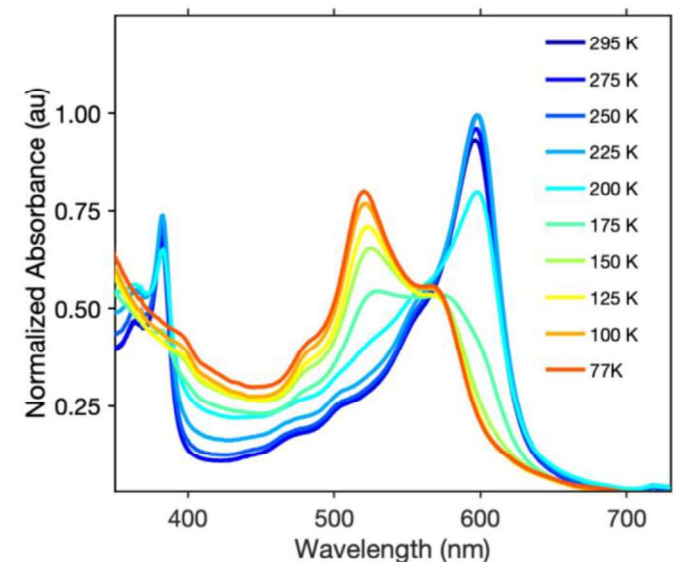
Figure 2.2: Steady-state absorption of TD1-Cu in a 6:1 v/v methylcyclohexane-toluene mixture, illustrating the temperature-dependent changes from 295 K to 77 K.

Figure 2.2 shows the temperature-dependent absorption spectrum of TD1-Cu in a methylcyclohexane:toluene mixture (6:1 volume ratio) from 295 K to 77 K. The steady-state absorption spectra were collected using an Agilent Cary 100. No fluorescence was observed for TD1-Cu in the monomer or the dimer form. In our previous work on TD1-Cu, we did not observe any fluorescence at room temperature for either the neutral radical or the oxidized species [71]. The lack of fluorescence in TD1-Cu is unsurprising due to the existence of low-lying states that allow relaxation via radiationless transitions (energy gap law) [76-78]. These low-lying states with very small oscillator strengths are characteristic of ligand-based radicals of oligopyrrole complexes and appear in the near IR region (see Figure 2.6 in the Supporting Information).

44

The 295 K absorption spectrum displays a prominent band in the visible region at 600 nm. These transitions originate from π to π^* transitions [71] localized on the tripyrrindione ligand. As the temperature is lowered, the primary absorption peak in the visible shifts from 600 nm to 521 nm. This change in the absorption spectrum is associated with the formation of a dimer at low temperatures enabled in part by interactions between the unpaired electrons. In the monomer, the unpaired electron on the metal center is localized in the dx$_2$-y$_2$ orbital, which is near orthogonal to the ligand's π orbitals that accommodate the other unpaired electron [26, 71], stabilizing the triplet ground state. Upon lowering the temperature, TD1-Cu undergoes a reversible dimerization process facilitated by antiferromagnetic coupling between the electrons localized on the ligand as well as ferromagnetic interactions between the electrons localized on the Cu(II) metal centers [26]. The presence of an isosbestic point implies the existence of two interconverting equilibrium populations and is representative of the conversion of the monomer to the dimer. The peaks in the near-IR (Figure 2.6 in the Supporting Information) also shift and display isosbestic points consistent with dimerization involving a change in the local environment of the ligand-based electron. Upon freezing into a glass, the scatter from the sample increases slightly, leading to a small amount of uncertainty in the isosbestic point.

The temperature-dependent absorption data was used to determine thermodynamic parameters for the dimerization process in the methylcyclohexane-toluene mixture. Assuming that the monomer and the dimer are the primary contributions to the absorption at 295 K and 77 K respectively, relative absorption intensities were used to determine values for equilibrium constants and ΔG at different temperatures (additional information in Section 3 of the Supporting Information). The temperature dependence of ΔG (Figure 2.8 in the Supporting Information) was

used to determine dimerization enthalpy and entropy changes. The values obtained, $\Delta H = -4.07 \pm 0.08$ kCal/mol and $\Delta S = -21.9 \pm 0.3$ Cal/mol·K, are consistent with previously published values [26]. Both ΔH and ΔS are negative, indicating that dimerization is spontaneous at low temperatures. The temperature at which ΔG switches from positive to negative is approximately 185 K. This is consistent with our steady-state absorption spectra, which show a significant change between the 200 K and 175 K traces.

Figure 2.3 (a)–(f) presents several representative 2DES spectra of TD1-Cu at room temperature. These spectra were acquired using a laser pulse centered at 600 nm, covering a spectral range of 570 nm to 633 nm. A brief description of the experimental setup is provided here (additional details can be found in Section 2.5.3 of the Supporting Information). The 2DES measurements were collected using a home-built femtosecond pump-probe geometry 2DES setup. A 1kHz regenerative-amplifier laser system, Coherent (Libra), was used to power a home-built single-pass noncolinear optical parametric amplifier (NOPA). The NOPA output was compressed using a prism compression line and later split to generate pump and probe pulses. The pump pulse was passed through a pulse shaper, FASTLITE Dazzler, to provide controllable variable time delay between two collinear pump pulses. This delay between the two pump pulses is called t_1 or the coherence time, and the delay between the pump pulses and the probe is called t_2 or the population time. The spot size of the pump and probe beams at the sample position was approximately 80 µm. The NOPA output was centered at 600 nm and 529 nm for the room temperature (295 K) and 77 K measurements respectively (see Supporting Information). Second harmonic generation signal generated with a BBO revealed a temporal width of sub-45 fs and sub-40 fs for the pulses used for the room temperature and 77 K measurements, respectively, which was complemented by

polarization gated frequency resolved optical gating (PG-FROG) using a non-resonant sample (see Figures 2.9 and 2.10 in the Supporting Information). After the sample position, the probe was focused onto a spectrometer (SpectraPro HRS-300) and detected on a CCD (PIXIS 400, Princeton Instruments). The detection frequency axis collected using the CCD corresponds to the λ_3 axis in the 2DES plots, the λ_1 axis is generated from the Fourier transform of the delay between the pump pulses t_1. Each 2DES plot corresponds to a single point along the population time, t_2 [52, 79]. Additional experimental details for the 2DES measurements can be found in the Supporting Information.

In Figure 2.3, the strong feature that appears on the diagonal at 600 nm in panel (a) is associated with a ground state bleach (GSB) of the primary π to π^* transition shown in the room temperature (295K) absorption spectrum (Figure 2.2).
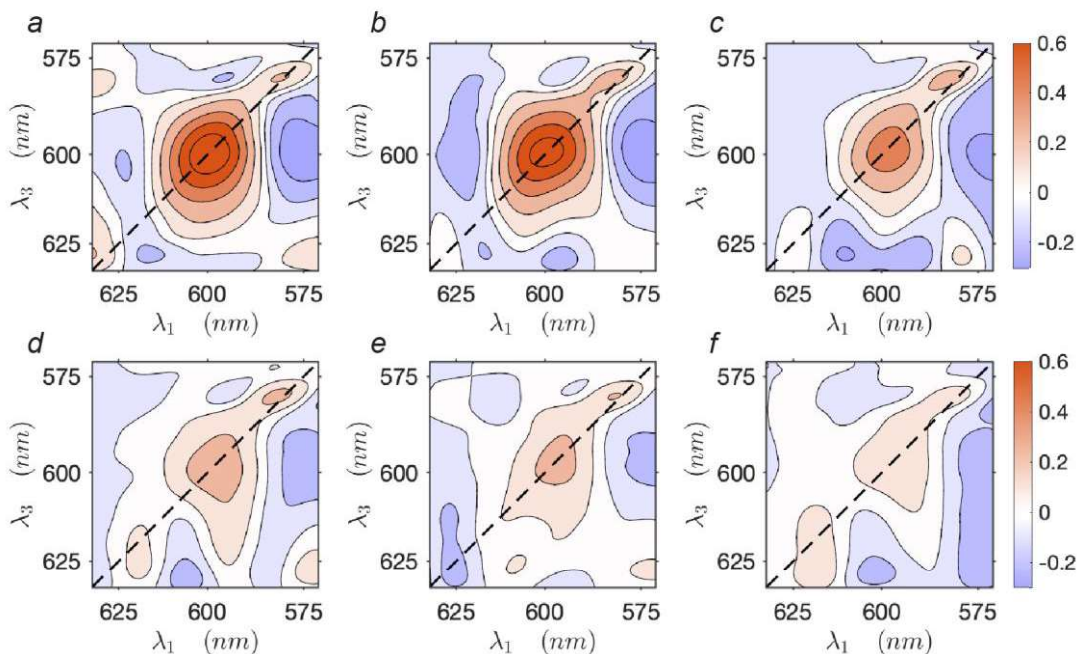
Figure 2.3: Representative absorptive 2DES surfaces for TD1-Cu at 295 K at various t2 delay times: (a) 0.4 ps, (b) 1.2 ps, (c) 13 ps, (d) 30 ps, (e) 100 ps, (f) 400 ps.

A second ground state bleach (GSB) feature associated with an electronic transition at 581 nm appears on the diagonal in Figure 2.3 (see also Supporting Information Figure 2.11), coinciding with the shoulder observed in the 295 K absorption spectrum. However, due to its proximity to the edge of the laser spectrum, the associated signal is weak. In Figure 2.3 (b)-(d), an excited-state absorption (ESA) feature is observed as an off-diagonal peak at $\lambda_1 = 606$ nm and $\lambda_3 = 625$ nm. Although this signal is extremely weak, we can assign it based on our previous work [71]. It exhibits a blue shift in its peak as the population time increases (Supporting Information Figure 2.12), which is consistent with our previous findings.

To determine the decay timescales associated with the diagonal 600 nm peak in Figure 2.3 (a)–(f), the associated region of the 2DES data was integrated (see also Supporting Information Figure 2.13) and plotted as a function of t_2 and fit to decaying exponentials. From these data, two timescales were recovered, 2.5 ± 0.4 ps and 13.8 ± 1.0 ps. These timescales are in agreement with our previously reported results for this system at room temperature [71], with the shorter timescale corresponding to vibrational relaxation and the longer timescale to the lifetime of the excited state. Due to low signal, a reliable timescale could not be extracted from the ESA feature at $\lambda_1 = 606$ nm and $\lambda_3 = 625$ nm, however, that signal is also gone at long t_2 times.
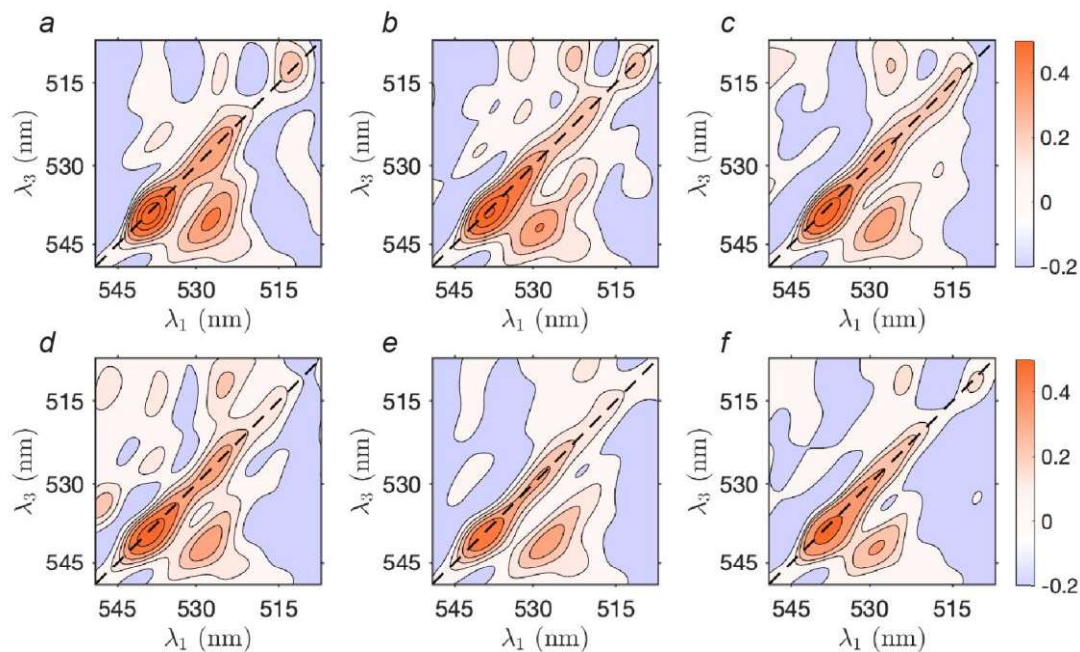
Figure 2.4: Representative absorptive 2DES surfaces for TD1-Cu at 77 K at various t2 delay times: (a) 0.4 ps, (b) 1.2 ps, (c) 13 ps, (d) 30 ps, (e) 100 ps, (f) 400 ps.

The 2DES experiments at 77 K used a laser pulse with a central wavelength of 529 nm (see Supporting Information Figure 2.7). This pulse is overlapped with the primary absorption feature in the 77 K spectrum. As the spectral bandwidth of this pulse did not span the entire transition, there is some shaping of the features in the 2DES spectrum due to a convolution of the absorption with the laser pulse. Figure 2.4 (a)–(f) displays representative 2DES surfaces at 77 K for various t_2 delays. The change in temperature from 295 K to 77 K and the associated dimerization of TD1-Cu significantly changes the observed signal. At 295 K, the 2DES measurements are dominated by the GSB on the diagonal at 600 nm (Figure 2.3 (a)–(d)) and all features disappear on the order of tens of picoseconds. At 77 K, we observe two closely spaced narrow diagonal peaks at 528 nm

and 539 nm (Figure 2.4 (a)–(f)). These correspond to GSBs from two excitonic energy levels. A crosspeak also appears at λ_1 = 528 nm and λ_3 = 539 nm, associated with energy transfer between the higher to the lower state. The crosspeak appears due to electronic coupling in the dimer. All features observed in the 2DES spectra at 77 K persist to the maximum experimental delay of 400 ps, while at 295 K, the signal has fully decayed within the first 100 ps, highlighting the presence of much longer-lived excited state in the TD1-Cu dimer compared to its room temperature monomer counterpart.

The two diagonal peaks at 539 nm and 528 nm in the 77 K 2DES spectra arise from the GSB of two closely positioned electronic transitions originating from the triplet ground state of the dimer. Based on EPR measurements [26], the ligand spin in the dimer is quenched due to strong antiferromagnetic coupling, while the spins on the Cu metal centers pair, resulting in a signal typical of a Cu(II) dimeric species with a spin triplet [26]. These GSB features are associated with the peak in the 77 K steady-state absorption spectrum (Figure 2.2) near 525 nm and a broad shoulder on the low energy side. The signal corresponding to these GSBs persists throughout the entire experimental delay of 400 ps. Notably, the off-diagonal crosspeak between these two states is present from the beginning of the experiment, providing evidence of strong excitonic coupling between these states. This crosspeak also persists beyond the maximum experimental delay.
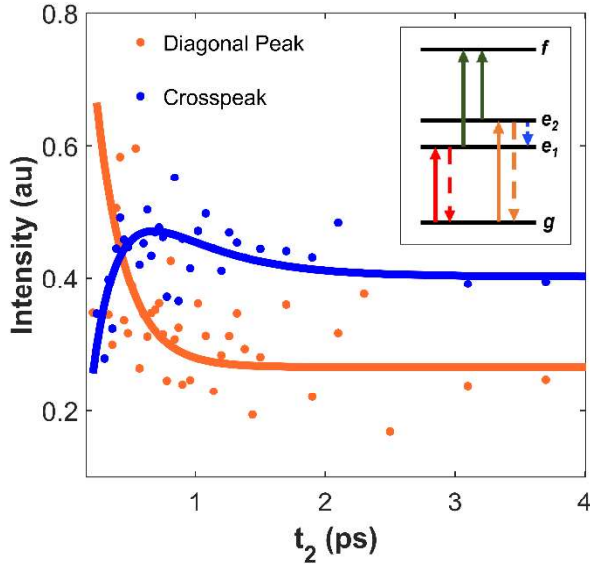
Figure 2.5: Short time dynamics for the 528 nm electronic transition and the crosspeak at $\lambda 1 =$ 528 nm and $\lambda 3 = 539$ nm. The dots correspond to data points from integrated regions of the 2DES spectra at delay times, t2. The solid lines are fit with exponential terms reported in the main text. The retrieved decay timescales for the 528 nm diagonal peak are 240 ± 70 fs and a nanosecond timescale (beyond the maximum experimental delay). The crosspeak shows an initial rise of 165 $\pm$ 70 fs followed by a biexponential decay with timescales of 460 ± 80 fs and a nanosecond timescale. The inset presents the level structure for the dimer.

The decay timescales for the two diagonal peaks as well as the crosspeak below the diagonal in the 77 K 2DES data were determined by integrating the corresponding regions (Figure 2.5, Figures 2.14 to 2.16) for all t_2 delay times and fitting those integrated traces with exponentials. The integrated trace of the GSB at 528 nm has a biexponential decay with timescales of 240 ± 70 fs and a nanosecond timescale that persists beyond the maximum delay time of the 2DES experiment (400 ps). As the maximum experimental delay is significantly shorter than the lifetime of the

signal, the associated nanosecond timescale cannot be reliably determined from the 2DES experiment. To determine this longer lifetime, a transient absorption measurement with a maximum delay of 1.4 ns was performed. The recovery of the ground state bleach was fit to exponential terms, recovering a long timescale of 1.0 ± 0.3 ns associated with the excited state lifetime. The transient absorption data and associated fit can be found in the SI (Figures 2.17 and 2.18).

The lower energy state at 539 nm displays a biexponential decay profile with a fast decay component of 480 ± 60 fs, followed by a nanosecond timescale. Unlike the diagonal features, the crosspeak signal rises during the early population times with a timescale of 165 ± 70 fs. The higher energy diagonal peak has a corresponding but oppositely signed sub-250 fs timescale. These timescales are associated with an energy transfer process between the two states resulting from excitonic coupling [80]. Following the rise in the signal from the fast energy transfer, the crosspeak then undergoes a biexponential decay with timescales of 460 ± 80 fs and a nanosecond timescale. The 460 fs and 480 fs timescales observed for the crosspeak and the diagonal peak at 539 nm, respectively, correspond to vibrational relaxation in the lower energy transition.

Both diagonal peaks as well as the crosspeak in the 77 K data persist beyond the maximum delay of the experiment. From the transient absorption measurement, the lifetime of the excited state at 77K was found to be 1.0 ± 0.3 ns. In contrast, at room temperature, the lifetime of the excited state is on the order of tens of picoseconds. The significantly longer excited-state lifetime at low temperature means that the process facilitating fast (picosecond) excited-state relaxation in the monomer at 295 K is not available at 77 K due to a change in the electronic structure associated with dimerization. Fast excited-state decay in the monomer at 295 K is likely mediated through

coupling to metal-centered states. Dimerization involves coupling between the spins localized on the copper metal centers and significantly modifies the electronic structure, as shown by the shift in the absorption spectra. This change in the electronic structure likely makes the 295 K deactivation pathway unfavorable and leading to longer-lived excited-state lifetimes.

The temperature-dependent change in the electronic structure arises from excitonic coupling in the dimer. At 77 K, the TD1-Cu dimer behaves like a model excitonic system. Upon dimerization, the resulting excitonic states, denoted as e_1 and e_2 in the inset in Figure 2.5, appear in the 77 K 2DES data at 539 nm and 528 nm, respectively. Up arrows signify transitions to higher energy electronic states, while down dashed arrows denote population relaxation to lower energy electronic states. The formation of an excitonic dimer at 77 K is supported by the observation of an energy transfer crosspeak. Based on the thermodynamic parameters (Supporting Information Section 2 and Figure 2.8) recovered from our absorption data, ΔG of dimerization is equal to zero at approximately 185 K. Considering the value of kT at that temperature, the coupling interaction driving dimerization is approximately 16 meV. In addition, the average energy of excitonic states is blue-shifted by approximately 250 meV with respect to the ground state in the dimeric form in comparison to the energy difference between the excited state and ground state of the monomer. This shift in energy is an order of magnitude greater than the coupling interaction, as expected for molecular dimers [80, 81].

2.4 Conclusion

In conclusion, the temperature-dependent reversible spin-mediated dimerization of TD1-Cu modifies the optical properties, leading to significant changes in the electronic structure and the

ultrafast dynamics. At room temperature, the triplet monomer form of TD1-Cu is a Cu(II)-bound radical whose excited state decays with a picosecond timescale. At 77 K, dimerization mediated by spin interactions between unpaired electrons on each of the monomers results in an excitonic system with a long excited-state lifetime. The unusual properties of TD1-Cu as a stable radical with two unpaired electrons results in spin-based temperature-switchable optical properties. These findings suggest that the TD1-Cu system may be useful as a spin- and temperature-controlled molecular switch with applications in areas ranging from spin dynamics to redox chemistry and catalysis.

2.5 Supporting Information

2.5.1 Steady-State UV-Visible Spectroscopy

The TD1-Cu complex was synthesized according to previously reported methods [25, 26, 82]. A solution of the TD1-Cu complex was prepared in a solvent mixture of methyl cyclohexane (86% V/V) and toluene (14 % V/V) to facilitate formation of an optically clear glass at cryogenic temperatures. These samples were used for steady-state absorbance spectroscopy, performed using an Agilent Cary 100 in a 1 mm pathlength quartz cuvette. A zoomed in region of the low energy region of the absorption spectrum showing low-lying states with very small oscillator strengths is shown in Figure 2.6. Representative laser spectra used for the 2DES measurements as well as temperature-dependent absorption measurements are shown in Figure 2.7.
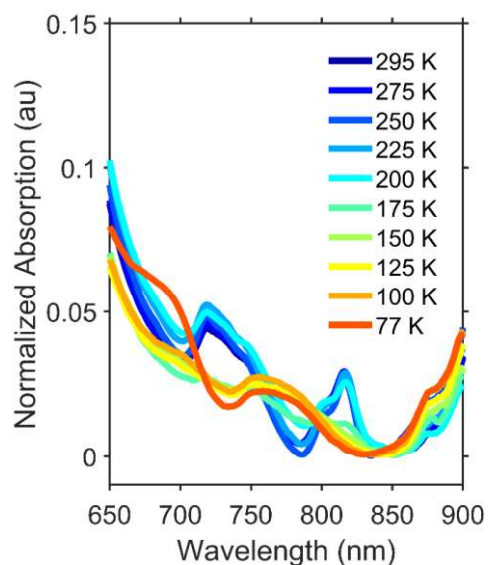
Figure 2.6: Zoomed in region of the steady-state absorption spectra between 650 nm and 900 nm (normalized to main π-π* transition for monomer at 295 K) of TD1-Cu complex dissolved in methyl cyclohexane-toluene solvent mixture at various temperatures. The 295 K spectrum shows low oscillator strength peaks near 720 nm and 816 nm while the 77 K spectrum has a small peak at 777 nm and another one beyond 900 nm.
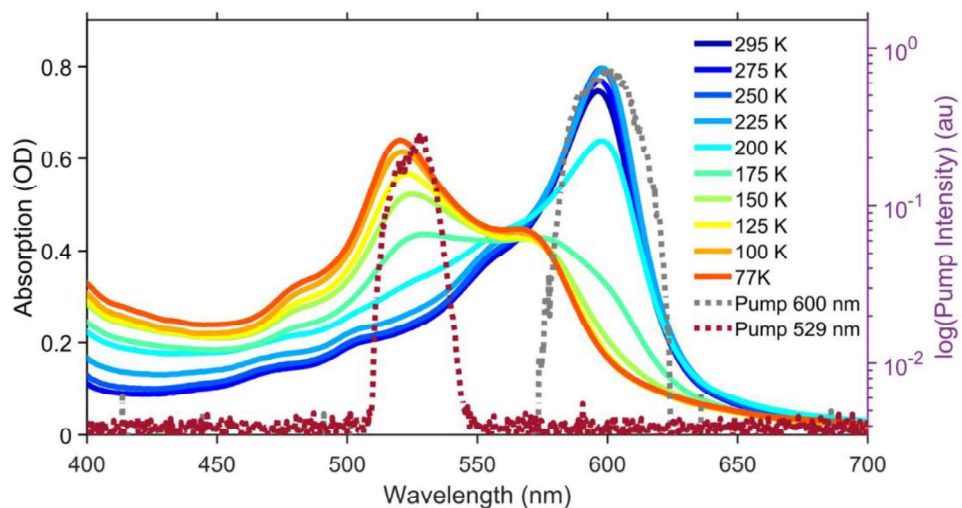
Figure 2.7: Plot representing the change in absorption line shape of the TD1-Cu complex in 6:1 vol/vol solvent mixture of methylcyclohexane:toluene as the temperature is lowered to 77 K. The optical density of the absorption is along the left y-axis while the right y-axis represents the intensity of the excitation pulse used for performing the room temperature (295 K) and 77 K experiment on a log scale. The pump spectra used to collect the 2DES data are shown as dotted lines in gray and dark magenta for 295 K and 77 K measurements, respectively.

2.5.2 Thermodynamic Parameters

The thermodynamic parameters for dimerization of the TD1-Cu complex as a function of temperature are calculated using the UV-Vis absorption spectra (see Figure 2.7). The rate of dimerization at any temperature T is calculated using the following relation:

$$K_{dimer}(T) = [D]_T/[M]_T{}^2$$

Where $[D]_T$ is the dimer concentration at temperature T while $[M]_T$ is the monomer concentration at temperature T. Using conservation of mass and assuming there is no appreciable dimer population at room temperature, we can substitute the monomer concentration using the following relation:

$$[M]_T = [M]_{295K} - 2[D]_T$$

Although the signal at room temperature is assumed to be dominated by the monomer, this does not mean that there is no dimer present, just that its contribution is minimal. Initial monomer concentration at room temperature (295 K) was determined using the optical density for the monomer $\pi\ to\ \pi^*$ transition at 600 nm. Dimer concentrations at various temperature was determined using the absorption peak at 521 nm which is associated with the dimer $\pi\ to\ \pi^*$

transition. The corresponding values of ΔG values are plotted in Figure 2.8 as a function of temperature.
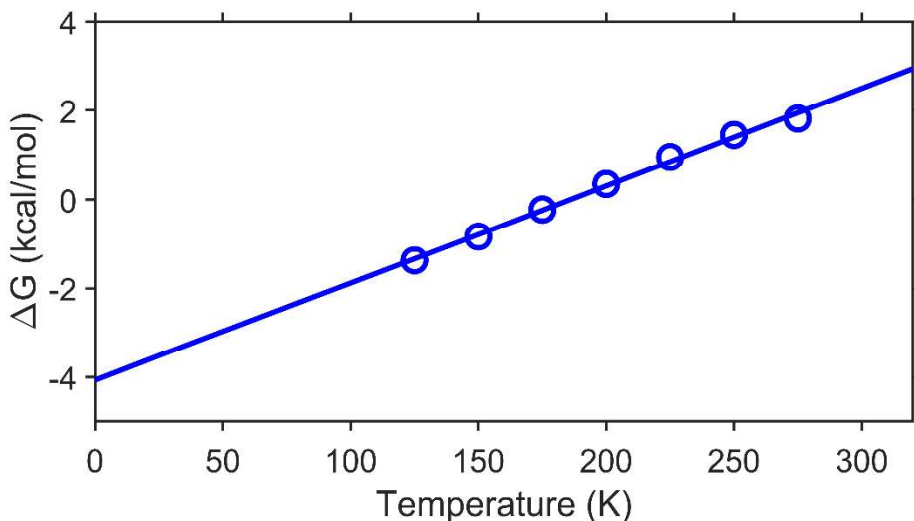
Figure 2.8: Gibbs free energy for dimerization of TD1-Cu complex obtained from the steady-state absorption spectra (Figure 2.7).

2.5.3 Two-Dimensional Electronic Spectroscopy (2DES)

Pump-probe geometry 2DES measurements were performed using a home-built apparatus. A regenerative-amplifier laser system from Coherent (Libra) was used to generate sub 100 fs pulses with around 4 mJ centered at 800 nm at a 1kHz repetition rate. About 250 μJ of this output was used to power a home-built single-pass noncollinear optical parametric amplifier (NOPA) generating pulses from 500 nm to 700 nm with a spectral FWHM between 20 nm and 50 nm. The NOPA output was sent through a prism compression line for chirp compensation. The pulse was then split to generate a pump (stronger intensity) and a probe (weaker intensity) beam. After going

through a variable neutral density filter consisting of a waveplate/polarizer pair, the pump pulse passed though FASTLITE Dazzler pulse shaper which provided two collinear identical pump pulses with a controllable variable time delay. The probe pulse was routed first through a waveplate/polarizer pair and then along a mechanical delay line. At the sample position, the probe was focused using f = 100 mm lens while pump was focused using f = 150 mm, resulting in a spot size of 80 µm at the focus. The pulses were iteratively compressed by maximizing the peak intensity and minimizing the temporal width of the cross-correlation signal from a 1 mm BBO collected on a Si-based detector from Thorlabs (Det10A2) connected to a lock-in amplifier while chopping the pump. For the 2DES experiments, the probe was focused into a spectrometer (SpectraPro HRS-300) after the sample position. The light was detected using a CCD (PIXIS 400, Princeton Instrument). The pulse was centered at 600 nm and 529 nm, as shown in Figure 2.7, when performing the experiments at 295 K and 77K respectively, in resonance with the lowest energy main transition in the visible region at the respective temperatures. As shown in Figure 2.7, the NOPA pulses did not span the entire absorption spectrum of the Cu-TD1 sample. This is a limit of the experimental apparatus. A BBO was used to generate an SHG signal to evaluate the pulse temporal resolution, giving a compressed temporal width of sub-45 fs and sub-40 fs pulse for room temperature and 77 K measurements respectively. Additional pulse characterization was performed by polarization gated frequency resolved optical gating (PG-FROG) using a non-resonant sample (carbon disulfide, CS_2. The PG-FROG measurement with the 600 nm pulse resulted in a temporal width of sub-45 fs. Representative PG-FROG data is shown in Figure 2.9. The 529 nm pulse used for the 77 K measurements was sub-40 fs. Representative PG-FROG data

is presented in Figure 2.10. All 2DES measurements at 77 K were performed using a nitrogen

vapor cryostat (OptistatDN, Oxford Instruments).
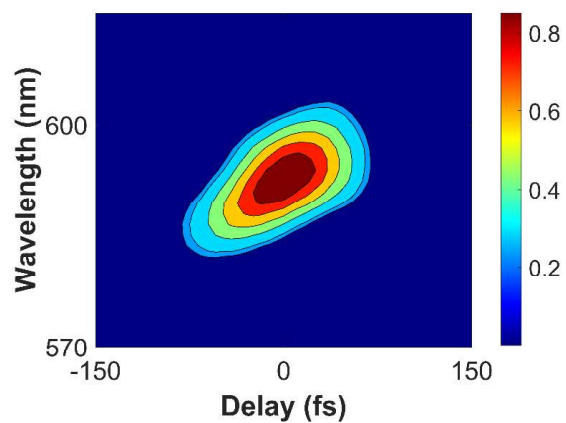
Figure 2.9: FROG output for 600 nm laser pulse used for the 2DES experiment at room

temperature (295 K).
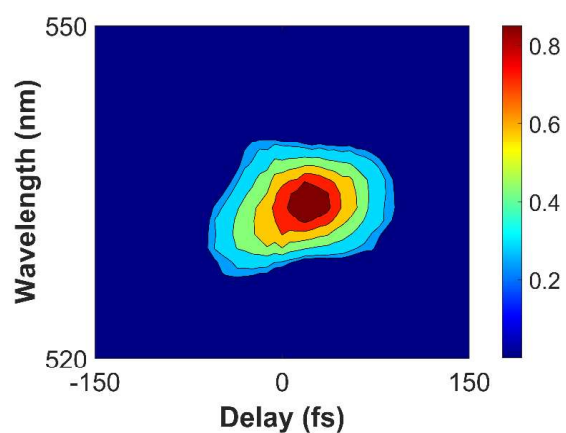
Figure 2.10: FROG output for 529 nm laser pulse used for the 2DES experiment at 77 K.
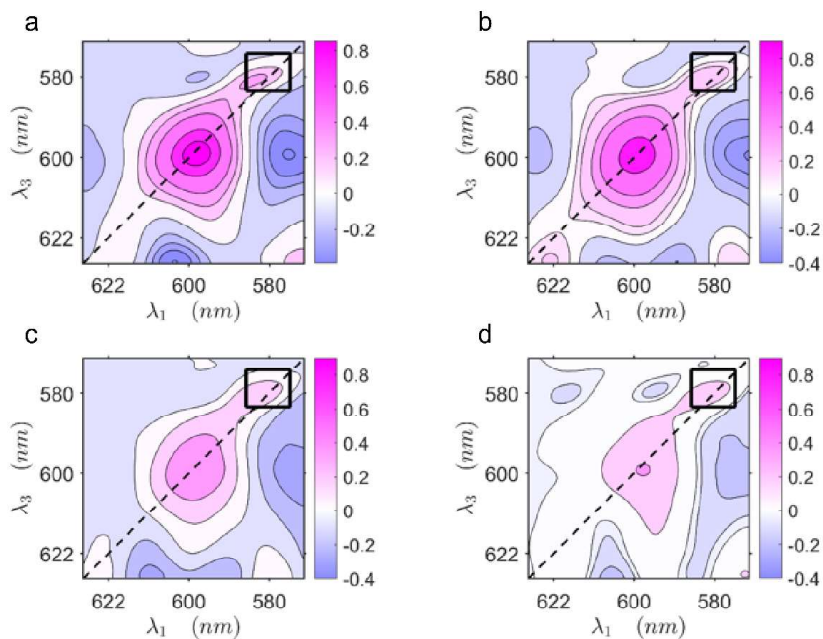
Figure 2.11: Real-value 2DES surface plots from the room temperature (295 K) measurement of the TD1-Cu complex taken at various t_2 delay points (0.5, 1.4, 13, and 30 ps in the following order for (a) to (d)). The boxed region in the top right corner highlights the transition centered at 581 nm.
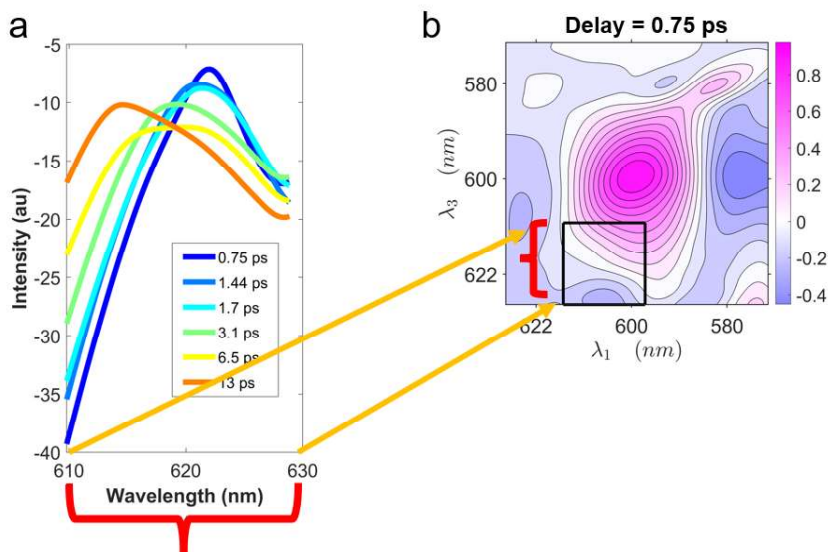
Figure 2.12: Blue-shift in slices obtained by integrated along λ_1 axis between 597 nm – 615 nm in the boxed region in (b). The TA traces plotted in panel (a) generated after integrating over the excitation frequencies corresponding the horizontal length of the black box in panel (b). X-axis of panel (a) is same as the vertical length of the black box region shown in panel (b).

The timescales reported in the paper were obtained by integrating regions of the 2DES data associated with different signal components and fitting that data to exponentials. These fits are shown in Figures 2.13 to 2.16. Short time dynamics and associated fits for the data in Figures 2.15 and 2.16 are also presented in Figure 2.5. Figure 2.13 shows a biexponential fit to the recovery of the ground state bleach at approximately 600 nm for Cu-TD1 at room temperature. This fit obtained timescales of 2.5 ± 0.4 ps and 13.8 ± 1.0 ps. Figure 2.14 presents the data and associated biexponential fit for the dynamics of the diagonal peak for Cu-TD1 at 77K at approximately 540 nm. The fit parameters were 480 ± 60 fs and 1.7 ns $\pm$ 500 ps. The time-resolved dynamics of the diagonal peak at approximately 530 nm for Cu-TD1 at 77K and associated biexponential fit are

61

shown in Figure 2.15. The timescales for this fit were 240 ± 70 fs and 1.8 ns ± 300 ps. Figure 2.16 presents the time-resolved dynamics of the below the diagonal crosspeak at approximately $\lambda_1 = 530$ nm and $\lambda_3 = 540$ nm. This data was fitted using one rising and two decaying exponentials respectively with timescales of 165 ± 70 fs, 460 ± 80 fs and 1.5 ns ± 300 ps. The nanosecond timescales associated with the fits to the 77 K data significantly exceed the maximum delay of the 2DES measurements and, as a result, are only estimates. For all fits, the error tolerances were estimated by calculating the standard deviation of the timescales obtained from repeat measurements.
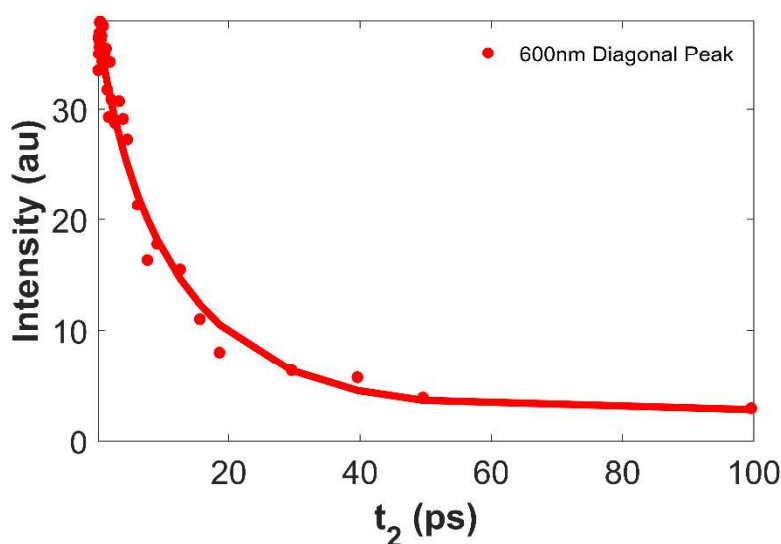
Figure 2.13: Integrated intensities for the room temperature 2DES data for the region between 593 nm to 606 nm along both λ_1 and λ_3 axes are represented here by a red dot for each population time. This is the region corresponding to the GSB signal from the lowest ligand π- π^* transition. The solid red trace is a biexponential fit to the data with 2.5 ± 0.4 ps and 13.8 ± 1.0 ps timescales.
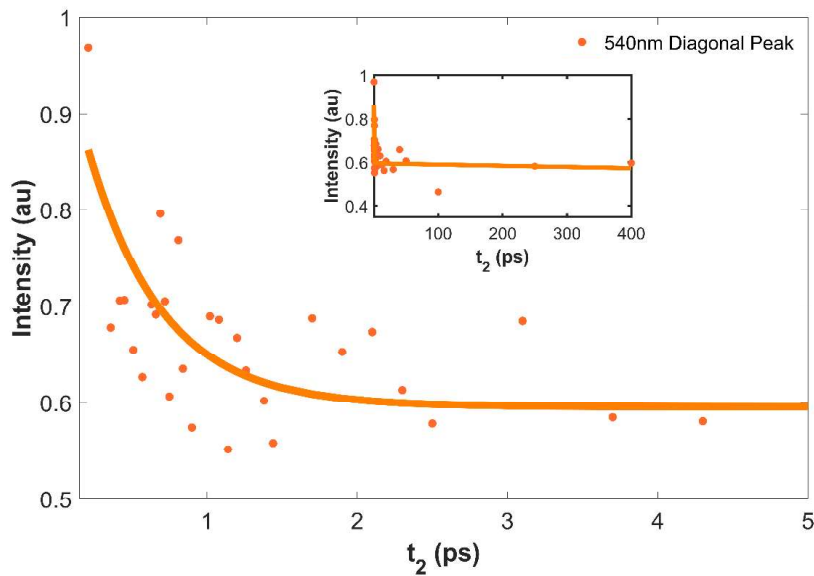
Figure 2.14: Integrated intensities for the 77K 2DES data for the region between 536 nm to 544 nm along both λ_1 and λ_3 axes (lower diagonal peak) are represented here by an orange dot for each population time. The solid orange line is a biexponential fit to the data with 480 ± 60 fs and a nanosecond timescales.
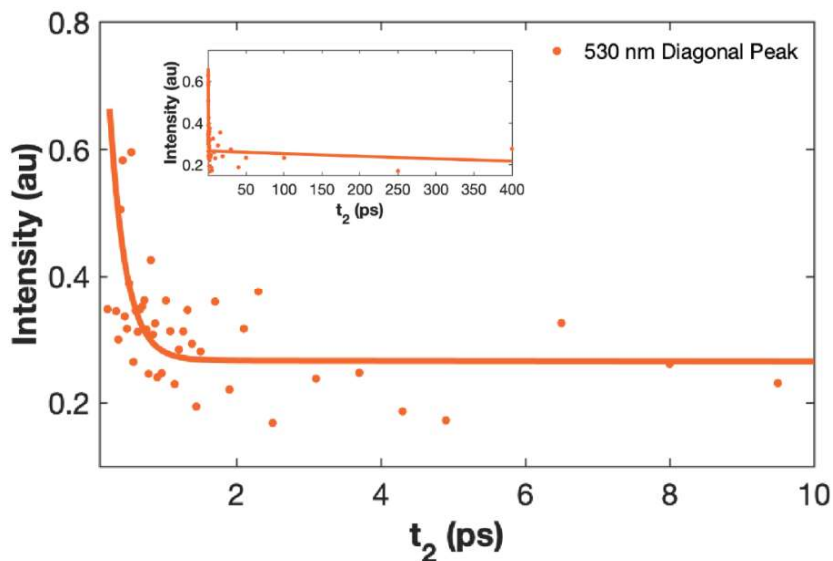
Figure 2.15: Integrated intensities for the 77K 2DES data for the region between 524 nm to 532 nm along both λ_1 and λ_3 axes (upper diagonal peak) are represented here by an orange dot for each population time. The solid orange line is a biexponential fit to the data with retrieved timescales being 240 ± 70 fs and a nanosecond decay.
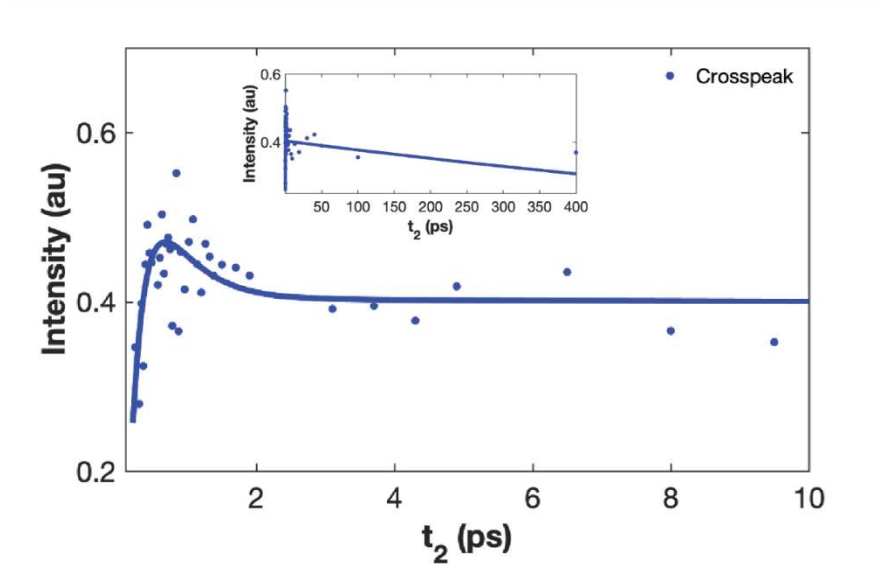
Figure 2.16: Integrated intensities for the 77K 2DES data for the region between 525 nm to 531 nm along the λ_1 axis and between 537 nm to 543 nm along the λ_3 axis (below diagonal crosspeak) are represented here by a blue dot for each population time. The solid blue line is a three-exponential fit to the data with one rising (165 ± 70 fs) and two decaying (460 ± 80 fs and a nanosecond timescale).

64

2.5.4 Transient Absorption

Transient absorption measurements were performed using a home-built experimental apparatus. A 1kHz Ti:Sapphire laser system was used to generate pulses centered at 540 nm from a commercial OPA (TOPAS) and to generate white light by plasma formation in an argon filled tube. The pluses from the OPA served as the pump and the white light was used as the probe. The probe pulse was generated by Kerr-optic self focusing via 800 nm (using approximately 1.9 mJ input pulses) light from our previously described Libra into an approximately 1.6 m tube after a 2 m focus to generate white light with sub 2% stability spanning 400 nm to 720 nm. The pump and probe were delayed relative to each other using a mechanical stage with a maximum delay of 1.4 ns. The transient absorption signal was frequency dispersed using a spectrometer (SpectraPro HRS-300) and collected using a CCD (PIXIS 400, Princeton Instruments).
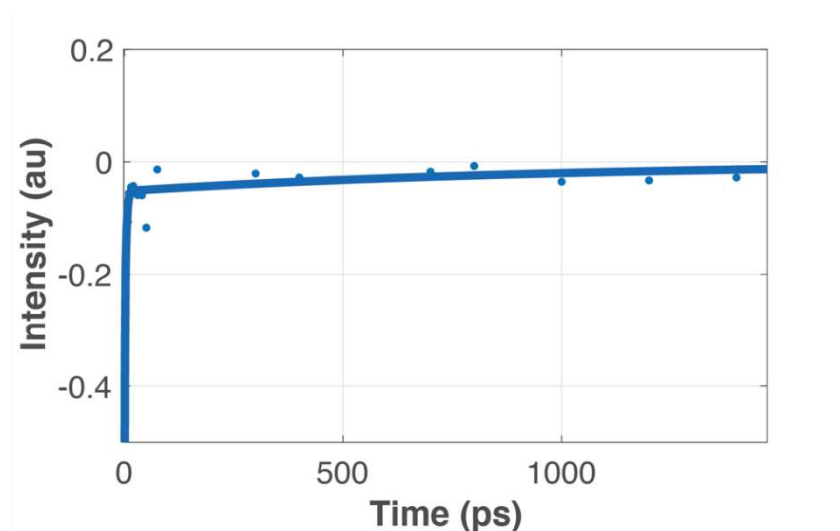
Figure 2.17: Integrated region of the ground state bleach obtained from the transient absorption measurement on Cu-TD1 at 77 K. The 1.0 ± 0.3 ns timescale obtained from this data corresponds to the lifetime of the excited state.
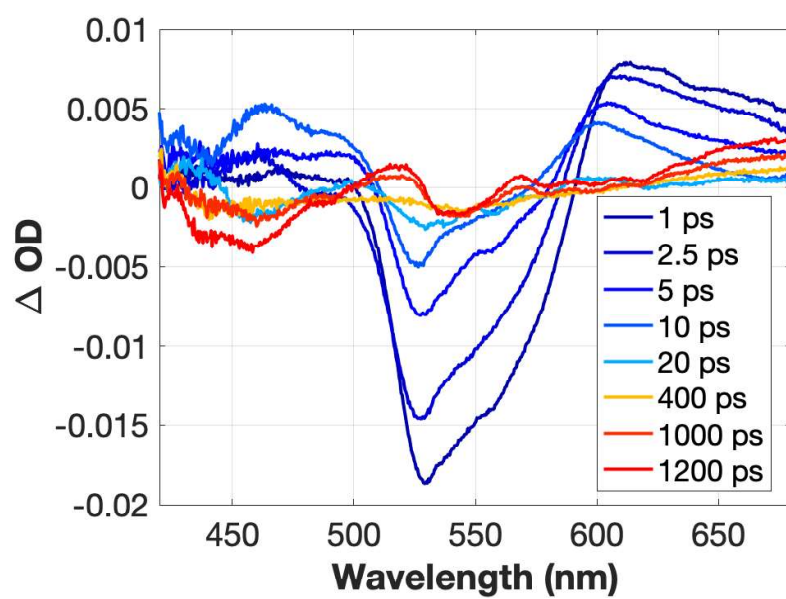
Figure 2.18: Broadband probe detected transient absorption measurement of Cu-TD1 at 77K. The signal has been background scatter corrected.

Chapter 3:

Ultrafast Dynamics of a Red-Light Activated Organic Photocatalyst in the Oxidative Hydroxylation of Phenylboronic Acid

3.1 Chapter Summary

Chapter 3 delves into the role of the ^{n}Pr-DMQA$^+$ cation in photoredox catalysis, focusing on its mechanism in the oxidative hydroxylation of phenylboronic acid. Through transient absorption and time-correlated single photon counting, the chapter highlights the role of catalyst's long-lived triplet state and its interactions with sacrificial amines. These findings elucidate the intricate photophysical dynamics that drive catalytic activity, enriching the thesis by linking structural characteristics to functional outcomes in photocatalytic processes.

3.2 Introduction

Photoredox catalysis has been the subject of significant interest [83-93] due to its potential environmental and economic advantages [94-97]. Over the past decade, the growth of photoredox catalysis has significantly influenced chemical methodologies, enabling the development of new synthetic pathways through light activation [89-91, 98-100], simplifying complex reactions under milder conditions [85, 98, 101-104], minimizing the reliance on harmful reagents [85, 105, 106], and enhancing waste reduction and process efficiency. While photoredox catalysis using transition metal complexes allows access to a wide array of reactions [22, 89, 107-113], issues such as cost and potential toxicity persist. Organic photocatalysts have emerged as a potential solution due to their structural flexibility and low cost. Red-light-activated photoredox catalytic processes have recently been an area of great interest [114-119]. The benefits of red-light photocatalysis include its lower energy requirement, reduced side reactions, minimized health risks, and its greater penetration through scattering media [42, 43, 120-122].

This work investigates the ultrafast dynamics of the organic N,N'-di-n-propyl-1,13-dimethoxyquinacridinium (^{n}Pr-DMQA^{+}) red-light photocatalyst to understand its mechanism in the aerobic oxidative hydroxylation of phenylboronic acid. ^{n}Pr-DMQA^{+}, shown in Figure 3.1 inset, is a member of the helicene family characterized by a condensed aromatic structure, with fused rings arranged in a nonplanar fashion to alleviate steric hindrances [123]. This arrangement, combining a conjugated π-electron system with nonplanarity, is known to favor enhanced intersystem crossing rates [123-126]. Here we use transient absorption (TA) and time correlated single photon counting (TCSPC) to track the dynamics of the catalyst. These measurements suggest that the mechanism proceeds through a long-lived triplet state of ^{n}Pr-DMQA^{+}.

3.3 Experimental Section

^{n}Pr-DMQA$^+$ was synthesized according to a previously reported method [43]. For all optical measurements, solutions were prepared by dissolving 2.5 mg of ^{n}Pr-DMQA$^+$ in 5 mL of *N,N*-dimethylformamide (DMF). 0.5 mmol of phenylboronic acid and 1 mmol of DIPEA were added to ^{n}Pr-DMQA$^+$ in DMF, to generate a previously reported oxidative hydroxylation reaction mixture [42]. Steady-state UV/Vis absorbance measurements were collected using an Agilent Cary 100. Fluorescence spectra were gathered using an Agilent Cary Eclipse. All measurements were performed at room temperature.

TCSPC data were collected using a previously described home-built system [50]. Briefly, the output of a Coherent Vitara Ti:Sapphire oscillator generating pulses of 100 fs at 800 nm was frequency-doubled to 400 nm through a type-I β-barium borate (BBO) crystal and focused into the sample to generate fluorescence. The fluorescence was then directed to a monochromator and photomultiplier tube detector and lifetime decays were measured using a SPC-130 TCSPC (Becker-Hickl).

Broadband-detected TA experiments were performed using a home-built apparatus. Our regenerative amplifier laser system (Libra, Coherent) delivered 100 fs pulses at 800 nm with an energy output of approximately 4 mJ per pulse at a frequency of 1kHz. For our experiments, we allocated 1.5 mJ from this output to create a broad spectrum of visible light. This was achieved by focusing the beam into an argon-filled tube generating white light that spanned 450 nm to 700 nm for broadband detection. The broadband pulses were temporally compressed using chirped mirrors (Laser Quantum). Following compression, the broadband light was split into pump and probe beams. The intensity of the pump beam was controlled using a variable neutral density filter,

consisting of a waveplate and polarizer duo, before being shaped by a Dazzler (FASTLITE) pulse shaper. Post-shaping, the pump beam exhibited a uniform intensity profile with a spectral range of 570 nm and 630 nm. The probe beam also passed through a variable neutral density filter and was delayed relative to the pump pulse using a mechanical delay line (DL325, Newport). The pump and probe were focused to the sample position using 150 mm and 100 mm focal length lenses, respectively, resulting in a focal spot size of 100 μm. The signal was collected using a SpectraPro HRS-300 spectrometer and a PIXIS 400 CCD camera (Princeton Instruments). To determine the temporal resolution of the pulses, a BBO crystal was utilized to generate a second harmonic signal for cross-correlation. This signal was measured using a silicon-based detector (Det10A2) from Thorlabs connected to a lock-in amplifier. The temporal width of the pulses was ~40 fs as shown in Figure 3.10 (see supporting information). The power at the sample position was approximately 50 nJ.

3.4 Result and Discussion

Figure 3.1 inset shows molecular structure of the helical carbenium ion, N,N′-di-n-propyl-1,13-dimethoxyquinacridinium (^{n}Pr-DMQA$^+$). The steady state absorption spectrum of ^{n}Pr-DMQA$^+$ in N, N-dimethylformamide (DMF) is presented in Figure 1. The main feature at 620 nm corresponds to the S_0 to S_1 with a shoulder around 585 nm [42, 127] associated with a vibrational mode. The fluorescence, shown in Figure 3.1, is maximized at 685 nm, corresponding to a Stoke shift of 0.2 eV.
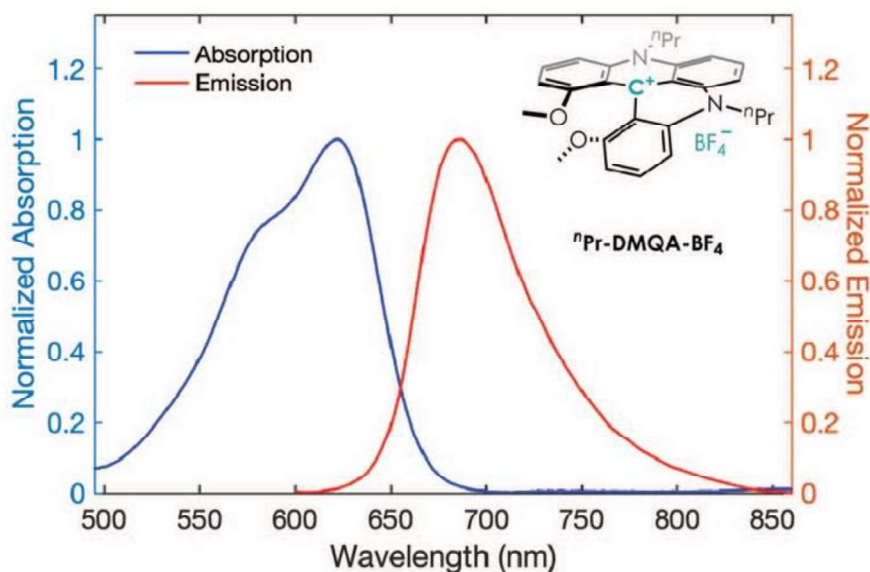
Figure 3.1: Normalized absorption (blue trace) and fluorescence (red trace) spectra of ^{n}Pr-DMQA^{+} dissolved in N, N-Dimethylformamide (DMF). Inset top right: structure of ^{n}Pr-DMQA^{+}. Carbon-bonded hydrogen atoms are omitted for clarity.

^{n}Pr-DMQA^{+} is used here to catalyze the oxidative hydroxylation reaction of phenylboronic acid (PhB(OH)$_2$) in the presence of N,N-Diisopropylethylamine (DIPEA). DIPEA acts as a sacrificial amine while PhB(OH)$_2$ is the reagent. The absorption spectrum of ^{n}Pr-DMQA^{+} does not exhibit a spectral shift when in solution with either DIPEA, and/or PhB(OH)$_2$. However, the fluorescence is quenched by about 60% in the presence of DIPEA with no shift in the peak position of the emission (see Figure 3.11 in the supporting information). The presence of PhB(OH)$_2$ does not affect the ^{n}Pr-DMQA^{+} fluorescence.

Figure 3.2 shows the TCSPC traces of ^{n}Pr-DMQA^{+} fluorescence in DMF with and without DIPEA. The recorded fluorescence lifetime of ^{n}Pr-DMQA^{+} is 5.8 ± 0.8 ns, which is unchanged by the presence of PhB(OH)$_2$. In the presence of DIPEA, this lifetime is quenched to 2.0 ± 0.3 ns.
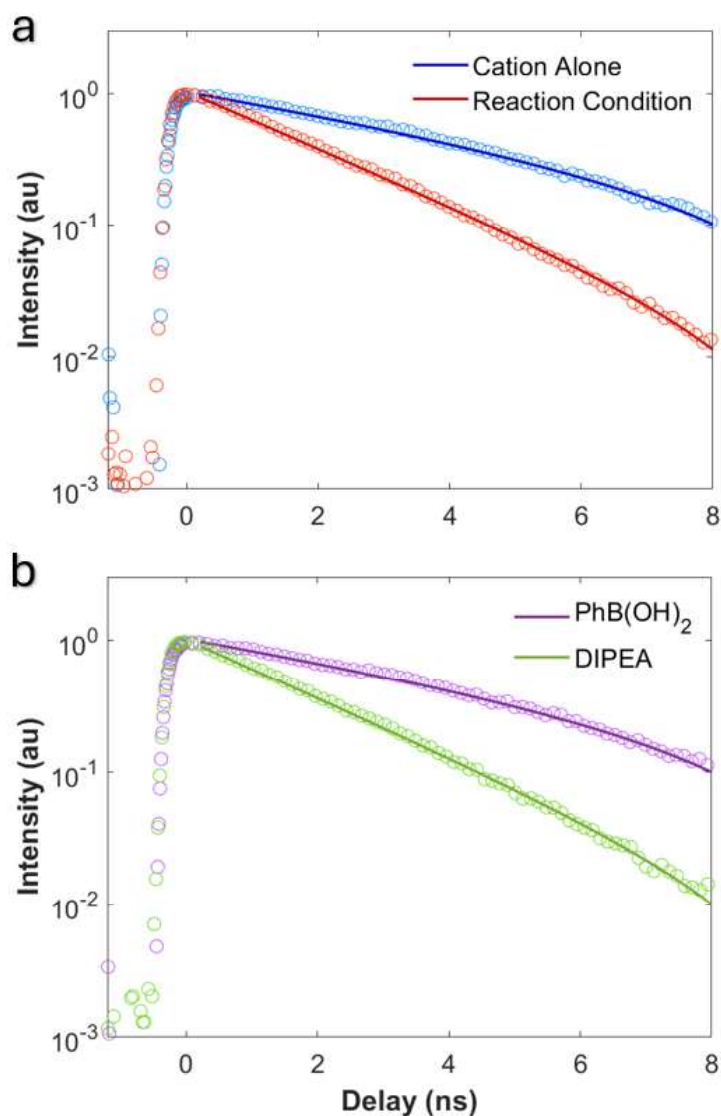
Figure 3.2: (a) Comparison between TCPSC data for ^{n}Pr-DMQA^{+} alone in DMF alone (blue) and in the presence of both DIPEA and PhB(OH)$_2$ in DMF (red). The solid traces show a single exponential fit to the corresponding data. (b) Comparison between the TCPSC data for ^{n}Pr-DMQA^{+} in the presence of PhB(OH)$_2$ (purple) and DIPEA (green). The solid traces of the respective colors show fits to the corresponding data. Both plots are on a semi-log scale. The

fluorescence lifetime of cation alone (or with $PhB(OH)_2$) is 5.8 ± 0.8 ns which is quenched to 2.0 ± 0.3 ns in the presence of DIPEA.

TA data for $^nPr\text{-}DMQA^+$ in DMF is presented in Figure 3.3 (a). A large ground state bleach (GSB) signal is observed around 625 nm immediately after pump excitation. This GSB signal exhibits red shift of $\sim$16 meV by 150 ps. Complete recovery of this bleach was not achieved within the 1.4 ns maximum observation time of the measurements. Another bleach minimum feature centered at 585 nm exhibited a similar response. A third bleach feature associated with fluorescence was also observed at 680 nm. Complete recovery of this feature did not occur within the maximum delay time of the experiment, consistent with the TCSPC lifetime of 5.8 ± 0.8 ns.

The excited state absorption (ESA) feature that appears at wavelengths lower than 500 nm provides further insight into the $^nPr\text{-}DMQA^+$ dynamics. An ESA centered at 485 nm shifted to 495 nm over the first 200 ps and then maintained most of its amplitude by the end of 1.4 ns experimental timespan. A gradually evolving ESA signal was observed around 530 nm, although this was initially obscured by the broad negative bleach. The signal changes sign around 100 ps, and reached its maximum positive amplitude around 300 ps. The slow rise and persistence of this signal beyond 1.4 ns suggests it originates from the S_1 state, potentially corresponding to transitions from S_1 to higher lying triplet states [128].
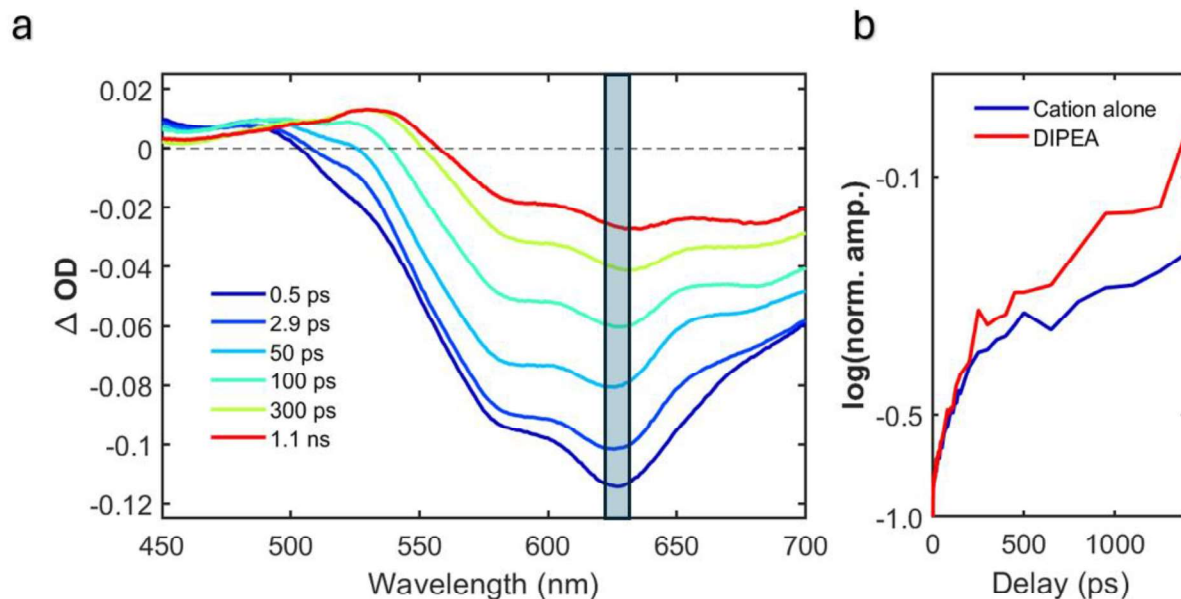
Figure 3.3: (a) TA traces of ^{n}Pr-DMQA$^+$ in DMF at different delay times. (b) Comparison between the normalized traces produced after integrating the highlighted region in panel (a) highlighting the slower recovery of bleach for ^{n}Pr-DMQA$^+$ alone in DMF (blue trace) in comparison to when DIPEA is present (red trace) in the solution with y-axis on log scale.

TA data for ^{n}Pr-DMQA$^+$ in the presence of PhB(OH)$_2$ is shown in Figure 3.12 (see supporting information). As shown in Figure 3.12, the ultrafast dynamics of ^{n}Pr-DMQA$^+$ are unchanged in the presence of PhB(OH)$_2$. TA data of ^{n}Pr-DMQA$^+$ in DMF following excitation at 620 nm in the presence of DIPEA alone is shown in Figure 3.13 (see supporting information). Following pump excitation, a GSB feature centered around 625 nm is observed. This GSB undergoes a red shift of ~16 meV over 150 ps, consistent with that observed for the photocatalyst alone. The immediate photoinduced response is confirmed by the bleach minimum established within the instrument

response time, accompanied by rapid recovery within 0.5 ps. Although the bleach did not fully recover over the experimental timescale, its recovery was faster compared to ^{n}Pr-DMQA^{+} with or without $PhB(OH)_2$ (see Figure 3.3 (b)), consistent with quenching in the presence of the amine. The bleach around 585 nm displays similar behavior to that of the GSB, with the overall recovery being relatively faster compared to ^{n}Pr-DMQA^{+} alone. Additionally, the bleach feature at 685 nm did not fully recover over the experimental timescale, although it was comparatively faster than that observed for ^{n}Pr-DMQA^{+} alone. This observation of overall faster bleach recovery is consistent with the TCSPC measurement for ^{n}Pr-DMQA^{+} in the presence of DIPEA shown in Figure 3.2 (b) with a lifetime of 2.0 ± 0.3 ns. The ESA at ~485 nm is present immediately following pump excitation, while the other ESA feature emerges at ~530 nm after 100 ps, initially as part of the broad bleach feature and is possibly associated with transition from excited state to higher lying triplet state. Both ESA features persist throughout the maximum delay of the measurement, indicating a long-lived nature similar to that observed for ^{n}Pr-DMQA^{+} alone.
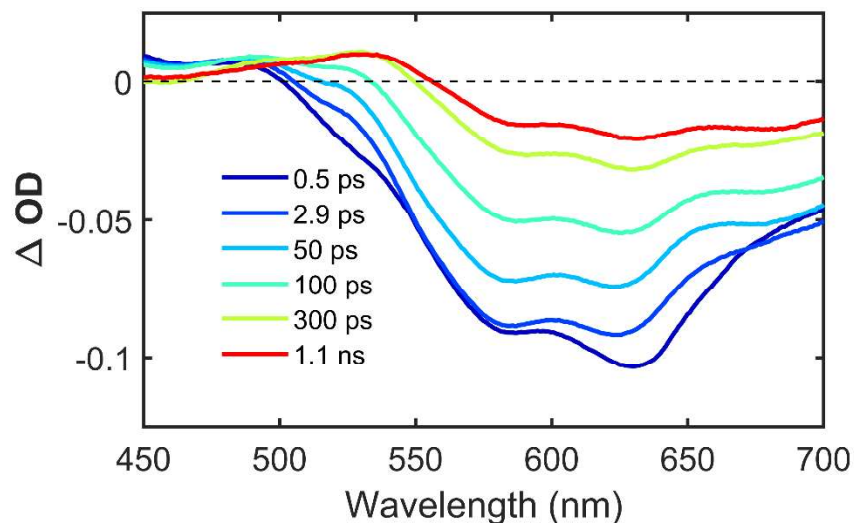
Figure 3.4: TA spectral traces of ^{n}Pr-DMQA^{+} in the presence of DIPEA and PHB(OH)$_2$ in DMF at different delay times.

TA data of ^{n}Pr-DMQA^{+} in DMF in the presence of DIPEA and PhB(OH)$_2$ is presented in Figure 3.4. The combination of DIPEA and PhB(OH)$_2$ at 100:50 ratios to that of ^{n}Pr-DMQA^{+} in DMF corresponds to the previously demonstrated conditions for a photocatalytic oxidative hydroxylation reaction [42]. The TA data shown in Figure 3.4 is similar to that of ^{n}Pr-DMQA^{+} alone although with faster bleach recovery, as observed in the case when only DIPEA is present (see Figure 3.13 in supporting information). The negative signal from 500 nm to 700 nm appears immediately following pump excitation. Within the negative feature there are three minima at $\sim$685 nm, $\sim$625 nm, and $\sim$585 nm. GSB is observed around 625 nm post pump excitation, with a red shift of $\sim$16 meV over 150 ps, consistent with that observed for the photocatalyst alone. The prompt photoinduced response is confirmed by the bleach minimum established within the

instrument response time, accompanied by rapid recovery within 0.5 ps. Although the bleach does not fully recover over the experimental timescale, its recovery is faster compared to ^{n}Pr-DMQA^{+} with or without PhB(OH)$_2$, which is consistent with quenching in the presence of the amine (see Figure 3.3 (b)). The bleach at ~585 nm exhibits similar behavior to that of the GSB, with overall recovery being relatively faster compared to ^{n}Pr-DMQA^{+} alone. Additionally, the third bleach feature associated with stimulated emission (SE) at ~685 nm does not fully recover over the experimental timescale, although the recovery is comparatively faster than that observed for ^{n}Pr-DMQA^{+} alone. This observation of overall faster bleach recovery is consistent with the TCSPC measurement shown in Figure 3.2 (a), with a lifetime of 2.0 ± 0.3 ns, corresponding with quenching in the presence of the amine. Similar to previous observations, the ESA at ~485 nm is present following pump excitation, while the other ESA feature emerges around 530 nm after 100 ps, initially as part of the broad bleach feature. Both ESA features persist throughout the maximum delay of the measurement.

For all TA measurements presented here, we observe a broad negative signal extending from 500 nm to 700 nm, associated with GSB and SE. Moreover, characteristic bleach features associated with SE and GSB are consistently observed around 685 nm, 625 nm, and 585 nm, respectively. Additionally, we observe ESA signals around 485 nm and 530 nm, which persist throughout the experimental timescale. However, notable differences arise in the overall recovery dynamics of the bleach features at longer delay times. In the presence of DIPEA and for the reaction conditions with both DIPEA and PhB(OH)$_2$, the recovery of the negative signal between 580 nm and 700 nm is faster compared to ^{n}Pr-DMQA^{+} alone, supporting the effect of amine

quenching on the excited state lifetime. In addition, the presence of $PhB(OH)_2$ does not alter the dynamics of the $^{n}Pr\text{-}DMQA^{+}$ cation (see Figure 3.12 in supporting information).

The TA measurements presented here show dynamics occurring across a broad range of timescales. We have constructed a kinetic model building upon prior investigations into helicenes, which have highlighted pathways involving intersystem crossing to triplet states [124, 126, 129-132], which can be particularly pronounced in nonplanar aromatic molecules [123, 125, 133]. Target analysis of the TA data was conducted based on the model depicted in Figure 3.5 (c) using Python-based package, KIMOPACK [134]. In all cases, the best fit to the data was achieved by considering a total of five decay rates, with the rate for intersystem crossing from the triplet state to the singlet ground state held as an offset due to its microsecond timescale [123, 124, 131, 135] which is significantly longer than the maximum delay time of the TA experiments.
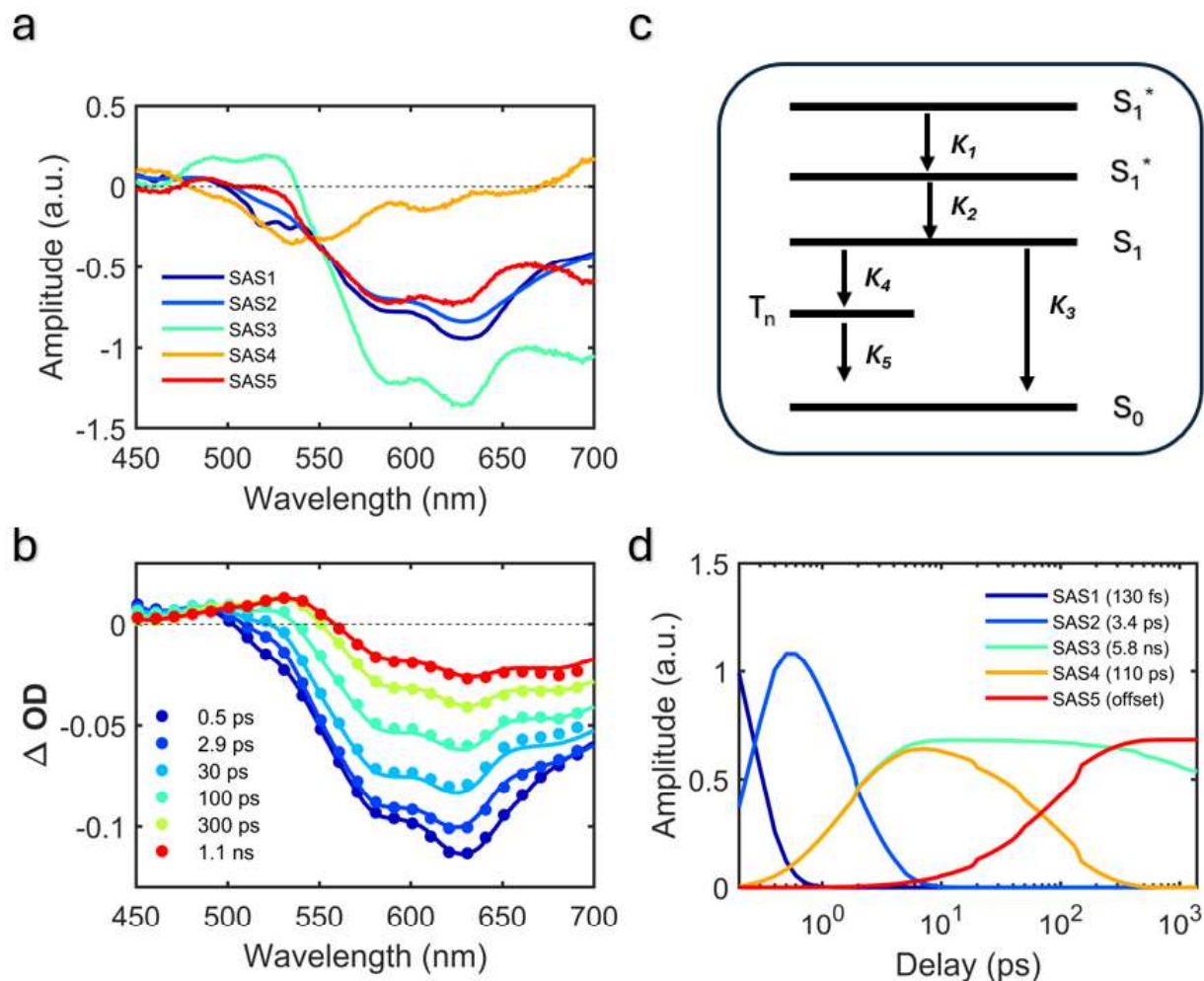
Figure 3.5: (a) Species-associated spectra (SAS) from the targeted analysis using the model shown in panel (c), and (b) raw TA data (dots) and fit (solid traces) for ^{n}Pr-DMQA$^+$ in DMF. (c) Kinetic model used in the targeted analysis with (d) corresponding kinetics for the model with the delay axis on log-scale.

Spectral analysis of the TA data reveals distinct features across the five species-associated spectra (SAS). Figure 3.5 presents the results for ^{n}Pr-DMQA$^+$ alone in DMF. The first three SAS

exhibit a bleach minimum centered around the ground state bleach (GSB) minimum at 625 nm, accompanied by a shoulder at 585 nm, corresponding to a vibronic sub-band observed in the absorption spectrum. The first two SAS display similar spectral characteristics. SAS1 undergoes decay within 135 ± 60 fs (all error estimates based on a 95% confidence interval), attributed to solvent-induced vibrational cooling. It is accompanied by positive amplitude below 500 nm, corresponding to ESA to higher-lying S_n states. In contrast, SAS2 decays over a longer timescale of 3.4 ± 0.5 ps, attributed to intramolecular vibrational redistribution (IVR). SAS3, corresponding to a time constant of 5.8 ns, consistent with our TCSPC results, has another local minimum beyond 660 nm related to SE and represents the S_1 to S_0 decay along with residual GSB. We assign SAS4 to ISC from the excited singlet state to the triplet manifold, with an associated timescale of 110 ± 18 ps [136-140]. Spectrally centered around 530 nm, this component has a local minimum around 620 nm, associated with GSB. Previous reports on azahelicenes compounds have indicated a typical S_1-T_1 energy gap to be more than 0.5 eV [123, 130]. This is consistent with the absence of phosphorescence observed up to 900 nm at cryogenic temperatures for ^{n}Pr-DMQA^{+} (see Figure 3.14 in supporting information).

Given the timescale associated with ISC in this system, the population of the S_1 state may initially transition to a higher-lying T_n state, followed by rapid internal conversion to T_1 and subsequent return to the S_0 ground state. This sequence has been reported previously for aza[7]helicene and other conjugated systems [126, 133]. Ultrafast ISC has been previously observed in organic molecules [136, 138, 139, 141-144], despite the absence of heavy atoms. This phenomenon has been attributed to the very small energy difference between the excited S_1 and T_n states [136, 138-140]. Reports also highlight enhanced spin-orbit coupling in nonplanar aromatic

compounds, which facilitates transitions between states with different spin [123, 125, 140, 143]. The amplitude of SAS5 is similar to that of SAS1 and SAS2 (see Figure 3.5(a)). We proposed that it is associated with ISC from T_1 to S_0. This non-decaying offset is consistent with the long lifetimes associated with such transitions [123, 124, 131, 135].

The results of the target analysis on the TA data for ^{n}Pr-DMQA$^+$ and PhB(OH)$_2$ in DMF are the same as those of the cation alone, indicating that the acid does not influence the photocatalyst dynamics (see Table 3.1 in supporting information). Figure 3.6 summarizes these results and compares them with the raw TA data. All the SAS are associated with the same components as in the case of the photocatalyst alone in DMF and have similar timescales. As before, SAS1 and SAS2 follow each other, while SAS3 shows bleach near 680 nm consistent with emission from the photocatalyst. SAS4 remains unchanged from the previous case when only the photocatalyst is present in DMF, while SAS5 represents an offset associated with the transition from T_1 to S_0 state.
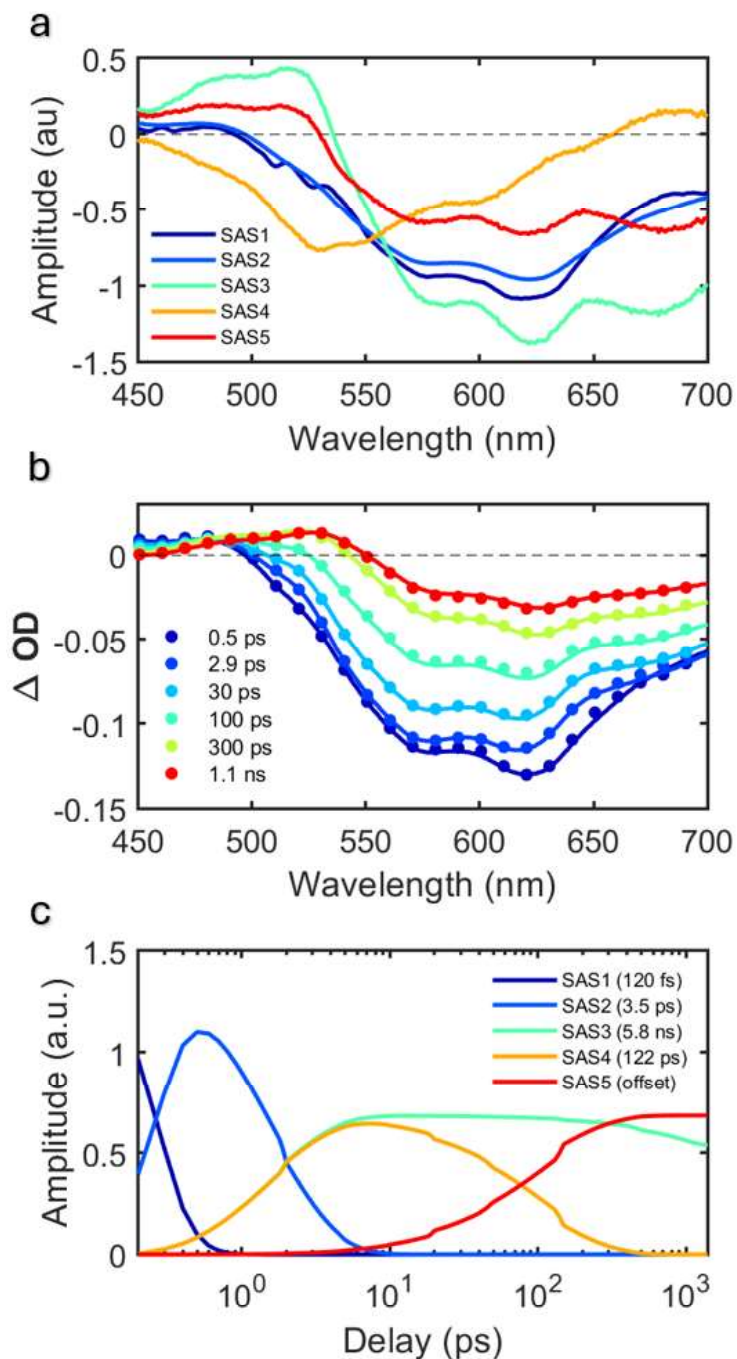
Figure 3.6: (a) SAS from the targeted analysis based on the model shown in Figure 3.5 (c) and (b) raw TA data (dots) and fit (solid traces) for ^{n}Pr-DMQA^{+} in the presence of PhB(OH)$_2$ in DMF and (c) corresponding kinetics with the delay axis on log-scale.

Target analysis of the TA data for ^nPr-DMQA$^+$ in DMF in the presence of DIPEA is summarized in Figure 3.7. The lifetimes of SAS1 and SAS2 remain nearly unchanged at 112 ± 60 fs and 3.3 ± 0.6 ps, respectively, with bleach minima situated around 625 nm, mirroring those of ^nPr-DMQA$^+$ alone. SAS3, with a lifetime of 2.0 ns (consistent with TCSPC measurements shown in Figure 3.2 (b), exhibits excited state quenching in the presence of amine. This is attributed to the introduction of additional non-radiative decay pathways [145-147]. SAS4 (assigned to ISC) has approximately the same timescale (110 ± 18 ps) as in the data for the cation alone but shows significant change in the spectral distribution. This includes a bleach minimum shift from 530 nm to 570 nm and a pronounced bleach near 610 nm. The observed quenching of the S_1 lifetime by the amine likely facilitates ISC to the triplet state [147]. This is suggested by the increased relative amplitude of SAS4 (Figure 3.7 (a)) suggesting an enhanced population transfer to the triplet state. After the triplet state is populated, an electron transfer occurs from the amine to this excited state as has been previously observed in other organic molecules [147-152]. This is further supported by the difference observed in the spectral profile of SAS5, an offset associated with the transition from T_1 to S_0, with diminished amplitude in comparison to SAS1 and SAS2 (Figure 3.7 (a)). This newly populated triplet state engages in a reaction with oxygen in solution to generate the superoxide anion.
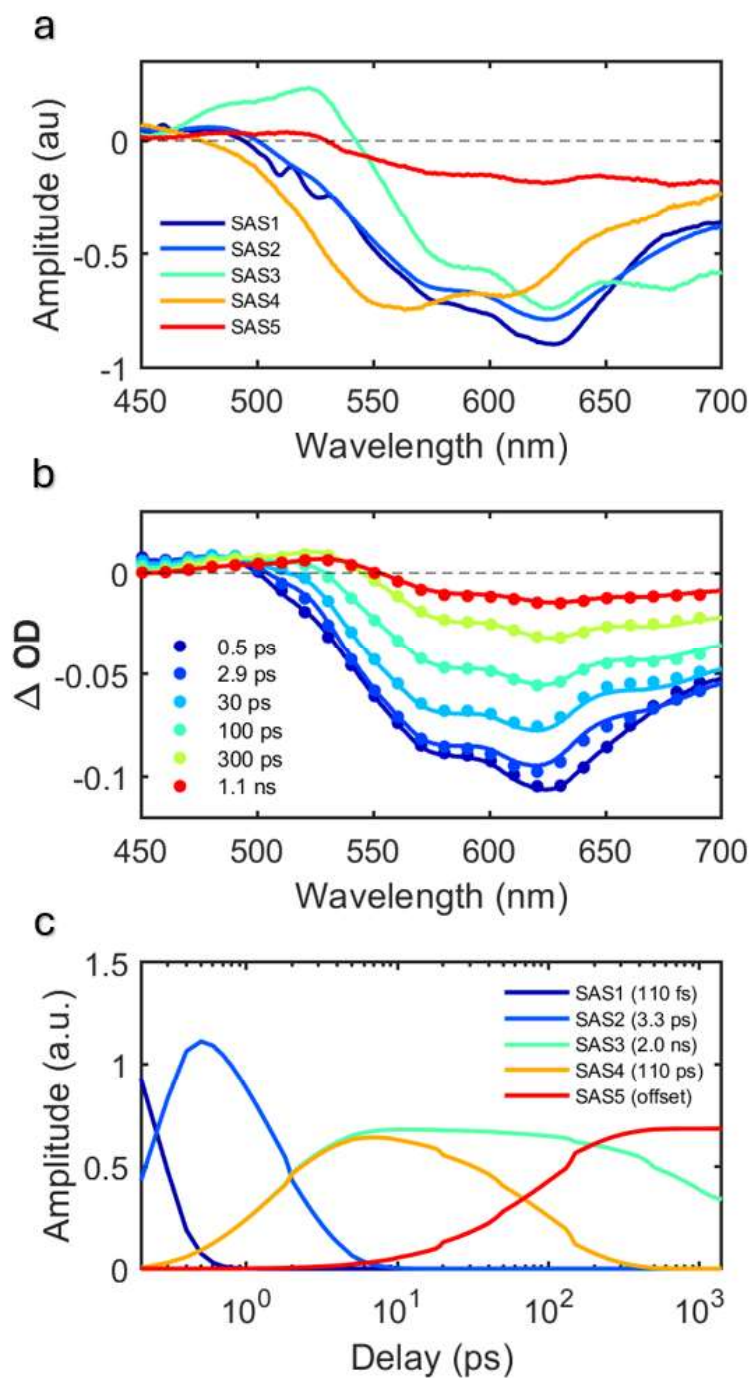
Figure 3.7: (a) SAS from the targeted analysis and (b) raw TA data (dots) and fit (solid traces) for ^{n}Pr-DMQA^{+} in the presence of DIPEA in DMF and (c) corresponding kinetics with the delay axis on log-scale.

Global target analysis of the TA data for ^{n}Pr-DMQA^{+} in DMF in the presence of PhB(OH)$_2$, and DIPEA presented in Figure 3.8 is consistent with the results from the analysis of the TA data for ^{n}Pr-DMQA^{+} and DIPEA shown in Figure 3.7. The lifetimes associated with SAS1 and SAS2 are similar to those observed for ^{n}Pr-DMQA^{+} in DMF, which indicates that solvation and IVR processes are not significantly modified by the presence of DIPEA or PhB(OH)$_2$ (see Table 3.2 in supporting information). SAS3 has a 2.0 ns timescale consistent with the TCSPC measurements shown in Figure 3.2 (a). SAS4, with a 112 ± 21 ps lifetime, has the same spectral profile as shown in Figure 3.7 (a) where DIPEA is present. This suggests that there is enhanced population transfer to the triplet state [147]. Finally, SAS5, an offset associated with the transition from T_1 to S_0, has a lower amplitude compared to the first 2 SAS, consistent with the behavior in the presence of DIPEA alone (Figure 3.7 (a)) when juxtaposed to the relative amplitude of SAS5 with respect to SAS1 and SAS2 in the cases of the cation alone in DMF or when the reagent PhB(OH)$_2$ is also present (Figure 3.5 (a) and 3.6 (a)). This suggests a depletion of the triplet state, possibly due to the formation of a radical ion-pair resulting from electron transfer from the amine to the triplet state of the photocatalyst [147] leading to the formation of superoxide anion [153]. This anion can interact with phenylboronic acid to yield phenol as the final product as previously reported [42].
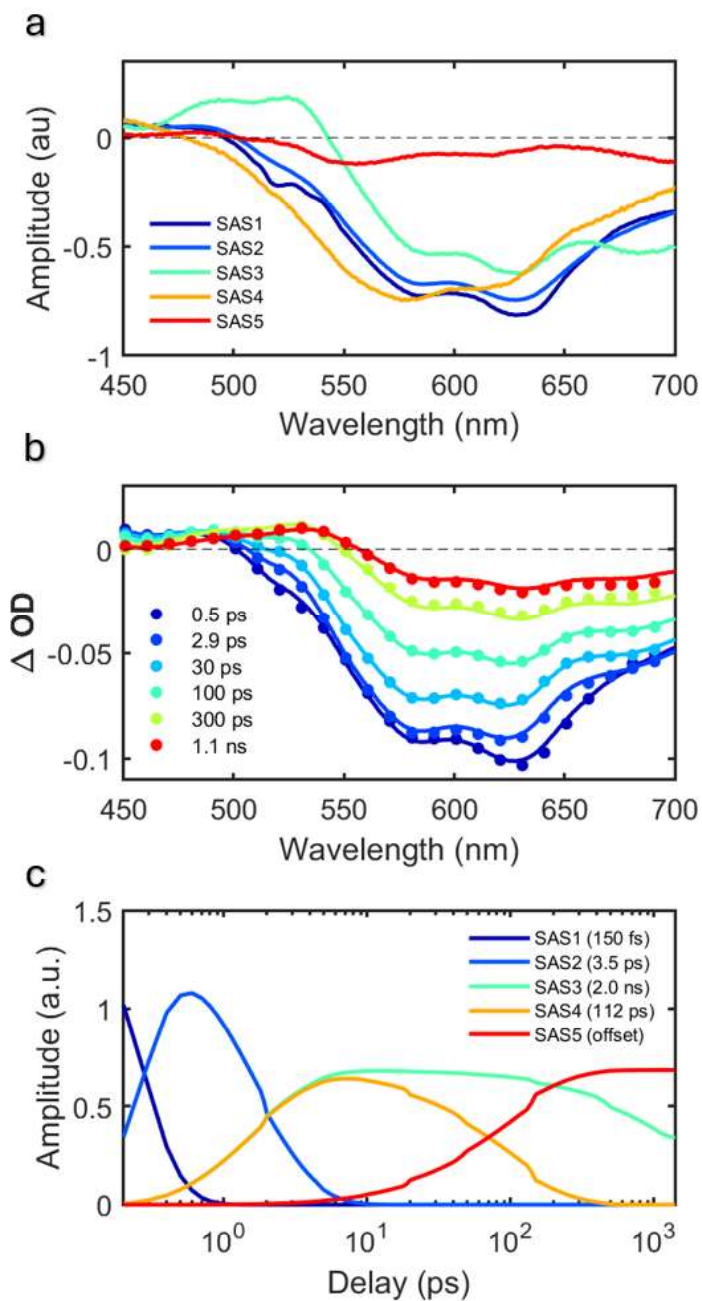
Figure 3.8: (a) SAS from the targeted analysis based on the model shown in Figure 3.5 (c), and (b) raw TA data (dots) and fit (solid traces) for ^{n}Pr-DMQA^{+} in the presence of DIPEA and phenylboronic acid in DMF and (d) corresponding kinetics for the model with the delay axis on log-scale.

Analysis of the TA and TCSPC data suggests that the aerobic hydroxylation of PhB(OH)$_2$ by ^{n}Pr-DMQA$^+$ proceeds through the triplet state as shown in Figure 3.9. The process begins with excitation to the S$_1$ state, followed by vibrational cooling and solvent reorganization. The system returns to the ground state either by radiative or non-radiative transitions from S$_1$ to S$_0$ or through ISC to triplet states followed by another ISC process from T$_1$ to S$_0$. The ISC process from S$_1$ to T$_n$ is enhanced in the presence of DIPEA and is associated with the quenching of the radiative lifetime. Kinetic analysis of the TA data supports the presence of a rapid ISC process to a higher-lying triplet state, which is close in energy to S$_1$ [138, 139, 142]. Enhanced spin-orbit coupling can be associated with a nonplanar aromatic molecular structure, with the magnitude of the enhancement being directly proportional to the deviation from planarity [123, 125]. This phenomenon has been previously observed in studies of aza[7]helicene, where the rate of ISC from S$_1$ to T$_3$ was found to be three orders of magnitude faster than that from S$_1$ to T$_1$ [133]. A similar trend has been observed for 4-dimethylaminochalcone, showing an ISC rate significantly exceeding the radiative transition [142]. Electron transfer from DIPEA (^{i}Pr$_2$NEt/^{i}Pr$_2$NEt$^{•+}$ = +0.72 V vs SCE in DMF) to an excited triplet state ($E_{1/2}$(C$^+$*/C$^•$) = +1.18 V vs SCE in DMF) [43, 147-151] can then lead to the formation of the ground state neutral DMQA radical which can subsequently reduce oxygen to superoxide radical anion under aerobic conditions [153]. Alternatively an oxidative pathway is also viable if the excited triplet state of the cationic DMQA ($E_{1/2}$ (C$^{•++}$/C$^+$*) = −0.62 V vs SCE in DMF) is oxidized under aerobic condition (O$_2$/O$_2$$^{•-}$ = −0.57 V vs SCE in DMF [43]) generating dicationic radical species of the DMQA and the superoxide radical anion. In both cases, the superoxide radical anion can then react with PhB(OH)$_2$, producing phenol through a subsequent hydrolysis step.
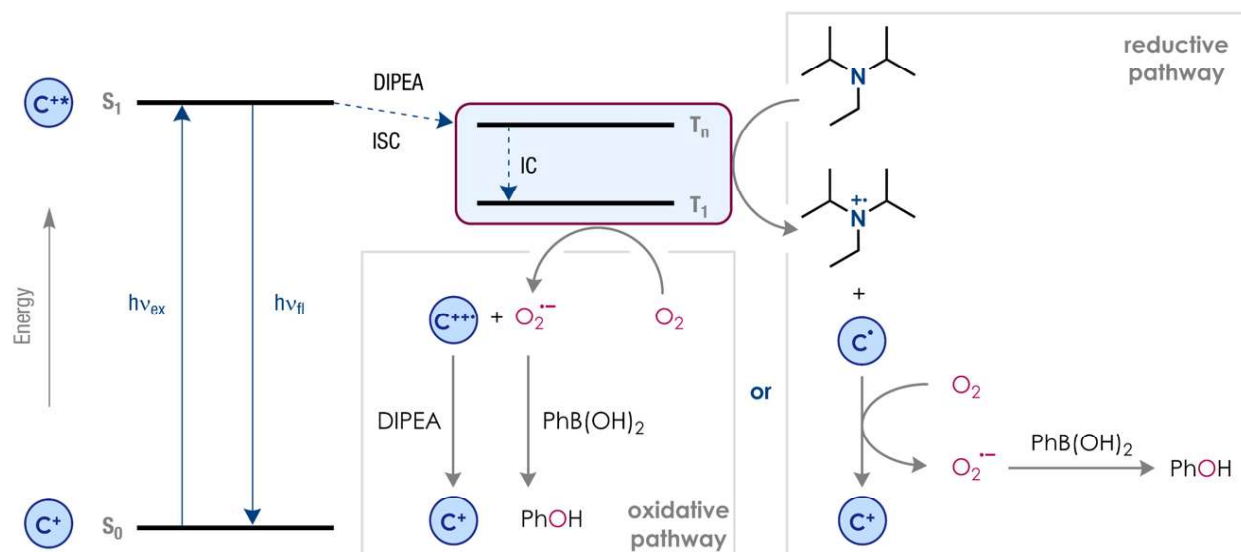
Figure 3.9: Mechanism for hydroxylation of $PhB(OH)_2$ to phenol using $^nPr\text{-DMQA}^+$ as a photoredox catalyst. DIPEA enhances the triplet population of photocatalyst due to formation of a radical ion-pair which is facilitated by electron transfer from the amine to the triplet state of the photocatalyst. Alternatively, O_2 in solution can react with the $^nPr\text{-DMQA}^+$ triplet state to form $O_2^{\bullet-}$. The oxidative reaction of $O_2^{\bullet-}$ with $PhB(OH)_2$ and subsequent hydrolysis results in the production of phenol.

3.5 Conclusion

Steady-state absorption, fluorescence spectroscopy, TCSPC, and TA data were used to study the mechanism of $^nPr\text{-DMQA}^+$ acting as a photoredox catalyst for the oxidative hydroxylation of $PhB(OH)_2$. While the absorption of $^nPr\text{-DMQA}^+$ in DMF was insensitive to the presence of either DIPEA or $PhB(OH)_2$, the fluorescence was quenched by DIPEA. TA measurements tracked the

ultrafast dynamics, revealing features consistent with rapid relaxation processes such as solvent reorganization and IVR, as well as longer-lived singlet and triplet excited states. Global target analysis of the TA data suggests that ISC is enhanced in the presence of DIPEA. This facilitates the formation of a long-lived triplet state which then can generate superoxide radical anion in two analogous pathways. This superoxide radical anion, in turn, interacts with $PhB(OH)_2$, leading to the production of phenol.

3.6 Supporting Information
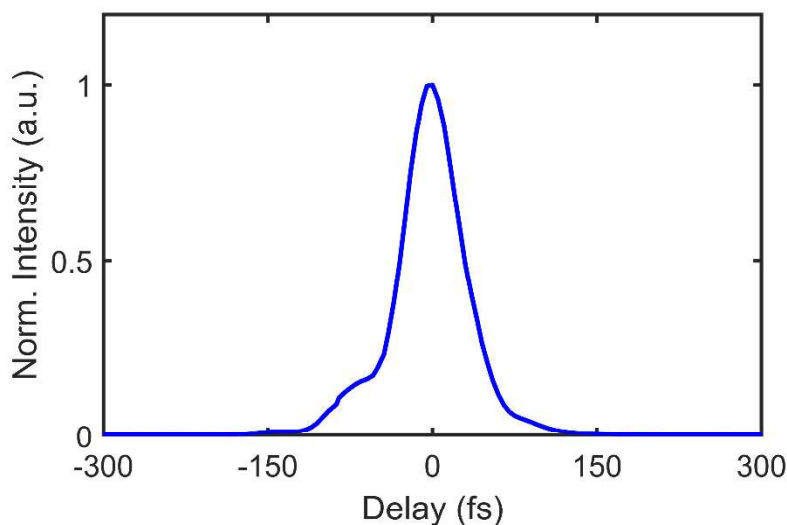
Figure 3.10: Cross-Correlation of the pump with white light probe generated by frequency doubling in a BBO crystal.
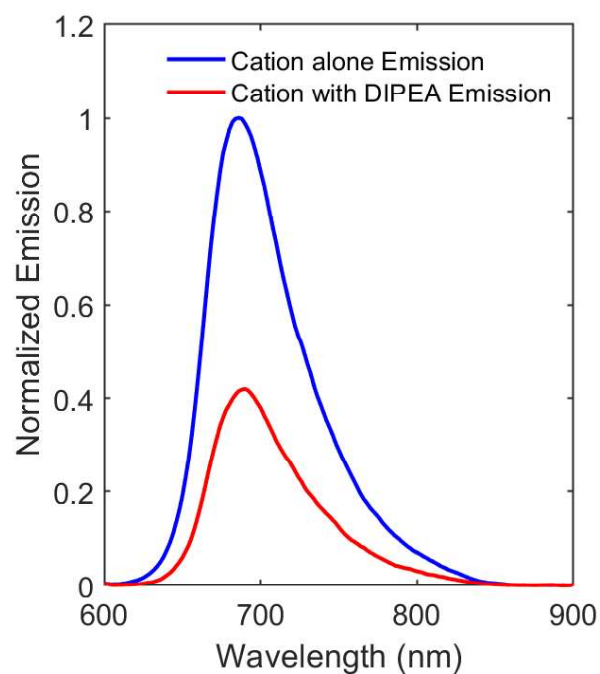
Figure 3.11: Fluorescence spectra of ^{n}Pr-DMQA^{+} alone (green trace) and with DIPEA (red trace) when normalized to the peak intensity of emission in DMF alone to show the quenching of emission in the presence of amine without a shift in the peak position.
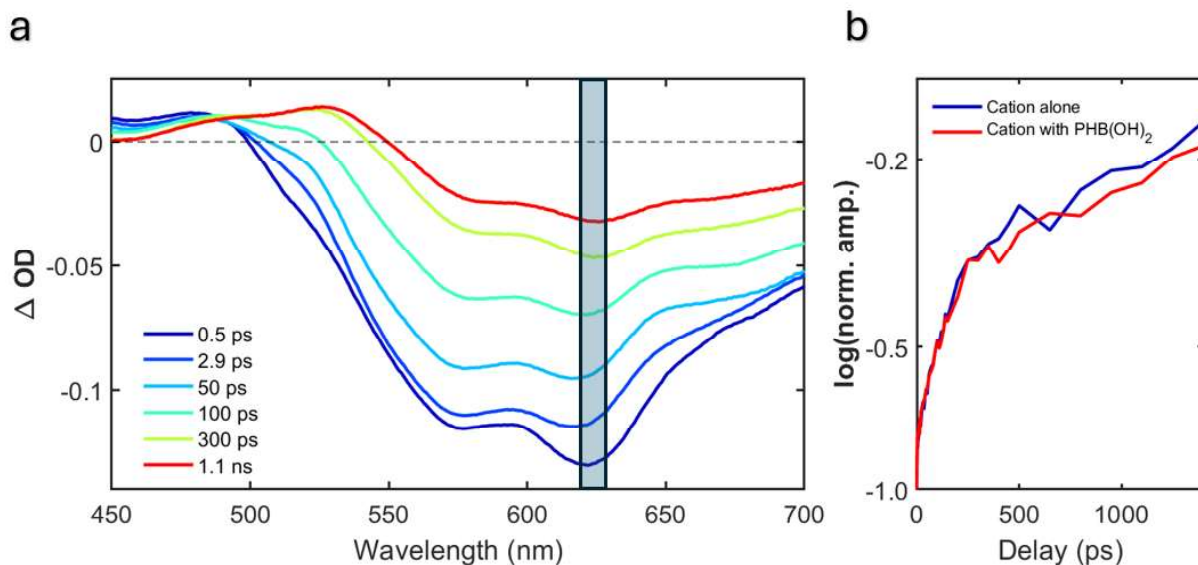
Figure 3.12: (a) TA spectral traces of ^{n}Pr-DMQA+ in the presence of PhB(OH)$_2$ with DMF being the solvent taken at different delay times. (b) Comparison between the normalized integrated traces produced after integrating the highlighted region in Figure 3.12 (a) highlighting the similar recovery of bleach rate for ^{n}Pr-DMQA+ alone (blue trace) in comparison to the presence of PhB(OH)$_2$ in DMF (red trace).
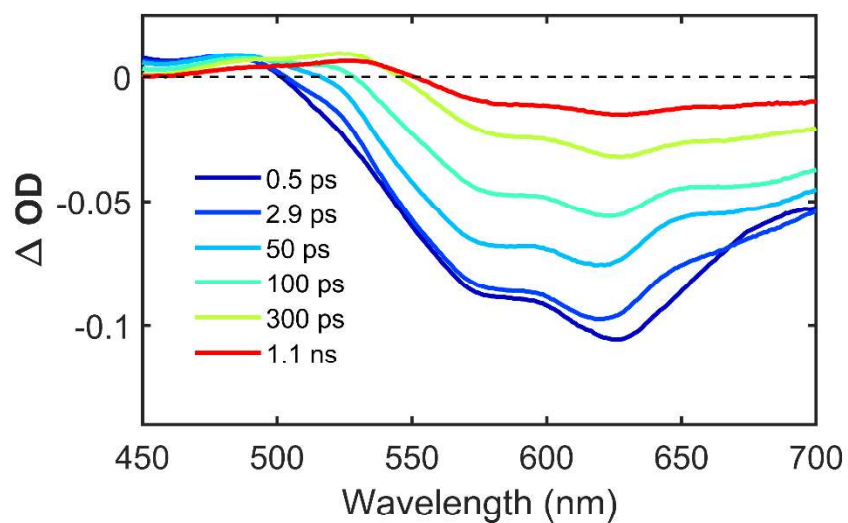
Figure 3.13: TA spectral traces of ^{n}Pr-DMQA^{+} in the presence of DIPEA with DMF being the solvent taken at different delay times.
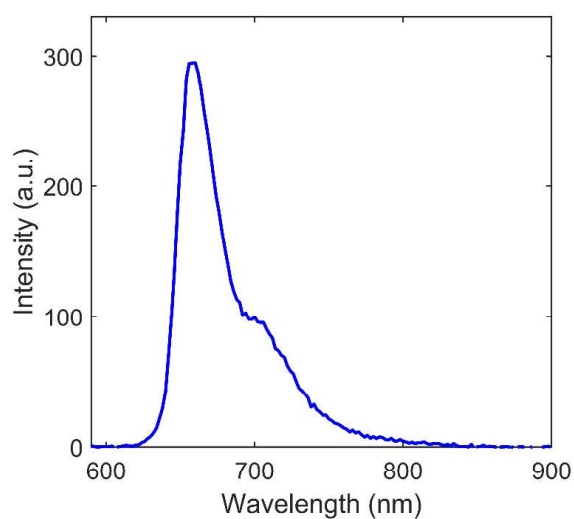
Figure 3.14: Emission from ^{n}Pr-DMQA^{+} cation at 77 K. The sample was prepared in a solution mixture of ethanol and methanol with volume ratio of 4:1.

Kinetic component	Timescale
SAS1	125 ± 60 fs
SAS2	3.5 ± 0.9 ps
SAS3	5.8 ns (from TCSPC)
SAS4	122 ± 18 ps
SAS5	$\gg 1$ ns

Table 3.1: Timescales obtained from TA data for the ^{n}Pr-DMQA^{+} cation in presence of PhB(OH)$_2$.

Kinetic component	Timescale
SAS1	150 ± 60 fs
SAS2	3.5 ± 0.9 ps
SAS3	2.0 ns (from TCSPC)
SAS4	112 ± 21 ps
SAS5	$\gg 1$ ns

Table 3.2: Timescales obtained from TA data for the ^{n}Pr-DMQA^{+} cation in presence of PhB(OH)$_2$ and DIPEA.

Chapter 4:

Ultrafast Dynamics of N,N′-di-n-propyl-1,13-dimethoxyquinacridine (*n*Pr-DMQA•) Radical: A Potent Photoredox Catalyst

4.1 Chapter Summary

This chapter delves into the photophysical properties and ultrafast dynamics of the N,N′-di-n-propyl-1,13-dimethoxyquinacridine (^{n}Pr-DMQA$^{•}$) radical, a stable neutral radical with significant implications in the field of photoredox catalysis. Employing electronic transient absorption spectroscopy, we explore the excited-state behaviors of ^{n}Pr-DMQA$^{•}$ in different solvent environments, highlighting the minimal effect of solvent polarity and role of higher lying excited state. The findings contribute to a deeper understanding of radical stability and reactivity, enriching the broader themes of the thesis by linking molecular dynamics to catalytic efficiency and offering insights that advance the development of novel photoredox systems based on organic radicals.

4.2 Introduction

Open-shell radicals that have gained significant attention in recent decades across various fields of molecular science. Open-shell radicals are prized for their unique electronic properties [31, 154-156] which are starkly different than their closed-shell counterparts [157-167] and have found applications in areas ranging from organic electronics to energy storage [168-173]. Aromatic hydrocarbon radicals have been suggested as potential contributors to the elusive diffuse interstellar bands observed in space, linking organic radical chemistry to celestial phenomena [174-177]. In the field of synthetic chemistry, the reactivity of these radicals has sparked interest in photoredox catalysis, a rapidly growing area within synthesis that leverages the unique reactivity accessible through open-shell species [162, 178-190]. Such catalysis provides a milder alternative to traditional methods, often enabling the transformation of unactivated substrates into valuable products. Despite their widespread study and application, organic radicals in liquids generally exhibit very short excited-state lifetimes [157, 163, 183, 191-199]. This rapid decay is often attributed to accessible conical intersections between the lowest excited state and the ground state [195, 200-203], a characteristic that limits their utility in some photophysical applications and underscores their dynamic nature.

Recent reports on N,N′-di-n-propyl-1,13-dimethoxyquinacridinium (^{n}Pr-DMQA$^+$) [127, 204] as organic photoredox catalyst has highlighted the role of its' oxidized and reduced radical forms as key intermediate [42, 43, 205]. The reduced neutral stable N,N′-di-n-propyl-1,13-dimethoxyquinacridine (^{n}Pr-DMQA$^•$) radical has been chemically synthesized and characterized [206, 207] and has a reduction potential < -3.4 V vs SCE [43]. The current study focuses on the excited-state dynamics of this stable neutral ^{n}Pr-DMQA$^•$ radical, exploring its photophysical

properties through electronic transient absorption (TA) spectroscopy. This approach aids in understanding the fundamental behavior of such radicals highlighting the short-lived nature of the excited state demonstrating sub-50 ps lifetime. By detailing the characterization, and dynamics of the ^{n}Pr-DMQA$^•$ radical, this chapter aims to contribute to the ongoing development of novel molecular systems with enhanced and exploitable radical properties.

4.3 Experimental Section

The preparation of the ^{n}Pr-DMQA$^•$ radical has been reported previously [206, 207]. The solutions containing the radical were prepared using solvents that had been degassed and handled within a nitrogen-filled glovebox to prevent any oxidative degradation. For optical characterization, steady-state absorption spectra were collected using an Agilent Cary 100 UV/Vis spectrometer. The experimental setup for transient absorption (TA) measurements with broadband detection, as discussed in chapter 3, was adapted to facilitate two-color experiments. This setup was powered by a Libra regenerative amplifier from Coherent, which drove an optical parametric amplifier (OPA) to produce the pump beam, while the broadband white light probe was generated through self-focusing in an argon-filled tube. The OPA output, tuned to 560 nm, was chosen to resonate with the lowest energy main visible transition of the neutral helicene radical. This light effectively excited the sample while the generated white light probe allowed for broadband detection across 450 nm to 700 nm. The temporal chirp in the OPA output was corrected using a home-built fused silica prism compression line, and paired chirped mirrors from Laser Quantum were utilized to compress the white light probe.

All transient absorption measurements were conducted at room temperature within an oxygen-free setup, housed inside a nitrogen vapor cryostat (OptistatDN). This controlled environment was critical as ^{n}Pr-DMQA$^{\bullet}$ converts back to its cationic form in the presence of oxygen. Continuous monitoring through UV-Vis absorption and fluorescence confirmed that the nitrogen environment effectively prevented oxygen intrusion for over 12 hours, well beyond the duration needed for TA measurements. The samples were maintained in a sealed 1 mm pathlength cuvette within the cryostat, with an optical density of approximately 0.5 at the excitation wavelength of 560 nm. The temporal profile of the pulses was characterized using polarization-gated frequency-resolved optical gating (PG-FROG), employing CS_2 as a non-resonant sample. The PG-FROG setup revealed a temporal pulse width of ~100 fs, ensuring precise temporal resolution for the TA experiments. The PG-FROG measurement, as shown in Figure 4.1, specifically covered the spectral range where both the pump and the probe displayed significant intensity.
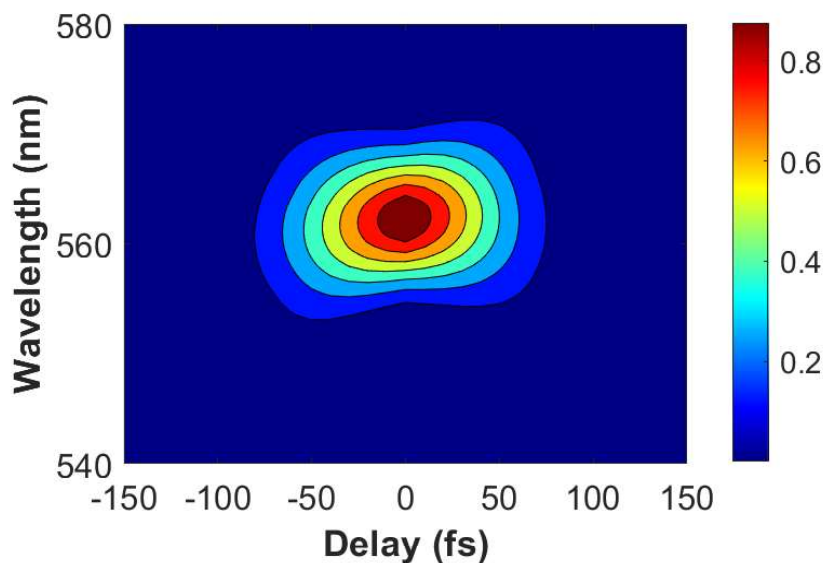
Figure 4.1: Spectrograph for retrieved pulse from PG-FROG analysis.

4.4 Result and Discussion
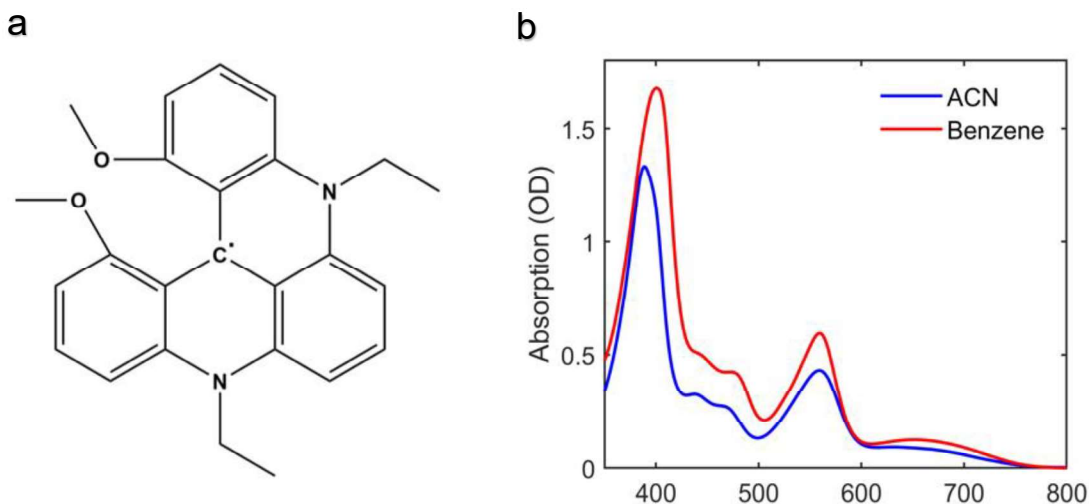
Figure 4.2: (a) Structure of N,N′-di-n-propyl-1,13-dimethoxyquinacridine (^{n}Pr-DMQA$^•$). (b) Absorption spectra of ^{n}Pr-DMQA$^•$ in acetonitrile (blue trace) and benzene (red trace). In acetonitrile, the radical has absorption features at 391 nm, 440 nm, 467 nm and 557 nm and 650 nm. In benzene, the absorption features appear at 401 nm, 445 nm, 477 nm and 559 nm and 660 nm.

Figure 4.2(a) shows the structure of the neutral open-shell doublet radical N,N′-di-n-propyl-1,13-dimethoxyquinacridine (^{n}Pr-DMQA$^•$). The absorption spectra of ^{n}Pr-DMQA$^•$ in acetonitrile (MeCN) and benzene is presented in Figure 4.2(b). The absorption spectra in both solvents are similar, indicating that the radical is relatively invariant to the solvent environments and does not display strong solvatochromism (see Figure 4.6 in supplementary information). In MeCN, ^{n}Pr-DMQA$^•$ has a relatively weak absorption near 650 nm, corresponding to the D_0 to D_1 transition.

Peaks with larger oscillator strength are present at 557 nm and 391 nm, and are attributed to D_2 and D_3 transitions, respectively. The peaks in the absorption spectrum are slightly red shifted in benzene, appearing at 401 nm, 559 nm, and 660 nm.

The ^{n}Pr-DMQA$^{\bullet}$ does not fluoresce in either MeCN or benzene due to coupling to lower lying states according to energy gap law [76] and their relatively short excited state lifetime. The lack of fluorescence has been observed for many organic radical systems [163, 196, 208-213].
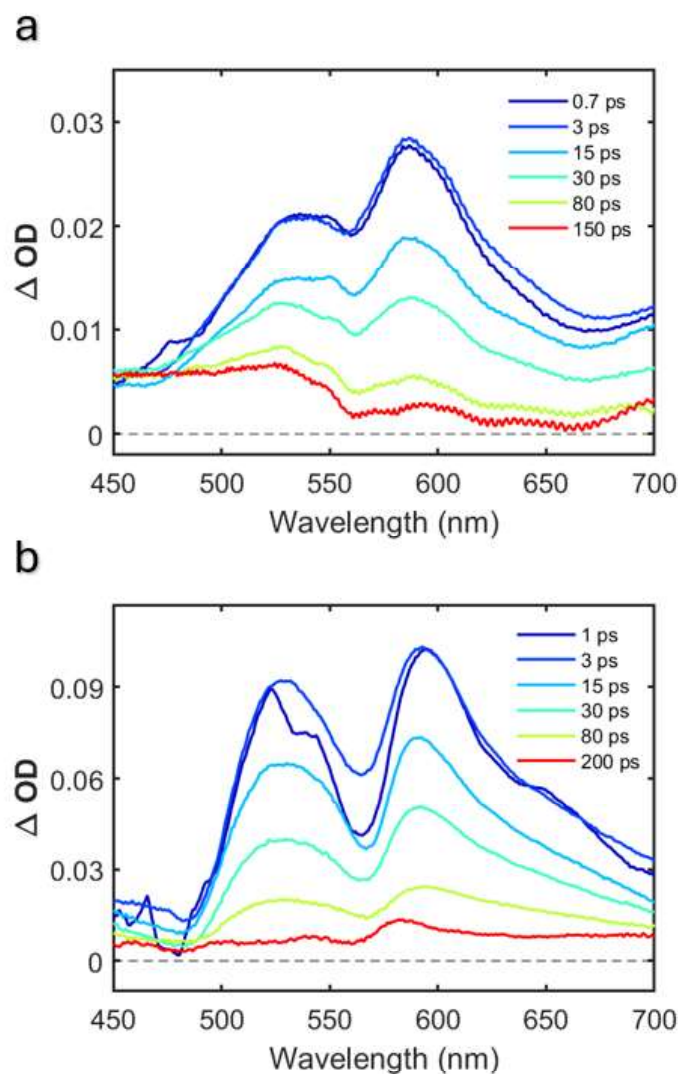
Figure 4.3: (a) Transient absorption (TA) spectral traces of ^{n}Pr-DMQA$^{\bullet}$ in acetonitrile recorded at various delay times. (b) TA data spectral traces of ^{n}Pr-DMQA$^{\bullet}$ in benzene taken at different delay times. Both data sets show similar behavior with comparatively slightly slower decay for the radical in benzene.

Transient absorption (TA) spectroscopy data was collected to measure the ultrafast dynamics of ^{n}Pr-DMQA$^\bullet$ in benzene and MeCN. The TA data in MeCN is presented in Figure 4.3(a). The pump excitation used here was at 560 nm associated with the D_2 transition as that is the lowest energy absorption feature with significant oscillator strength. Immediately following the excitation, we observe strong positive features from 450 nm to 700 nm. A negative feature associated with ground state bleach (GSB) is expected to appear at the pump wavelength, however, it is nearly completely swamped by the positive signal components, appearing only as a dip in the spectrum. The positive features here likely correspond to strong excited-state absorption (ESA) contributions, which effectively mask the bleach signal. Such an occurrence has parallels in the literature, notably in the study of the 1,3,5-triphenylverdazyl organic radical, where similar spectral behaviors were noted [208]. The ESA features, with peaks on either side of the bleach dip at ~540 nm and ~585 nm, decay on similar timescales. This suggests that relaxation from higher lying states is dominated by internal conversion. After approximately 150 ps, the TA signal has nearly returned to baseline due to fast excited state relaxation, which is expected for organic radicals in solution at room temperature [191, 196, 198, 211, 212, 214-216].

Figure 4.3(b) presents TA data for ^{n}Pr-DMQA$^\bullet$ in benzene. Benzene was chosen as a non-polar comparison to MeCN. The dynamics observed for the radical in benzene is very similar to MeCN, with the main difference appearing as a difference in amplitude between the ESA components on either side of the GSB associated dip at 560 nm and the spectral position of the peak. The ESA peaks at ~525 nm and ~590 nm on either side of the pump excitation. The similarities between ^{n}Pr-DMQA$^\bullet$ in MeCN and benzene show a relative solvent insensitivity in the time-resolved spectra in addition to the steady-state absorption. The ESA features decay by approximately 200

ps due to internal conversion, highlighting comparatively slower transition rate in nonpolar solvent.

The TA data was analyzed using the global analysis KIMOPACK package [134]. A sequential model with three components plus a background offset was used to fit the TA spectra for both MeCN and benzene solvents. Figure 4.4 presents the results of the global analysis of the TA data for ^{n}Pr-DMQA$^•$ in MeCN. We observe a fast component, characterized by a sub-120 fs timescale (not shown) most likely associated with internal conversion from higher-lying states to first excited state [212, 214]. DAS1, shown in Figure 4.4(a), has a timescale of 2.0 ± 0.3 ps (error estimates the spread based on repeat measurements under same condition) and has been assigned to intramolecular vibrational redistribution (IVR) [215, 217], consistent with evolutionary kinetics presented in Figure 4.4(d). DAS2 is associated with a timescale of 24 ± 2.0 ps, corresponds to non-radiative internal conversion to the ground state.
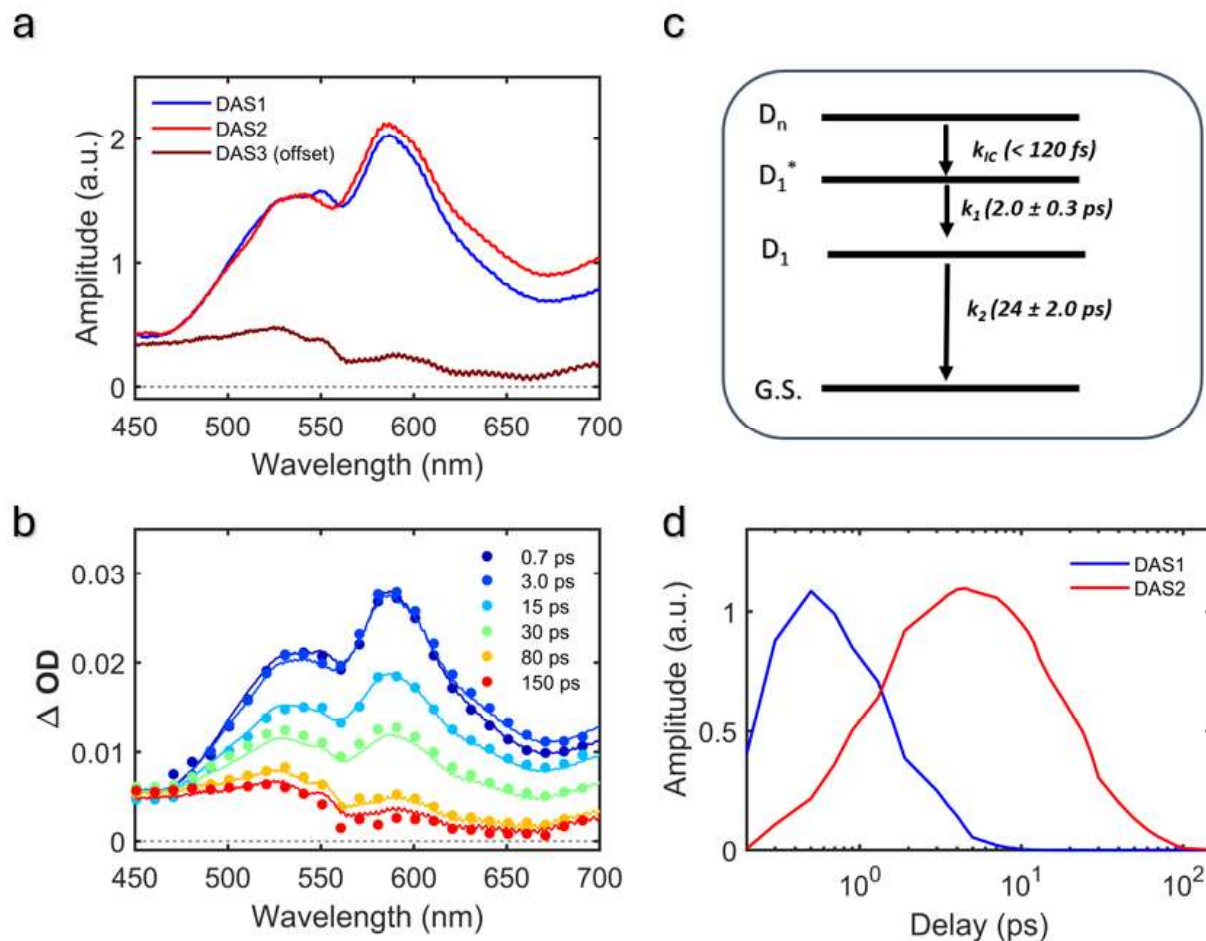
Figure 4.4: (a) Decay associated spectra (DAS) acquired through global analysis employing a sequential model for the radical in acetonitrile. (b) TA data represented with selected points and fitted traces (solid lines). (c) Kinetic model employed for the global analysis with the average timescales obtained from repeat measurements with spread represented by the error bars and (d) corresponding kinetics for the model with the delay axis presented on a log scale.
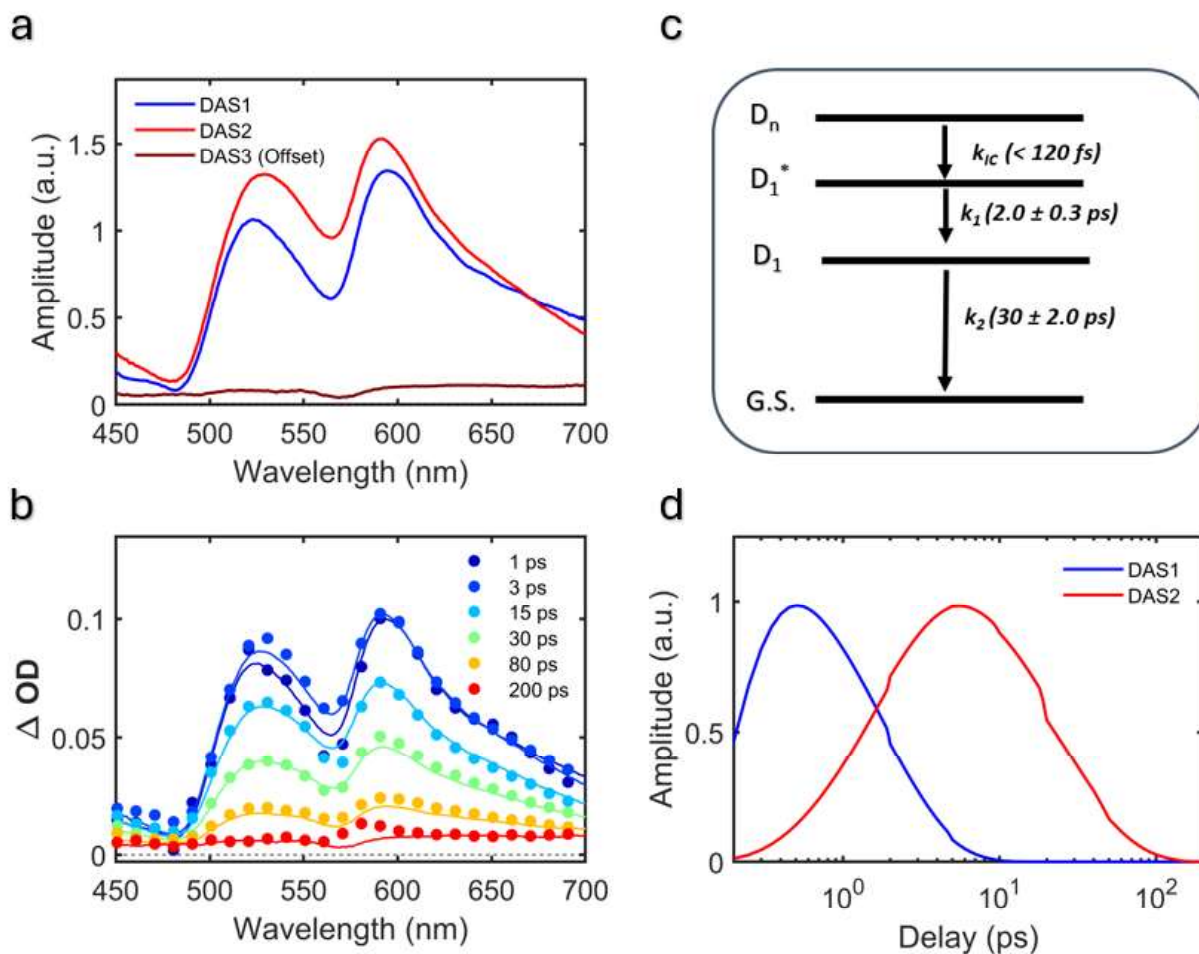
Figure 4.5: (a) Decay associated spectra (DAS) acquired through global analysis employing a sequential model for the radical in benzene. (b) TA data represented with selected points (dots) and fitted traces (solid lines). (c) Kinetic model employed for the global analysis with the average timescales obtained from repeat measurements along with spread represented by the error bars and (d) corresponding kinetics for the model with the delay axis presented on a log scale.

Figure 4.5 presents the global analysis results for ^{n}Pr-DMQA$^{\bullet}$ in benzene. As in the MeCN data, there is a sub-120 fs decay, that likely corresponds to internal conversion [212, 214]. DAS1

corresponds to intramolecular vibrational redistribution (IVR) with a lifetime of mapped 2.0 ± 0.3 ps [215, 217]. Further, DAS2 encapsulates the dynamics of the D_1 excited state's relaxation pathway, exhibiting a prolonged decay lifetime of 30 ± 2.0 ps. This represents a slightly slower excited state relaxation processes in comparison to the ones observed in the MeCN solvent environment, hence highlighting the minimal impact of solvent characteristics on the photophysical relaxation pathways of the ^{n}Pr-DMQA$^\bullet$. This observation is consistent with the lack of strong solvatochromism (see Figure 4.6 in supplementary information). Additionally, DAS3 is delineated as a component accounting for the persistent background offset.

^{n}Pr-DMQA$^\bullet$ has been reported to be an exceptionally potent photoreducing agent ($E_{1/2}^{reduction} \leq$ - 3.4 V vs SCE) [43]. Its large reduction potential in combination with the fast internal conversion and short excited state lifetime in MeCN and benzene observed from the TA data suggests that it may form a closed-shell Meisenheimer complex. This concept, as demonstrated by Rieth et al. in their investigation of naphthalene monoamide [211], reveals that such complexes can act as strongly reducing photoreagents with extended excited-state lifetimes. The Meisenheimer complex's excited-state lifetime extending beyond a nanosecond, a timescale typical for diffusion-limited processes driving molecular encounters in solution at typical reagent concentrations (~ 0.1 M), could explain the radical's high photoreduction potential despite rapid decay processes [211]. These insights into the ^{n}Pr-DMQA$^\bullet$'s photophysical and photocatalytic properties underscore its significant potential in applications requiring high photoreduction capabilities, bridging the gap between rapid photophysical processes and the demands of efficient photocatalytic reactions.

4.5 Conclusion

The investigation of the ^{n}Pr-DMQA$^{\bullet}$ radical has provided significant insights into its photophysical behavior and hence its utility in photoredox catalysis. The absorption spectra of ^{n}Pr-DMQA$^{\bullet}$ in both acetonitrile and benzene show relatively invariant features, indicating limited solvatochromism. Transient absorption spectroscopy has confirmed that the excited state lifetimes of ^{n}Pr-DMQA$^{\bullet}$ are remarkably short, under 50 ps in both solvents, which is consistent with rapid internal conversion processes observed in similar organic radicals. The global analysis of the transient absorption data elucidated the presence of intramolecular vibrational redistribution and non-radiative internal conversion processes from higher lying doublet states, with solvent-dependent relaxation timescales from first excited state. The observed behavior suggests that ^{n}Pr-DMQA$^{\bullet}$ may form closed-shell Meisenheimer complexes with long lived excited state hence mitigating the diffusion limit barrier required to overcome for molecular encounters, contributing to its potent photoreducing capabilities.

4.6 Supplementary Information
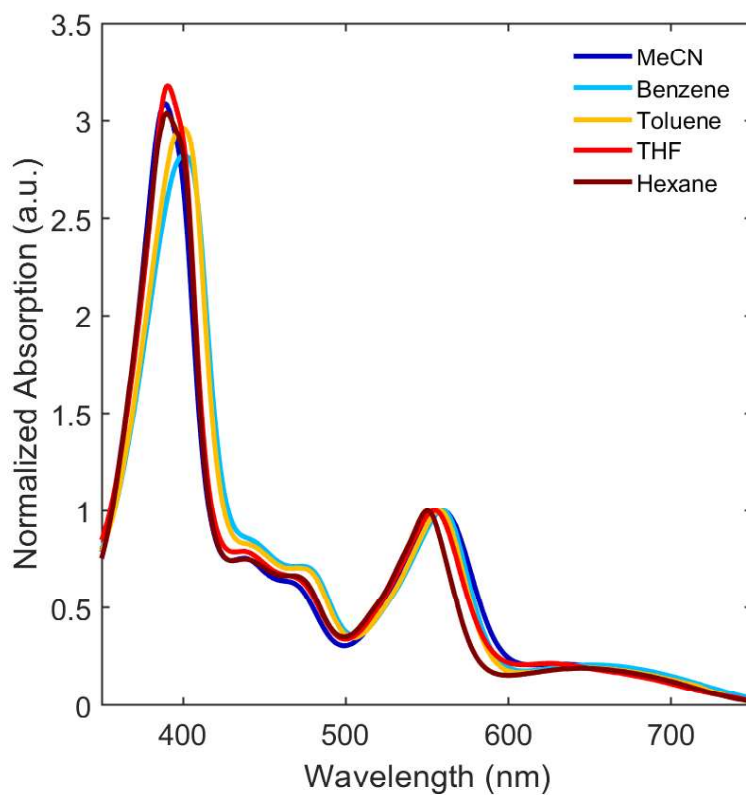
Figure 4.6: Absorption solvatochromism of ^{n}Pr-DMQA$^•$ radical in various solvents - acetonitrile (blue), benzene (cyan), toluene (orange), THF (red), and hexane (brown). All absorption traces are normalized to the peak around 560 nm.

Chapter 5:

Summary and Conclusion

This thesis explored the intricate dynamics and structural characteristics of various molecular systems through detailed optical spectroscopy studies, providing deep insights into the fundamental processes within metal-ligand complexes and organic photoredox species. These investigations highlight the versatility of optical spectroscopy in elucidating not only photoredox catalysis processes but also the fundamental nature of electronic coupling and excited state behaviors essential for understanding broader chemical phenomena. The interplay between electronic properties and catalytic behavior has been thoroughly examined, contributing to a more comprehensive understanding of the photophysics involved in these molecules. The main findings from each chapter are summarized in the following paragraphs.

Chapter 2 delved into the distinctive spin-driven dynamics of the TD1-Cu complex, examining its behavior in both monomeric and dimeric forms through temperature-dependent two-dimensional electronic spectroscopy (2DES). This investigation revealed that the formation of spin-coupled excitonic dimer form, mediated by ferromagnetic and antiferromagnetic interactions, leads to long-lived excited states in contrast to the short-lived nature of the monomer form. The study effectively highlights how the TD1-Cu complex serves as a prototype for exploring spin-mediated electronic dynamics in metal-organic frameworks, opening pathways for the development of advanced materials with tunable photophysical properties as well as applications in the field of spin dynamics, photoredox catalysis and redox chemistry.

Chapter 3 provided a comprehensive examination of the ultrafast dynamics of the ^{n}Pr-DMQA^{+} cation, a helical carbenium red-light activated organic photocatalyst utilized in the oxidative hydroxylation of phenylboronic acid. Through advanced optical spectroscopy techniques such as transient absorption (TA) and time-correlated single photon counting (TCSPC), this chapter

illuminated the critical role of the long-lived triplet state of ^{n}Pr-DMQA$^+$ in facilitating electron transfer processes essential for catalytic activity. The findings underscored the influence of sacrificial amines in modulating the photocatalyst's excited state dynamics, leading to significant quenching effects and demonstrating the amine's pivotal role as electron donor in the reaction mechanism. This detailed exploration of the ^{n}Pr-DMQA$^+$ cation's behavior not only advances our understanding of its photophysical properties but also contributes valuable insights into designing more efficient photoredox systems for sustainable chemical synthesis.

Chapter 4 explored the photophysical properties of the N,N′-di-n-propyl-1,13-dimethoxyquinacridine (^{n}Pr-DMQA$^•$) radical, a stable neutral radical used as an extreme photoredox catalyst. Utilizing transient absorption (TA) spectroscopy, the study provided detailed insights into the short-lived excited states of this radical, with lifetimes demonstrating sub-50 ps decay across different solvents. This understanding is crucial for advancing the use of organic radicals in photoredox catalysis despite short-lived excited state, offering pathways to enhance reaction efficiencies and expand the scope of photoredox applications in organic synthesis.

In conclusion, this thesis has underscored the instrumental role of optical spectroscopy in deciphering the intricate photophysical and photochemical mechanisms at the heart of innovative catalytic systems. From intricate metal-ligand complexes to sophisticated organic photoredox molecules, this research has illuminated the critical function of time-resolved spectroscopy in dissecting the complex behaviors inherent in these systems. It is anticipated that the methodologies and insights gained here will provide a platform for future research aimed at developing new catalytic systems with optimized performance and broader applicability.

Appendix:

MATLAB Scripts

A.1 CCD Calibration Using Atomic Line Lamps

```matlab
clear

%read file
filestr = fileread('filename');

filebyline = regexp(filestr, '\n', 'split');
filebyline( cellfun(@isempty,filebyline) ) = [];
filebyfield = regexp(filebyline, '\n', 'split');

%pad out so each line has the same number of fields
numfields = cellfun(@length, filebyfield);
maxfields = max(numfields);
fieldpattern = repmat({[]}, 1, maxfields);
firstN = @(S,N) S(1:N);
filebyfield = cellfun(@(S) firstN([S,fieldpattern], maxfields), filebyfield,
'Uniform', 0);

fieldarray = vertcat(filebyfield{:});


len = 15; %length = size for each coherent time repeat
num_waveforms = 1;
pro = (len-2)*num_waveforms;
ccd = zeros(pro,1340);
k =1;

for i = 1:num_waveforms
    for m = 3:len-1
        b = len*(i-1)+m;
        data = fieldarray{b}(:,:);
        ccd(k,:) = str2num(data);
        k = k+1;
    end
end

avg = zeros(num_waveforms,1340);

a = len-3; % # of images taken at each coherent time excluding the first image

for i = 1:num_waveforms
```

```matlab
    for m = 0:a-1
        avg(i,:) = ccd(a*i-m,:)+avg(i,:);
    end
    avg(i,:) = avg(i,:)/a;
end


calibration = avg;


figure(2)
plot(calibration)
% This is to select the peaks index from the collected data and corresponding
wavelength values from atomic lamp data.
```

Generating Calibration based on selected peaks

```matlab
column = 1:1340;
wlen = zeros(1,1340);


pixel = [389; 654; 731; 1014]; %% From the selected peaks from Figure(2)
wavelength = [435.8335; 546.075; 578.06; 696.54];
f1 = fit(pixel,wavelength,'poly3'); % using cubic fitting to generate
calibration file.
coeff = coeffvalues(f1);
for i = 1:1340
        wlen(1,i) = coeff(1)*(column(i))^3 + coeff(2)*(column(i))^2 +
coeff(3)*column(i) + coeff(4);
end
```

Saving the calibration file

```matlab
save('calibrated_frequency_axis_23_09_19', 'wlen', '-ascii', '-double', '-
tabs');
```

A.2 Plotting 2D emission with varying excitation wavelengths

```
clear;

data = readtable('test1.csv'); % replace "test1.csv" with the filename of the
data

data_all = table2array(data);
axis_emission = data_all(:,1);
data_2D = data_all(:,2:2:end);

axis_excitation = 200:5:750; % Making the excitation axis based on the
excitation data collection setup
```

Contour on logscale

```
plotmin = min(min(data_2D));
plotmax = max(max(data_2D));
log2_values = 1:log2(plotmax)/15:log2(plotmax);
cline = [plotmin 0 2.^log2_values];

nidx = 1;
nfig = figure(nidx+0);
hold off;
contourf(axis_excitation,axis_emission,data_2D, cline); colormap("jet");
xlabel ('Ex. Wavelength (nm)'); ylabel ('Em. Wavelength (nm)'); colorbar;
set(gca,'FontSize',15, 'TickDir', 'out', 'LineWidth', 1);
axis equal tight;
set(gca,'Layer', 'top');
set(gca,'TickDir','in');
box on;
```

Saving the plots

```
saveas(nfig,'filename_V1.fig');
saveas(nfig,'filename_V1.png');
```

A.3 Generating Input Data File for Global Analysis Using KIMOPACK

```matlab
wlen = wlen'; % wavelength axis

Time = Taxis; % delay axis from raw data
ta_input_data = plot_2D'; % TA data used for surface plot
kimo_inputdata = zeros(length(Taxis)+1,length(wlen)+1);

for i = 1:length(Taxis)+1
    for j = 1:length(wlen)+1
        if i == 1 && j == 1
            kimo_inputdata(i,j) = 0;
        elseif i == 1 && j > 1
            kimo_inputdata(1,j) = wlen(j-1);
        elseif j == 1 && i > 1
            kimo_inputdata(i,1) = Time(i-1)/1000;
        else
            kimo_inputdata(i,j) = ta_input_data(i-1,j-1);
        end
    end
end


save('input_KiMoPack_V1','kimo_inputdata', '-ascii', '-double', '-tabs');
```

A.4 Plotting GLOBAL ANALYSIS output from KIMOPACK

```matlab
clear; clc;

das = readtable('DAC.txt'); % DAS/SAS input data
das = table2array(das);

measured_matrix = readtable('measured_matrix.txt'); % Raw TA input data after
chirp correction
measured_matrix = table2array(measured_matrix);

calculated_matrix = table2array(readtable('calculated_matrix.txt'));
% Calculated TA matrix

concentration = table2array(readtable('concentration_temporal_evolution.txt'));
% Concentration evolution of kinetic components

time = table2array(readtable('Taxis.txt')); % Delay axis

lambda = measured_matrix(1,:); % Detection wavelength

taxis_fit = time(length(time)+2-size(measured_matrix,1):end); % delay axis
correct to match time axis used for global analysis
```

Plotting DAS

```matlab
axes_font = 15; linwdth = 3.5;
c_idx = 4;

DAS_fig = figure(7);
hold off;

cc = jet(8);
plot(lambda,das(2:end,1)/1e9,'LineWidth',linwdth,'Color',cc(1,:))   % 1E9 is a
scaling factor
hold on;
plot(lambda,das(2:end,2)/1e9,'LineWidth',linwdth,'Color',cc(3,:))
plot(lambda,das(2:end,3)/1e9,'LineWidth',linwdth,'Color',cc(6,:))
plot(lambda,das(2:end,4)/1e9,'LineWidth',linwdth,'Color',cc(8,:))
```

```matlab
plot([450 710],[0 0],'--','LineWidth',linwdth-2,'Color',[0 0 0])

ylabel('DAS');
xlabel('Wavelength (nm)');
xlim([450 700]);
set(gca,'FontSize',axes_font, 'TickDir', 'in', 'LineWidth', 1.5);
legend('A (0.12 ps)', 'B (1.8 ps', 'C (23.9 ps)','D (non decaying)'); % Example
used for legend
legend boxoff;

saveas(DAS_fig,'DAS_XYZ_V1.fig');
saveas(DAS_fig,'DAS_XYZ_V1.png');
```

Plotting Measured Matrix and Calculated Matrix with Error

```matlab
fig_idx_matrix = 8^5;
linewdth = 2; axes_font = 15;
cline = 20;
Matrix_Plot = figure(fig_idx_matrix);
hold off;

subplot(1,2,1)
plot_2D = measured_matrix(2:end,:); % Plotting raw data
contourf(lambda,taxis_fit/1000,plot_2D,cline,'LineStyle','-');
colormap(jet); colorbar;
xlabel('Wavelength (nm)','Interpreter','Latex','fontweight','bold');
ylabel('Delay (ps)','Interpreter','Latex','fontweight','bold');
hold off;
xlim([450 700]);
yticks([1 10 100 1000]);
title('Measured (A)')
set(gca, 'YScale', 'log')
set(gca,'FontSize',axes_font, 'TickDir', 'in', 'LineWidth', 1);

subplot(1,2,2)
plot_2D = calculated_matrix(2:end,:); % Plotting calculated data
contourf(lambda,taxis_fit/1000,plot_2D,cline,'LineStyle','-');
colormap(jet); colorbar;
xlabel('Wavelength (nm)','Interpreter','Latex','fontweight','bold');
ylabel('Delay (ps)','Interpreter','Latex','fontweight','bold');
hold off;
xlim([450 700]);
```

```matlab
yticks([1 10 100 1000]);
title('Calculated (B)')
set(gca, 'YScale', 'log')
set(gca,'FontSize',axes_font, 'TickDir', 'in', 'LineWidth', 1);

subplot(1,3,3)
plot_2D = 10*(measured_matrix(2:end,:) - calculated_matrix(2:end,:)); %
Plotting 10*(Measured - Calculated)
contourf(lambda,taxis_fit/1000,plot_2D,cline,'LineStyle','-');
colormap(jet); colorbar;
xlabel('Wavelength (nm)','Interpreter','Latex','fontweight','bold');
ylabel('Delay (ps)','Interpreter','Latex','fontweight','bold');
hold off;
xlim([450 700]);
yticks([1 10 100 1000]);
title('10*(A-B)')
set(gca, 'YScale', 'log')
set(gca,'FontSize',axes_font, 'TickDir', 'in', 'LineWidth', 1);

saveas(Matrix_Plot,'Comparison_Matrix_XYZ_TA_V1.fig');
saveas(Matrix_Plot,'Comparison_Matrix_XYZ_TA_V1.png');
```

Plotting Kinetic Traces

```matlab
s_reg = [500,520,590,610]; % example of spectral region of interest
l1_idx = find(lambda > s_reg(1)-2 & lambda < s_reg(1)+2);
l2_idx = find(lambda > s_reg(2)-2 & lambda < s_reg(2)+2);
l3_idx = find(lambda > s_reg(3)-2 & lambda < s_reg(3)+2);
l4_idx = find(lambda > s_reg(4)-2 & lambda < s_reg(4)+2);

% Generating kinetic traces from measured matrix
k1_raw = sum(measured_matrix(2:end,l1_idx-2:l1_idx+2)/5,2);
k2_raw = sum(measured_matrix(2:end,l2_idx-2:l2_idx+2)/5,2);
k3_raw = sum(measured_matrix(2:end,l3_idx-2:l3_idx+2)/5,2);
k4_raw = sum(measured_matrix(2:end,l4_idx-2:l4_idx+2)/5,2);

% Generating kinetic traces from CALCULATED matrix
k1_cal = sum(calculated_matrix(2:end,l1_idx-2:l1_idx+2)/5,2);
k2_cal = sum(calculated_matrix(2:end,l2_idx-2:l2_idx+2)/5,2);
k3_cal = sum(calculated_matrix(2:end,l3_idx-2:l3_idx+2)/5,2);
k4_cal = sum(calculated_matrix(2:end,l4_idx-2:l4_idx+2)/5,2);
```

```matlab
axes_font = 18; linwdth = 3;
marker = 18; cc = jet(11);
kinetic_trace_fig = figure(9^4 + 7);
hold off;
plot(taxis_fit/1000,k1_raw,'.','MarkerSize',marker,'Color',cc(1,:))
hold on;
plot(taxis_fit/1000,k1_cal,'LineWidth',linwdth,'Color',cc(1,:))
plot(taxis_fit/1000,k2_raw,'.','MarkerSize',marker,'Color',cc(4,:))
plot(taxis_fit/1000,k2_cal,'LineWidth',linwdth,'Color',cc(4,:))
plot(taxis_fit/1000,k3_raw,'.','MarkerSize',marker,'Color',cc(7,:))
plot(taxis_fit/1000,k3_cal,'LineWidth',linwdth,'Color',cc(7,:))
plot(taxis_fit/1000,k4_raw,'.','MarkerSize',marker,'Color',cc(11,:))
plot(taxis_fit/1000,k4_cal,'LineWidth',linwdth,'Color',cc(11,:))
plot([.01 1400],[0 0],'--','LineWidth',linwdth-2,'Color',[0 0 0])
ylabel('Amplitude (au)');
xlabel('Delay (ps)');
xticks([1 10 100 1000]);
set(gca, 'XScale', 'log'); % x-axis on log-scale

set(gca,'FontSize',axes_font, 'TickDir', 'in', 'LineWidth', 1.5);
legend('500 nm','','520 nm','','590 nm','','610 nm'); legend boxoff;

saveas(kinetic_trace_fig,'log_kinetic_trace_XYZ_V1.fig');
saveas(kinetic_trace_fig,'log_kinetic_trace_XYZ_V1.png');
```

Plotting Spectral traces

```matlab
t_reg = [0.5 2.9 50 100 300 1100]; % example for selecting temporal region for
plotting traces
taxis = taxis_fit/1000;

t1_idx = find(taxis == t_reg(1));
t2_idx = find(taxis == t_reg(2));
t3_idx = find(taxis == t_reg(3));
t4_idx = find(taxis == t_reg(4));
t5_idx = find(taxis == t_reg(5));
t6_idx = find(taxis == t_reg(6));

axes_font = 14; linwdth = 2;
marker = 20; cc = jet(16);
spectral_trace_fig = figure(10^4 + 7 + 100 + 100);
hold off;
```

```matlab
 plot(lambda(1:3:end),measured_matrix(t1_idx+1,1:3:end),'.','MarkerSize',marker,
'Color',cc(1,:))
 hold on;
 plot(lambda,calculated_matrix(t1_idx+1,:),'LineWidth',linwdth,'Color',cc(1,:))
 plot(lambda(1:3:end),measured_matrix(t2_idx+1,1:3:end),'.','MarkerSize',marker,
'Color',cc(3,:))
 plot(lambda,calculated_matrix(t2_idx+1,:),'LineWidth',linwdth,'Color',cc(3,:))
 plot(lambda(1:3:end),measured_matrix(t3_idx+1,1:3:end),'.','MarkerSize',marker,
'Color',cc(5,:))
 plot(lambda,calculated_matrix(t3_idx+1,:),'LineWidth',linwdth,'Color',cc(5,:))
 plot(lambda(1:3:end),measured_matrix(t4_idx+1,1:3:end),'.','MarkerSize',marker,
'Color',cc(7,:))
 plot(lambda,calculated_matrix(t4_idx+1,:),'LineWidth',linwdth,'Color',cc(7,:))
 plot(lambda(1:3:end),measured_matrix(t5_idx+1,1:3:end),'.','MarkerSize',marker,
'Color',cc(9,:))
 plot(lambda,calculated_matrix(t5_idx+1,:),'LineWidth',linwdth,'Color',cc(9,:))
 plot(lambda(1:3:end),measured_matrix(t6_idx+1,1:3:end),'.','MarkerSize',marker,
'Color',cc(14,:))
 plot(lambda,calculated_matrix(t6_idx+1,:),'LineWidth',linwdth,'Color',cc(14,:))
 plot([450 700],[0 0],'--','LineWidth',linwdth-2,'Color',[0 0 0])

 ylabel('\Delta OD','fontweight','bold');
 xlabel('Wavelength (nm)');
 xlim([450 700]);
 set(gca, 'YScale', 'linear')
 set(gca,'FontSize',axes_font, 'TickDir', 'in', 'LineWidth', 1.5);
 legend('0.5 ps','','2.9 ps','','50 ps','','100 ps','','300 ps','','1.1 ns');
legend boxoff;

 saveas(spectral_trace_fig,'spectral_trace_XYZ_V1.fig');
 saveas(spectral_trace_fig,'spectral_trace_XYZ_V1.png');
```

Concentration Profile as a function of time delay

```matlab
 axes_font = 18; linwdth = 4;
 marker = 18; cc = jet(8);
 concentration_fig = figure(9^5 + 7);
 hold off;

 plot(taxis_fit/1000,concentration(2:end,1)/1e-
11,3,'LineWidth',linwdth,'Color',cc(1,:)) % 1E-11 is a scaling factor
 hold on;
```

```matlab
 plot(taxis_fit/1000,concentration(2:end,2)/1e-
11,3,'LineWidth',linwdth,'Color',cc(3,:))
 plot(taxis_fit/1000,concentration(2:end,3)/1e-
11,3,'LineWidth',linwdth,'Color',cc(6,:))

 ylabel('a.u.');
 xlabel('Delay (ps)');
 xticks([1 10 100 1000])
 set(gca, 'XScale', 'log')
 set(gca,'FontSize',axes_font, 'TickDir', 'in', 'LineWidth', 1.5);
 legend('A (0.12 ps)', 'B (1.8 ps', 'C (23.9 ps)');  % Example of legend
 legend boxoff;

 saveas(concentration_fig,'concent_XYZ_V1.fig');
 saveas(concentration_fig,'concent_XYZ_V1.png');
```

References

1.   Li, L., C.R. Prindle, W. Shi, C. Nuckolls, and L. Venkataraman, Radical Single-Molecule Junctions. *Journal of the American Chemical Society*, 2023. **145**(33): p. 18182-18204.

2.   Mizuno, A., R. Matsuoka, T. Mibu, and T. Kusamoto, Luminescent Radicals. *Chemical Reviews*, 2024. **124**(3): p. 1034-1121.

3.   Tomat, E. and C.J. Curtis, Biopyrrin Pigments: From Heme Metabolites to Redox-Active Ligands and Luminescent Radicals. *Accounts of Chemical Research*, 2021. **54**(24): p. 4584-4594.

4.   Day, P., A.E. Underhill, T.R. Society, and P. Hurst, Metal-Organic and Organic Molecular Magnets. 2007: *Royal Society of Chemistry*.

5.   Linert, W. and M. Verdaguer, Molecular Magnets Recent Highlights. 2012: *Springer Science & Business Media*.

6.   Makarova, T. and F. Palacio, Carbon Based Magnetism: An Overview of the Magnetism of Metal Free Carbon-based Compounds and Materials. 2006: *Elsevier Science*.

7.   Ratera, I. and J. Veciana, Playing with Organic Radicals as Building Blocks for Functional Molecular Materials. *Chemical Society Reviews*, 2012. **41**(1): p. 303-349.

8.   Ju, M., Z. Lu, L.F.T. Novaes, J.I. Martinez Alvarado, and S. Lin, Frustrated Radical Pairs in Organic Synthesis. *Journal of the American Chemical Society*, 2023. **145**(36): p. 19478-19489.

9.   Matyjaszewski, K. and J. Xia, Atom Transfer Radical Polymerization. *Chemical Reviews*, 2001. **101**(9): p. 2921-2990.

10.   Phaniendra, A., D.B. Jestadi, and L. Periyasamy, Free Radicals: Properties, Sources, Targets, and Their Implication in Various Diseases. *Indian J Clin Biochem*, 2015. **30**(1): p. 11-26.

11.   Koivisto, B.D. and R.G. Hicks, The Magnetochemistry of Verdazyl Radical-Based Materials. *Coordination Chemistry Reviews*, 2005. **249**(23): p. 2612-2630.

12.   Efthymiou, C., M. Winterlich, and C. Papatriantafyllopoulou, Breakthrough in Radical-Bridged Single-molecule Magnets, in *Single-Molecule Magnets*. 2018. p. 315-351.

13.   Gansäuer, A. and H. Bluhm, Reagent-Controlled Transition-Metal-Catalyzed Radical Reactions. *Chemical Reviews*, 2000. **100**(8): p. 2771-2788.

14.   Himo, F., L.A. Eriksson, F. Maseras, and P.E.M. Siegbahn, Catalytic Mechanism of Galactose Oxidase: A Theoretical Study. *Journal of the American Chemical Society*, 2000. **122**(33): p. 8031-8036.

15.   Chaudhuri, P., K. Wieghardt, T. Weyhermüller, T.K. Paine, S. Mukherjee, and C. Mukherjee, Biomimetic Metal-Radical Reactivity: Aerial Oxidation of Alcohols, Amines,

Aminophenols and Catechols Catalyzed by Transition Metal Complexes. *Biological Chemistry*, 2005. **386**(10): p. 1023-1033.

16.   Capone, M., A. Sirohiwal, M. Aschi, D.A. Pantazis, and I. Daidone, Alternative Fast and Slow Primary Charge-Separation Pathways in Photosystem II. *Angewandte Chemie*, 2023. **135**(16): p. e202216276.

17.   Yoneda, Y., E.A. Arsenault, S. Yang, Jr., K. Orcutt, M. Iwai, and G.R. Fleming, The Initial Charge Separation Step in Oxygenic Photosynthesis. *Nature Communications*, 2022. **13**(1): p. 2275.

18.   Saito, K., T. Ishida, M. Sugiura, K. Kawakami, Y. Umena, N. Kamiya, J.-R. Shen, and H. Ishikita, Distribution of the Cationic State Over the Chlorophyll Pair of the Photosystem II Reaction Center. *Journal of the American Chemical Society*, 2011. **133**(36): p. 14379-14388.

19.   Narzi, D., D. Bovi, P. De Gaetano, and L. Guidoni, Dynamics of the Special Pair of Chlorophylls of Photosystem II. *Journal of the American Chemical Society*, 2016. **138**(1): p. 257-264.

20.   Otsu, T. and A. Kuriyama, Living Mono- and Biradical Polymerizations in Homogeneous System Synthesis of AB and ABA Type Block Copolymers. *Polymer Bulletin*, 1984. **11**(2): p. 135-142.

21.   Hall Jr., H.K. and A.B. Padias, Organic and Polymer Chemistry of Electrophilic Tri- and Tetrasubstituted Ethylenes. *Journal of Polymer Science Part A: Polymer Chemistry*, 2004. **42**(12): p. 2845-2858.

22.   Twilton, J., C. Le, P. Zhang, M.H. Shaw, R.W. Evans, and D.W.C. MacMillan, The Merger of Transition Metal and Photocatalysis. *Nature Reviews Chemistry*, 2017. **1**(7): p. 0052.

23.   Huo, H., X. Shen, C. Wang, L. Zhang, P. Röse, L.-A. Chen, K. Harms, M. Marsch, G. Hilt, and E. Meggers, Asymmetric Photoredox Transition-Metal Catalysis Activated by Visible Light. *Nature*, 2014. **515**(7525): p. 100-103.

24.   Hopkinson, M.N., B. Sahoo, J.-L. Li, and F. Glorius, Dual Catalysis Sees the Light: Combining Photoredox with Organo-, Acid, and Transition-Metal Catalysis. *Chemistry – A European Journal*, 2014. **20**(14): p. 3874-3886.

25.   Bahnmüller, S., J. Plotzitzka, D. Baabe, B. Cordes, D. Menzel, K. Schartz, P. Schweyen, R. Wicht, and M. Bröring, Hexaethyltripyrrindione (H3Et6tpd): A Non-Innocent Ligand Forming Stable Radical Complexes with Divalent Transition-Metal Ions. *European Journal of Inorganic Chemistry*, 2016. **2016**(29): p. 4761-4768.

26.   Gautam, R., A.V. Astashkin, T.M. Chang, J. Shearer, and E. Tomat, Interactions of Metal-Based and Ligand-Based Electronic Spins in Neutral Tripyrrindione π Dimers. *Inorganic Chemistry*, 2017. **56**(11): p. 6755-6762.

27.   Tomat, E., Coordination Chemistry of Linear Tripyrroles: Promises and Perils. *Comments on Inorganic Chemistry*, 2016. **36**(6): p. 327-342.

28.   Chirik, P.J. and K. Wieghardt, Radical Ligands Confer Nobility on Base-Metal Catalysts. *Science*, 2010. **327**(5967): p. 794-795.

29.   Gomberg, M., An Instance of Trivalent Carbon: Triphenylmethyl. *Journal of the American Chemical Society*, 1900. **22**(11): p. 757-771.

30.   Hicks, R., Stable Radicals: Fundamentals and Applied Aspects of Odd-Electron Compounds. 2011: *Wiley*.

31.   Abe, M., Diradicals. *Chemical Reviews*, 2013. **113**(9): p. 7011-7088.

32.   Zhang, N., S.R. Samanta, B.M. Rosen, and V. Percec, Single Electron Transfer in Radical Ion and Radical-Mediated Organic, Materials and Polymer Synthesis. *Chemical Reviews*, 2014. **114**(11): p. 5848-5958.

33.   Nishide, H. and T. Suga, Organic Radical Battery. *The Electrochemical Society Interface*, 2005. **14**(4): p. 32.

34.   Morita, Y., S. Nishida, T. Murata, M. Moriguchi, A. Ueda, M. Satoh, K. Arifuku, K. Sato, and T. Takui, Organic Tailored Batteries Materials Using Stable Open-Shell Molecules with Degenerate Frontier Orbitals. *Nature Materials*, 2011. **10**(12): p. 947-951.

35.   Kamada, K., K. Ohta, T. Kubo, A. Shimizu, Y. Morita, K. Nakasuji, R. Kishi, S. Ohta, S.-i. Furukawa, H. Takahashi, and M. Nakano, Strong Two-Photon Absorption of Singlet Diradical Hydrocarbons. *Angewandte Chemie (International ed. in English)*, 2007. **46**(19): p. 3544-3546.

36.   Kamada, K., S.-i. Fuku-en, S. Minamide, K. Ohta, R. Kishi, M. Nakano, H. Matsuzaki, H. Okamoto, H. Higashikawa, K. Inoue, S. Kojima, and Y. Yamamoto, Impact of Diradical Character on Two-Photon Absorption: Bis(acridine) Dimers Synthesized from an Allenic Precursor. *Journal of the American Chemical Society*, 2013. **135**(1): p. 232-241.

37.   Kobayashi, Y., K. Mutoh, and J. Abe, Fast Photochromic Molecules Toward Realization of Photosynergetic Effects. *The Journal of Physical Chemistry Letters*, 2016. **7**(18): p. 3666-3675.

38.   Novaes, L.F.T., J. Liu, Y. Shen, L. Lu, J.M. Meinhardt, and S. Lin, Electrocatalysis as An Enabling Technology for Organic Synthesis. *Chemical Society Reviews*, 2021. **50**(14): p. 7941-8002.

39.   Tay, N.E.S., D. Lehnherr, and T. Rovis, Photons or Electrons? A Critical Comparison of Electrochemistry and Photoredox Catalysis for Organic Synthesis. *Chemical Reviews*, 2022. **122**(2): p. 2487-2649.

40.   Glaser, F., C. Kerzig, and O.S. Wenger, Multi-Photon Excitation in Photoredox Catalysis: Concepts, Applications, Methods. *Angewandte Chemie International Edition*, 2020. **59**(26): p. 10266-10284.

41.   Liao, L.-L., L. Song, S.-S. Yan, J.-H. Ye, and D.-G. Yu, Highly Reductive Photocatalytic Systems in Organic Synthesis. *Trends in Chemistry*, 2022. **4**(6): p. 512-527.

42.   Mei, L., J.M. Veleta, and T.L. Gianetti, Helical Carbenium Ion: A Versatile Organic Photoredox Catalyst for Red-Light-Mediated Reactions. *Journal of the American Chemical Society*, 2020. **142**(28): p. 12056-12061.

43.   Hossain, M.M., A.C. Shaikh, R. Kaur, and T.L. Gianetti, Red Light–Blue Light Chromoselective C(sp2)–X Bond Activation by Organic Helicenium-Based Photocatalysis. *Journal of the American Chemical Society*, 2024. **146**(12): p. 7922-7930.

44.   Moerner, W.E. and D.P. Fromm, Methods of Single-Molecule Fluorescence Spectroscopy and Microscopy. *Review of Scientific Instruments*, 2003. **74**(8): p. 3597-3619.

45.   Förster, T., Zwischenmolekulare Energiewanderung und Fluoreszenz. *Annalen der Physik*, 1948. **437**(1-2): p. 55-75.

46.   Kasha, M., Characterization of Electronic Transitions in Complex Molecules. *Discussions of the Faraday society*, 1950. **9**: p. 14-19.

47.   Swain, A., Steady-State and Ultrafast Optical Properties of Tripyrrindione Ligand and Metal Complexes. 2022, *The University of Arizona*.

48.   O'Connor, D., Time-Correlated Single Photon Counting. 2012: *Academic press*.

49.   Berezin, M.Y. and S. Achilefu, Fluorescence Lifetime Measurements and Biological Imaging. *Chemical reviews*, 2010. **110**(5): p. 2641-2684.

50.   Swain, A., B. Cho, R. Gautam, C.J. Curtis, E. Tomat, and V. Huxter, Ultrafast Dynamics of Tripyrrindiones in Solution Mediated by Hydrogen-Bonding Interactions. *The Journal of Physical Chemistry B*, 2019. **123**(26): p. 5524-5535.

51.   van Stokkum, I.H.M., D.S. Larsen, and R. van Grondelle, Global and Target Analysis of Time-Resolved Spectra. *Biochimica et Biophysica Acta (BBA) - Bioenergetics*, 2004. **1657**(2): p. 82-104.

52.   Fuller, F.D. and J.P. Ogilvie, Experimental Implementations of Two-Dimensional Fourier Transform Electronic Spectroscopy. *Annual Review of Physical Chemistry*, 2015. **66**(Volume 66, 2015): p. 667-690.

53.   Hybl, J.D., A.W. Albrecht, S.M. Gallagher Faeder, and D.M. Jonas, Two-Dimensional Electronic Spectroscopy. *Chemical Physics Letters*, 1998. **297**(3): p. 307-313.

54.   Hybl, J.D., A. Albrecht Ferro, and D.M. Jonas, Two-Dimensional Fourier Transform Electronic Spectroscopy. *The Journal of Chemical Physics*, 2001. **115**(14): p. 6606-6622.

55.   Brixner, T., T. Mančal, I.V. Stiopkin, and G.R. Fleming, Phase-Stabilized Two-Dimensional Electronic Spectroscopy. *The Journal of Chemical Physics*, 2004. **121**(9): p. 4221-4236.

56.   Brixner, T., I.V. Stiopkin, and G.R. Fleming, Tunable Two-Dimensional Femtosecond Spectroscopy. *Optics Letters*, 2004. **29**(8): p. 884-886.

57.   Cowan, M., J. Ogilvie, and R. Miller, Two-Dimensional Spectroscopy Using Diffractive Optics Based Phased-Locked Photon Echoes. *Chemical Physics Letters*, 2004. **386**(1-3): p. 184-189.

58.   DeFlores, L.P., R.A. Nicodemus, and A. Tokmakoff, Two-Dimensional Fourier Transform Spectroscopy in the Pump-Probe Geometry. *Optics letters*, 2007. **32**(20): p. 2966-2968.

59.   Gundogdu, K., K.W. Stone, D.B. Turner, and K.A. Nelson, Multidimensional Coherent Spectroscopy Made Easy. *Chemical Physics*, 2007. **341**(1-3): p. 89-94.

60.   Tekavec, P.F., G.A. Lott, and A.H. Marcus, Fluorescence-Detected Two-Dimensional Electronic Coherence Spectroscopy by Acousto-Optic Phase Modulation. *The Journal of Chemical Physics*, 2007. **127**(21).

61.   Vaughan, J.C., T. Hornung, K. Stone, and K.A. Nelson, Coherently Controlled Ultrafast Four-Wave Mixing Spectroscopy. *The Journal of Physical Chemistry A*, 2007. **111**(23): p. 4873-4883.

62.   Myers, J.A., K.L.M. Lewis, P.F. Tekavec, and J.P. Ogilvie, Two-Color Two-Dimensional Fourier Transform Electronic Spectroscopy with a Pulse-Shaper. *Optics Express*, 2008. **16**(22): p. 17420-17428.

63.   Tekavec, P.F., J.A. Myers, K.L. Lewis, and J.P. Ogilvie, Two-Dimensional Electronic Spectroscopy with a Continuum Probe. *Optics letters*, 2009. **34**(9): p. 1390-1392.

64.   Harel, E., A.F. Fidler, and G.S. Engel, Real-Time Mapping of Electronic Structure with Single-Shot Two-Dimensional Electronic Spectroscopy. *Proceedings of the National Academy of Sciences*, 2010. **107**(38): p. 16444-16447.

65.   Brida, D., C. Manzoni, and G. Cerullo, Phase-Locked Pulses for Two-Dimensional Spectroscopy by a Birefringent Delay Line. *Optics letters*, 2012. **37**(15): p. 3027-3029.

66.   Zhang, Y., K. Meyer, C. Ott, and T. Pfeifer, Passively Phase-Stable, Monolithic, All-Reflective Two-Dimensional Electronic Spectroscopy Based on a Four-Quadrant Mirror. *Optics Letters*, 2013. **38**(3): p. 356-358.

67.   Heisler, I.A., R. Moca, F.V.A. Camargo, and S.R. Meech, Two-Dimensional Electronic Spectroscopy Based on Conventional Optics and Fast Dual Chopper Data Acquisition. *Review of Scientific Instruments*, 2014. **85**(6).

68.   Ernst, R.R., G. Bodenhausen, and A. Wokaun, Principles of Nuclear Magnetic Resonance in One and Two Dimensions. 1990: *Oxford university press*.

69.   Tan, H.-S., Theory and Phase-Cycling Scheme Selection Principles of Collinear Phase Coherent Multi-Dimensional Optical Spectroscopy. *The Journal of Chemical Physics*, 2008. **129**(12).

70.   Zhang, Z., K.L. Wells, E.W.J. Hyland, and H.-S. Tan, Phase-Cycling Schemes for Pump–Probe Beam Geometry Two-Dimensional Electronic Spectroscopy. *Chemical Physics Letters*, 2012. **550**: p. 156-161.

71.   Cho, B., A. Swain, R. Gautam, E. Tomat, and V.M. Huxter, Time-Resolved Dynamics of Stable Open- and Closed-Shell Neutral Radical and Oxidized Tripyrrindione Complexes. *Phys Chem Chem Phys*, 2022. **24**(26): p. 15718-15725.

72.   Preuss, K.E., Pancake Bonds: π-Stacked Dimers of Organic and Light-Atom Radicals. *Polyhedron*, 2014. **79**: p. 1-15.

73.   Kertesz, M., Pancake Bonding: An Unusual Pi-Stacking Interaction. *Chemistry – A European Journal*, 2019. **25**(2): p. 400-416.

74.   Tomat, E., C.J. Curtis, A.V. Astashkin, J. Conradie, and A. Ghosh, Multicenter Interactions and Ligand Field Effects in Platinum(II) Tripyrrindione Radicals. *Dalton Transactions*, 2023. **52**(19): p. 6559-6568.

75.   Habenšus, I., A. Ghavam, C.J. Curtis, A.V. Astashkin, and E. Tomat, Primary Amines as Ligands and Linkers in Complexes of Tripyrrindione Radicals. *Journal of Porphyrins and Phthalocyanines*, 2023. **27**(07n10): p. 1448-1456.

76.   Englman, R. and J. Jortner, The Energy Gap Law for Radiationless Transitions in Large Molecules. *Molecular Physics*, 1970. **18**(2): p. 145-164.

77.   Gouterman, M., Optical Spectra and Electronic Structure of Porphyrins and Related Rings. *The porphyrins*, 1978. **3**.

78.   Straub, K.D., P.M. Rentzepis, and D. Huppert, Picosecond Spectroscopy of Some Metalloporphyrins. *Journal of Photochemistry*, 1981. **17**(2): p. 419-425.

79.   Biswas, S., J. Kim, X. Zhang, and G.D. Scholes, Coherent Two-Dimensional and Broadband Electronic Spectroscopies. *Chemical Reviews*, 2022. **122**(3): p. 4257-4321.

80.   Van Amerongen, H. and R. Van Grondelle, Photosynthetic Excitons. 2000: *World Scientific*.

81.   Silinsh, E.A. and V. Cápek. Organic Molecular Crystals : Interaction, Localization, and Transport Phenomena. 1994.

82.   Gautam, R., J.J. Loughrey, A.V. Astashkin, J. Shearer, and E. Tomat, Tripyrrindione as a Redox-Active Ligand: Palladium(II) Coordination in Three Redox States. *Angewandte Chemie International Edition*, 2015. **54**(49): p. 14894-14897.

83.   Védrine, J.C., Metal Oxides in Heterogeneous Oxidation Catalysis: State of the Art and Challenges for a More Sustainable World. *ChemSusChem*, 2019. **12**(3): p. 577-588.

84.   Thomas, J.M. and W.J. Thomas, Principles and Practice of Heterogeneous Catalysis. 2014: *John Wiley & Sons*.

85.   Romero, N.A. and D.A. Nicewicz, Organic Photoredox Catalysis. *Chemical Reviews*, 2016. **116**(17): p. 10075-10166.

86.   Jiang, W., B.Q.L. Low, R. Long, J. Low, H. Loh, K.Y. Tang, C.H.T. Chai, H. Zhu, H. Zhu, Z. Li, X.J. Loh, Y. Xiong, and E. Ye, Active Site Engineering on Plasmonic Nanostructures for Efficient Photocatalysis. *ACS Nano*, 2023. **17**(5): p. 4193-4229.

87.   Liu, J., L. Ye, S. Wooh, M. Kappl, W. Steffen, and H.-J. Butt, Optimizing Hydrophobicity and Photocatalytic Activity of PDMS-Coated Titanium Dioxide. *ACS Applied Materials & Interfaces*, 2019. **11**(30): p. 27422-27425.

88.   Goddard, J.-P., C. Ollivier, and L. Fensterbank, Photoredox Catalysis for the Generation of Carbon Centered Radicals. *Accounts of Chemical Research*, 2016. **49**(9): p. 1924-1936.

89.   Prier, C.K., D.A. Rankic, and D.W.C. MacMillan, Visible Light Photoredox Catalysis with Transition Metal Complexes: Applications in Organic Synthesis. *Chemical Reviews*, 2013. **113**(7): p. 5322-5363.

90.   Hopkinson, M.N., A. Tlahuext-Aca, and F. Glorius, Merging Visible Light Photoredox and Gold Catalysis. *Accounts of Chemical Research*, 2016. **49**(10): p. 2261-2272.

91.   Lang, X., J. Zhao, and X. Chen, Cooperative Photoredox Catalysis. *Chemical Society Reviews*, 2016. **45**(11): p. 3026-3038.

92. Shaw, M.H., J. Twilton, and D.W.C. MacMillan, Photoredox Catalysis in Organic Chemistry. *The Journal of Organic Chemistry*, 2016. **81**(16): p. 6898-6926.

93. Wang, C.-S., P.H. Dixneuf, and J.-F. Soulé, Photoredox Catalysis for Building C–C Bonds from C(sp2)–H Bonds. *Chemical Reviews*, 2018. **118**(16): p. 7532-7585.

94. Anastas, P.T. and M.M. Kirchhoff, Origins, Current Status, and Future Challenges of Green Chemistry. *Accounts of Chemical Research*, 2002. **35**(9): p. 686-694.

95. Liu, J., T. Dietz, S.R. Carpenter, M. Alberti, C. Folke, E. Moran, A.N. Pell, P. Deadman, T. Kratz, J. Lubchenco, E. Ostrom, Z. Ouyang, W. Provencher, C.L. Redman, S.H. Schneider, and W.W. Taylor, Complexity of Coupled Human and Natural Systems. *Science*, 2007. **317**(5844): p. 1513-1516.

96. Clarke, C.J., W.-C. Tu, O. Levers, A. Bröhl, and J.P. Hallett, Green and Sustainable Solvents in Chemical Processes. *Chemical Reviews*, 2018. **118**(2): p. 747-800.

97. Liu, J., H. Mooney, V. Hull, S.J. Davis, J. Gaskell, T. Hertel, J. Lubchenco, K.C. Seto, P. Gleick, C. Kremen, and S. Li, Systems Integration for Global Sustainability. *Science*, 2015. **347**(6225): p. 1258832.

98. Ravelli, D., M. Fagnoni, and A. Albini, Photoorganocatalysis. What for? *Chemical Society Reviews*, 2013. **42**(1): p. 97-113.

99. Skubi, K.L., T.R. Blum, and T.P. Yoon, Dual Catalysis Strategies in Photochemical Synthesis. *Chemical Reviews*, 2016. **116**(17): p. 10035-10074.

100.   Marzo, L., S.K. Pagire, O. Reiser, and B. König, Visible-Light Photocatalysis: Does It Make a Difference in Organic Synthesis? *Angewandte Chemie International Edition*, 2018. **57**(32): p. 10034-10072.

101.   Xuan, J., Z.-J. Feng, S.-W. Duan, and W.-J. Xiao, Room Temperature Synthesis of Isoquino[2,1-a][3,1]oxazine and Isoquino[2,1-a]pyrimidine Derivatives via Visible Light Photoredox Catalysis. *RSC Advances*, 2012. **2**(10): p. 4065-4068.

102.   Nicewicz, D.A. and T.M. Nguyen, Recent Applications of Organic Dyes as Photoredox Catalysts in Organic Synthesis. *ACS Catalysis*, 2014. **4**(1): p. 355-360.

103.   Phelan, J.P., S.B. Lang, J.S. Compton, C.B. Kelly, R. Dykstra, O. Gutierrez, and G.A. Molander, Redox-Neutral Photocatalytic Cyclopropanation via Radical/Polar Crossover. *Journal of the American Chemical Society*, 2018. **140**(25): p. 8037-8047.

104.   Shang, T.-Y., L.-H. Lu, Z. Cao, Y. Liu, W.-M. He, and B. Yu, Recent Advances of 1,2,3,5-Tetrakis(carbazol-9-yl)-4,6-dicyanobenzene (4CzIPN) in Photocatalytic Transformations. *Chemical Communications*, 2019. **55**(38): p. 5408-5419.

105.   Hari, D.P. and B. König, Eosin Y Catalyzed Visible Light Oxidative C–C and C–P bond Formation. *Organic Letters*, 2011. **13**(15): p. 3852-3855.

106.   Cantillo, D., O. de Frutos, J.A. Rincón, C. Mateos, and C.O. Kappe, Continuous Flow α-Trifluoromethylation of Ketones by Metal-Free Visible Light Photoredox Catalysis. *Organic Letters*, 2014. **16**(3): p. 896-899.

107.   Juris, A., V. Balzani, P. Belser, and A. von Zelewsky, Characterization of the Excited State Properties of Some New Photosensitizers of the Ruthenium (Polypyridine) Family. *Helvetica Chimica Acta*, 1981. **64**(7): p. 2175-2182.

108.   Kalyanasundaram, K., Photophysics, Photochemistry and Solar Energy Conversion with Tris(bipyridyl) Ruthenium(II) and Its Analogues. *Coordination Chemistry Reviews*, 1982. **46**: p. 159-244.

109.   Bolm, C. and M. Beller, Transition Metals for Organic Synthesis. Vol. 1. 2004: *Wiley-VCH, Weinheim*.

110.   Lowry, M.S., J.I. Goldsmith, J.D. Slinker, R. Rohl, R.A. Pascal, G.G. Malliaras, and S. Bernhard, Single-Layer Electroluminescent Devices and Photoinduced Hydrogen Production from an Ionic Iridium(III) Complex. *Chemistry of Materials*, 2005. **17**(23): p. 5712-5719.

111.   Schultz, D.M. and T.P. Yoon, Solar Synthesis: Prospects in Visible Light Photocatalysis. *Science*, 2014. **343**(6174): p. 1239176.

112.   Kelly, C.B., N.R. Patel, D.N. Primer, M. Jouffroy, J.C. Tellis, and G.A. Molander, Preparation of Visible-Light-Activated Metal Complexes and Their Use in Photoredox/Nickel Dual Catalysis. *Nature Protocols*, 2017. **12**(3): p. 472-492.

113.   Parasram, M. and V. Gevorgyan, Visible Light-Induced Transition Metal-Catalyzed Transformations: Beyond Conventional Photosensitizers. *Chemical Society Reviews*, 2017. **46**(20): p. 6227-6240.

114.   Cocquet, G., C. Ferroud, and A. Guy, A Mild and Efficient Procedure for Ring-Opening Reactions of Piperidine and Pyrrolidine Derivatives by Single Electron Transfer Photooxidation. *Tetrahedron*, 2000. **56**(19): p. 2975-2984.

115.   Cocquet, G., C. Ferroud, P. Simon, and P.-L. Taberna, Single Electron Transfer Photoinduced Oxidation of Piperidine and Pyrrolidine Derivatives to the Corresponding Lactams. *Journal of the Chemical Society, Perkin Transactions 2*, 2000(6): p. 1147-1153.

116.   Lee, J., J.W. Papatzimas, A.D. Bromby, E. Gorobets, and D.J. Derksen, Thiaporphyrin-Mediated Photocatalysis Using Red Light. *RSC Advances*, 2016. **6**(64): p. 59269-59272.

117.   Matsuzaki, K., T. Hiromura, E. Tokunaga, and N. Shibata, Trifluoroethoxy-Coated Subphthalocyanine affects Trifluoromethylation of Alkenes and Alkynes even under Low-Energy Red-Light Irradiation. *ChemistryOpen*, 2017. **6**(2): p. 226-230.

118.   Ravetz, B.D., A.B. Pun, E.M. Churchill, D.N. Congreve, T. Rovis, and L.M. Campos, Photoredox Catalysis Using Infrared Light via Triplet Fusion Upconversion. *Nature*, 2019. **565**(7739): p. 343-346.

119.   Yerien, D.E., M.V. Cooke, M.C. García Vior, S. Barata-Vallejo, and A. Postigo, Radical Fluoroalkylation Reactions of (Hetero)arenes and Sulfides Under Red Light Photocatalysis. *Organic & Biomolecular Chemistry*, 2019. **17**(15): p. 3741-3746.

120.   Fülöp, A., X. Peng, M.M. Greenberg, and A. Mokhir, A Nucleic Acid-Directed, Red Light-Induced Chemical Reaction. *Chemical Communications*, 2010. **46**(31): p. 5659-5661.

121.   Carling, C.-J., J. Olejniczak, A. Foucault-Collet, G. Collet, M.L. Viger, V.A. Nguyen
        Huu, B.M. Duggan, and A. Almutairi, *Efficient Red Light Photo-Uncaging of Active
        Molecules in Water upon Assembly into Nanoparticles. Chemical Science*, 2016. **7**(3): p.
        2392-2398.

122.   Zhang, H., W.S. Trout, S. Liu, G.A. Andrade, D.A. Hudson, S.L. Scinto, K.T. Dicker, Y.
        Li, N. Lazouski, J. Rosenthal, C. Thorpe, X. Jia, and J.M. Fox, *Rapid Bioorthogonal
        Chemistry Turn-on through Enzymatic or Long Wavelength Photocatalytic Activation of
        Tetrazine Ligation. Journal of the American Chemical Society*, 2016. **138**(18): p. 5978-
        5983.

123.   Schmidt, K., S. Brovelli, V. Coropceanu, D. Beljonne, J. Cornil, C. Bazzini, T. Caronna,
        R. Tubino, F. Meinardi, Z. Shuai, and J.-L. Brédas, *Intersystem Crossing Processes in
        Nonplanar Aromatic Heterocyclic Molecules. The Journal of Physical Chemistry A*,
        2007. **111**(42): p. 10490-10499.

124.   Sapir, M. and E.V. Donckt, *Intersystem Crossing in the Helicenes. Chemical Physics
        Letters*, 1975. **36**(1): p. 108-110.

125.   Nijegorodov, N.I. and W.S. Downey, *The Influence of Planarity and Rigidity on the
        Absorption and Fluorescence Parameters and Intersystem Crossing Rate Constant in
        Aromatic Molecules. The Journal of Physical Chemistry*, 1994. **98**(22): p. 5639-5643.

126.   Beljonne, D., Z. Shuai, G. Pourtois, and J.L. Bredas, Spin−Orbit Coupling and Intersystem Crossing in Conjugated Polymers: A Configuration Interaction Description. *The Journal of Physical Chemistry A*, 2001. **105**(15): p. 3899-3907.

127.   Laursen, B.W. and F.C. Krebs, Synthesis of a Triazatriangulenium Salt. *Angewandte Chemie International Edition*, 2000. **39**(19): p. 3432-3434.

128.   Dean, J.C., D.G. Oblinsky, S.R. Rather, and G.D. Scholes, Methylene Blue Exciton States Steer Nonradiative Relaxation: Ultrafast Spectroscopy of Methylene Blue Dimer. *The Journal of Physical Chemistry B*, 2016. **120**(3): p. 440-454.

129.   Birks, J.B., D.J.S. Birch, E. Cordemans, and E. Vander Donckt, Fluorescence of the Higher Helicenes. *Chemical Physics Letters*, 1976. **43**(1): p. 33-36.

130.   Graule, S., M. Rudolph, W. Shen, J.A.G. Williams, C. Lescop, J. Autschbach, J. Crassous, and R. Réau, Assembly of π-Conjugated Phosphole Azahelicene Derivatives into Chiral Coordination Complexes: An Experimental and Theoretical Study. *Chemistry − A European Journal*, 2010. **16**(20): p. 5976-6005.

131.   Anger, E., M. Rudolph, L. Norel, S. Zrig, C. Shen, N. Vanthuyne, L. Toupet, J.A.G. Williams, C. Roussel, J. Autschbach, J. Crassous, and R. Réau, Multifunctional and Reactive Enantiopure Organometallic Helicenes: Tuning Chiroptical Properties by Structural Variations of Mono- and Bis(platinahelicene)s. *Chemistry − A European Journal*, 2011. **17**(50): p. 14178-14198.

132.   Koli, M., S. Gupta, S. Chakraborty, A. Ghosh, R. Ghosh, A.P. Wadawale, T.K. Ghanty, B.S. Patro, and S. Mula, Design and Synthesis of BODIPY-Hetero[5]helicenes as Heavy-Atom-Free Triplet Photosensitizers for Photodynamic Therapy of Cancer. *Chemistry – A European Journal*, 2023. **29**(57): p. e202301605.

133.   Liu, Y., D. Aranda, and F. Santoro, A Computational Study of the Vibronic Effects on the Electronic Spectra and the Photophysics of Aza[7]helicene. *Physical Chemistry Chemical Physics*, 2021. **23**(31): p. 16551-16563.

134.   Müller, C., T. Pascher, A. Eriksson, P. Chabera, and J. Uhlig, KiMoPack: A python Package for Kinetic Modeling of the Chemical Mechanism. *The Journal of Physical Chemistry A*, 2022. **126**(25): p. 4087-4099.

135.   Chen, J., T.C. Cesario, and P.M. Rentzepis, Time-Resolved Spectroscopic Studies of Methylene Blue and Phenothiazine Derivatives Used for Bacteria Inactivation. *Chemical Physics Letters*, 2010. **498**(1): p. 81-85.

136.   Reichardt, C., R.A. Vogt, and C.E. Crespo-Hernández, On the Origin of Ultrafast Nonradiative Transitions in Nitro-Polycyclic Aromatic Hydrocarbons: Excited-State Dynamics in 1-Nitronaphthalene. *The Journal of Chemical Physics*, 2009. **131**(22).

137.   Romanov, A.N., S.K. Gularyan, B.M. Polyak, R.A. Sakovich, G.E. Dobretsov, and O.M. Sarkisov, Electronically Excited States of Membrane Fluorescent Probe 4-Dimethylaminochalcone: Results of Quantum Chemical Calculations. *Physical Chemistry Chemical Physics*, 2011. **13**(20): p. 9518-9524.

138.   Carlotti, B., F. Elisei, U. Mazzucato, and A. Spalletti, Unusual High Fluorescence of Two Nitro-Distyrylbenzene-like Compounds Induced by CT Processes Affecting the Fluorescence/Intersystem-Crossing Competition. *Physical Chemistry Chemical Physics*, 2015. **17**(22): p. 14740-14749.

139.   Ghosh, R., A. Nandi, and D.K. Palit, Solvent Sensitive Intramolecular Charge Transfer Dynamics in the Excited States of 4-N,N-Dimethylamino-4′-Nitrobiphenyl. *Physical Chemistry Chemical Physics*, 2016. **18**(11): p. 7661-7671.

140.   Yang, W., J. Zhao, C. Sonn, D. Escudero, A. Karatay, H.G. Yaglioglu, B. Küçüköz, M. Hayvali, C. Li, and D. Jacquemin, Efficient Intersystem Crossing in Heavy-Atom-Free Perylenebisimide Derivatives. *The Journal of Physical Chemistry C*, 2016. **120**(19): p. 10162-10175.

141.   Lewis, F.D., R.T. Lauterbach, H.G. Heine, W. Hartmann, and H. Rudolph, Photochemical Alpha Cleavage of Benzoin Derivatives: Polar Transition States for Free-Radical Formation. *Journal of the American Chemical Society*, 1975. **97**(6): p. 1519-1525.

142.   Gularyan, S.K., O.M. Sarkisov, G.E. Dobretsov, V.Y. Svetlichnyi, F.E. Gostev, and S.A. Antipin, 4-Dimethylaminochalcone as Fluorescent Probe: Effect of the Medium Polarity on Relaxation Processes in the Excited State. *Russian Chemical Bulletin*, 2004. **53**(8): p. 1670-1673.

143. Nagarajan, K., A.R. Mallia, K. Muraleedharan, and M. Hariharan, Enhanced Intersystem Crossing in Core-Twisted Aromatics. *Chemical Science*, 2017. **8**(3): p. 1776-1782.

144. Stephansen, A.B. and T.I. Sølling, Distortion Dependent Intersystem Crossing: A Femtosecond Time-Resolved Photoelectron Spectroscopy Study of Benzene, Toluene, and p-Xylene. *Structural Dynamics*, 2017. **4**(4).

145. Rehm, D. and A. Weller, Kinetics of Fluorescence Quenching by Electron and H-Atom Transfer. *Israel Journal of Chemistry*, 1970. **8**(2): p. 259-271.

146. Lakowicz, J.R., Quenching of Fluorescence, in *Principles of Fluorescence Spectroscopy*, J.R. Lakowicz, Editor. 1983, *Springer US*: Boston, MA. p. 257-301.

147. Sandanayaka, A.S.D., Y. Araki, C. Luo, M. Fujitsuka, and O. Ito, Photoinduced Electron-Transfer Processes of Fullerene (C60) with Amine Donors: Excited Triplet Route vs Excited Singlet Route. *Bulletin of the Chemical Society of Japan*, 2004. **77**(7): p. 1313-1322.

148. Peters, K.S., S.C. Freilich, and C.G. Schaeffer, Dynamics of Electron Transfer in Amine Photooxidation. *Journal of the American Chemical Society*, 1980. **102**(17): p. 5701-5702.

149. Devadoss, C. and R.W. Fessenden, Picosecond and Nanosecond Studies of the Photoreduction of Benzophenone by 1,4-Diazabicyclo[2.2.2]Octane: Characterization of the Transient. *The Journal of Physical Chemistry*, 1990. **94**(11): p. 4540-4549.

150. Demeter, A., L. Biczok, T. Berces, V. Wintgens, P. Valat, and J. Kossanyi, Laser Photolysis Studies of Transient Processes in the Photoreduction of Naphthalimides by Aliphatic Amines. *The Journal of Physical Chemistry*, 1993. **97**(13): p. 3217-3224.

151. Görner, H., Electron Transfer from Triethylamine to the Triplet State of Dinitronaphthalenes, 4,4'-Dinitrobiphenyl and 2,7-Dinitrofluorenone: Time Resolved UV−Vis Spectroscopic and Conductometric Study in Polar Solvents. *The Journal of Physical Chemistry A*, 2002. **106**(25): p. 5989-5998.

152. Hoffmann, N. and H. Görner, Photoinduced Electron Transfer from N-Methylpyrrolidine to Ketones and Radical Addition to an Electron-Deficient Alkene. *Chemical Physics Letters*, 2004. **383**(5): p. 451-455.

153. Chen, P.-Z., L.-Y. Niu, Y.-Z. Chen, and Q.-Z. Yang, Difluoroboron β-diketonate Dyes: Spectroscopic Properties and Applications. *Coordination Chemistry Reviews*, 2017. **350**: p. 196-216.

154. Dougherty, D.A., Spin Control in Organic Molecules. *Accounts of Chemical Research*, 1991. **24**(3): p. 88-94.

155. Borden, W.T., H. Iwamura, and J.A. Berson, Violations of Hund's Rule in Non-Kekule Hydrocarbons: Theoretical Prediction and Experimental Verification. *Accounts of chemical research*, 1994. **27**(4): p. 109-116.

156. Zeng, Z., X. Shi, C. Chi, J.T.L. Navarrete, J. Casado, and J. Wu, Pro-Aromatic and Anti-Aromatic π-Conjugated Molecules: An Irresistible Wish to be Diradicals. *Chemical Society Reviews*, 2015. **44**(18): p. 6578-6596.

157. Tokumura, K., N. Mizukami, M. Udagawa, and M. Itoh, Doublet-Doublet Fluorescence and Coupling Reactions of 9-Anthrylmethyl Radical in Fluid Hexane Solution Studied by Two-Step Laser Excitation Fluorescence Spectroscopy. *The Journal of Physical Chemistry*, 1986. **90**(17): p. 3873-3876.

158. Scaiano, J.C., L.J. Johnston, W.G. McGimpsey, and D. Weir, Photochemistry of Organic Reaction Intermediates: Novel Reaction Paths Induced by Two-Photon Laser Excitation. *Accounts of Chemical Research*, 1988. **21**(1): p. 22-29.

159. Samanta, A., K. Bhattacharyya, P. Das, P.V. Kamat, D. Weir, and G. Hug, Quenching of Excited Doublet States of Organic Radicals by Stable Radicals. *The Journal of Physical Chemistry*, 1989. **93**(9): p. 3651-3656.

160. Tokumura, K., T. Ozaki, M. Udagawa, and M. Ito, Lifetime and Electronic Spectra of p-Methoxybenzyl Radical in the Lowest Excited Doublet State in Solution. *The Journal of Physical Chemistry*, 1989. **93**(1): p. 161-164.

161. Eggins, B.R. and P.K.J. Robertson, Photoelectrochemistry Using Quinone Radical Anions. *Journal of the Chemical Society, Faraday Transactions*, 1994. **90**(15): p. 2249-2256.

162. Majima, T., M. Fukui, A. Ishida, and S. Takamuku, Stilbene Radical Anions in the Excited Doublet State. *The Journal of Physical Chemistry*, 1996. **100**(21): p. 8913-8919.

163. Breslin, D.T. and M.A. Fox, Excited-State Behavior of Thermally Stable Radical Ions. *The Journal of Physical Chemistry*, 1994. **98**(2): p. 408-411.

164. Ishida, A., M. Fukui, H. Ogawa, S. Tojo, T. Majima, and S. Takamuku, Lifetimes and Transient Phenomena of Stilbene Radical Cations in the Second Excited Doublet State. *Journal of physical chemistry (1952)*, 1995. **99**(27): p. 10808-10814.

165. Cook, A.R., L.A. Curtiss, and J.R. Miller, Fluorescence of the 1, 4-benzoquinone Radical Anion. *Journal of the American Chemical Society*, 1997. **119**(24): p. 5729-5734.

166. Fujisawa, J.-i., K. Ishii, Y. Ohba, S. Yamauchi, M. Fuhs, and K. Möbius, First Observation of the Excited Doublet State of a Radical− Triplet Pair in Solution: W-Band High-Field Time-Resolved Electron Paramagnetic Resonance Spectroscopy. *The Journal of Physical Chemistry A*, 1999. **103**(2): p. 213-216.

167. Ishii, K., Y. Hirose, and N. Kobayashi, Electron Spin Polarizations of Phthalocyaninatosilicon Covalently Linked to One TEMPO Radical in the Excited Quartet and Doublet Ground States. *The Journal of Physical Chemistry A*, 1999. **103**(13): p. 1986-1990.

168. Rawson, J.M., A. Alberola, and A. Whalley, Thiazyl Radicals: Old Materials for New Molecular Devices. *Journal of Materials Chemistry*, 2006. **16**(26): p. 2560-2575.

169.   Kamada, K., K. Ohta, T. Kubo, A. Shimizu, Y. Morita, K. Nakasuji, R. Kishi, S. Ohta, S.-i. Furukawa, and H. Takahashi, *Strong Two-photon Absorption of Singlet Diradical Hydrocarbons. Angewandte Chemie (International ed. in English)*, 2007. **46**(19): p. 3544-3546.

170.   Iwasaki, A., L. Hu, R. Suizu, K. Nomura, H. Yoshikawa, K. Awaga, Y. Noda, K. Kanai, Y. Ouchi, and K. Seki, *Interactive Radical Dimers in Photoconductive Organic Thin Films. Angewandte Chemie International Edition*, 2009. **48**(22): p. 4022-4024.

171.   Morita, Y., S. Suzuki, K. Sato, and T. Takui, *Synthetic Organic Spin Chemistry for Structurally well-defined Open-Shell Graphene Fragments. Nature chemistry*, 2011. **3**(3): p. 197-204.

172.   Janoschka, T., M.D. Hager, and U.S. Schubert, *Powering Up the Future: Radical Polymers for Battery Applications. Advanced Materials*, 2012. **24**(48): p. 6397-6409.

173.   Nakano, M. and B. Champagne, *Theoretical Design of Open-Shell Singlet Molecular Systems for Nonlinear Optics. The Journal of Physical Chemistry Letters*, 2015. **6**(16): p. 3236-3256.

174.   Bohme, D.K., *PAH [Polycyclic Aromatic Hydrocarbons] and Fullerene Ions and Ion/Molecule Reactions in Interstellar and Circumstellar Chemistry. Chemical reviews*, 1992. **92**(7): p. 1487-1508.

175.   Snow, T.P., V. Le Page, Y. Keheyan, and V.M. Bierbaum, *The Interstellar Chemistry of PAH Cations. Nature*, 1998. **391**(6664): p. 259-260.

176.   Sarre, P.J., The Diffuse Interstellar Bands: A Major Problem in Astronomical Spectroscopy. *Journal of Molecular Spectroscopy*, 2006. **238**(1): p. 1-10.

177.   Wenzel, G., C. Joblin, A. Giuliani, S.R. Castillo, G. Mulas, M. Ji, H. Sabbah, S. Quiroga, D. Peña, and L. Nahon, Astrochemical Relevance of VUV Ionization of Large PAH Cations. *Astronomy & Astrophysics*, 2020. **641**: p. A98.

178.   Fox, M.A., The Photoexcited States of Organic Anions. *Chemical Reviews*, 1979. **79**(3): p. 253-273.

179.   Moutet, J.C. and G. Reverdy, Photochemistry of Cation Radicals in Solution: Photoinduced Electron-Transfer Reaction: Oxidation of 1,1-Diarylethylenes. *Chemischer Informationsdienst*, 1983. **14**(27).

180.   Shukla, S.S. and J.F. Rusling, Photoelectrocatalytic Reduction of 4-Chlorobiphenyl Using Anion Radicals and Visible Light. *The Journal of Physical Chemistry*, 1985. **89**(15): p. 3353-3358.

181.   Legros, B., P. Vandereecken, and J.-P. Soumillion, Electron transfer Photoinduced from Naphtholate Anions: Anion Oxidation Potentials and Use of Marcus Free Energy Relationships. *The Journal of Physical Chemistry*, 1991. **95**(12): p. 4752-4761.

182.   Ghosh, I., T. Ghosh, J.I. Bardagi, and B. König, Reduction of Aryl Halides by Consecutive Visible Light-Induced Electron Transfer Processes. *Science*, 2014. **346**(6210): p. 725-728.

183. Christensen, J.A., B.T. Phelan, S. Chaudhuri, A. Acharya, V.S. Batista, and M.R. Wasielewski, Phenothiazine Radical Cation Excited States as Super-Oxidants for Energy-Demanding Reactions. *Journal of the American Chemical Society*, 2018. **140**(15): p. 5290-5299.

184. Marzo, L., S.K. Pagire, O. Reiser, and B. König, Visible-Light Photocatalysis: Does It Make a Difference in Organic Synthesis? *Angewandte Chemie International Edition*, 2018. **57**(32): p. 10034-10072.

185. Lennert, U., P.B. Arockiam, V. Streitferdt, D.J. Scott, C. Rödl, R.M. Gschwind, and R. Wolf, Direct Catalytic Transformation of White Phosphorus into Arylphosphines and Phosphonium Salts. *Nature catalysis*, 2019. **2**(12): p. 1101-1106.

186. Wang, D., F. Loose, P.J. Chirik, and R.R. Knowles, N–H Bond Formation in a Manganese (V) Nitride Yields Ammonia by Light-Driven Proton-Coupled Electron Transfer. *Journal of the American Chemical Society*, 2019. **141**(12): p. 4795-4799.

187. Barham, J.P. and B. König, Synthetic Photoelectrochemistry. *Angewandte Chemie International Edition*, 2020. **59**(29): p. 11732-11747.

188. Cowper, N.G., C.P. Chernowsky, O.P. Williams, and Z.K. Wickens, Potent Reductants via Electron-Primed Photoredox Catalysis: Unlocking Aryl Chlorides for Radical Coupling. *Journal of the American Chemical Society*, 2020. **142**(5): p. 2093-2099.

189.   Glaser, F., C. Kerzig, and O.S. Wenger, Multi-Photon Excitation in Photoredox Catalysis: Concepts, Applications, Methods. *Angewandte Chemie International Edition*, 2020. **59**(26): p. 10266-10284.

190.   Kim, H., H. Kim, T.H. Lambert, and S. Lin, Reductive Electrophotocatalysis: Merging Electricity and Light to Achieve Extreme Reduction Potentials. *Journal of the American Chemical Society*, 2020. **142**(5): p. 2087-2092.

191.   Gumy, J.-C. and E. Vauthey, Investigation of the Excited-State Dynamics of Radical Ions in the Condensed Phase Using the Picosecond Transient Grating Technique. *The Journal of Physical Chemistry A*, 1997. **101**(46): p. 8575-8580.

192.   Brodard, P., A. Sarbach, J.-C. Gumy, T. Bally, and E. Vauthey, Excited-State Dynamics of Organic Radical Ions in Liquids and in Low-Temperature Matrices. *The Journal of Physical Chemistry A*, 2001. **105**(27): p. 6594-6601.

193.   Zhao, L., R. Lian, I.A. Shkrob, R.A. Crowell, S. Pommeret, E.L. Chronister, A.D. Liu, and A.D. Trifunac, Ultrafast Studies on the Photophysics of Matrix-Isolated Radical Cations of Polycyclic Aromatic Hydrocarbons. *The Journal of Physical Chemistry A*, 2004. **108**(1): p. 25-31.

194.   Okhrimenko, A.N., A.V. Gusev, and M.A. Rodgers, Excited State Relaxation Dynamics of the Zinc (II) Tetraphenylporphine Cation Radical. *The Journal of Physical Chemistry A*, 2005. **109**(34): p. 7653-7656.

195.   Grilj, J., E.N. Laricheva, M. Olivucci, and E. Vauthey, Fluorescence of Radical Ions in Liquid Solution: Wurster's Blue as a Case Study. *Angewandte Chemie International Edition*, 2011. **50**(19): p. 4496-4498.

196.   Gosztola, D., M.P. Niemczyk, W. Svec, A.S. Lukas, and M.R. Wasielewski, Excited Doublet States of Electrochemically Generated Aromatic Imide and Diimide Radical Anions. *The Journal of Physical Chemistry A*, 2000. **104**(28): p. 6545-6551.

197.   Lu, C., M. Fujitsuka, A. Sugimoto, and T. Majima, Unprecedented Intramolecular Electron Transfer from Excited Perylenediimide Radical Anion. *The Journal of Physical Chemistry C*, 2016. **120**(23): p. 12734-12741.

198.   Fujitsuka, M., S.S. Kim, C. Lu, S. Tojo, and T. Majima, Intermolecular and Intramolecular Electron Transfer Processes from Excited Naphthalene Diimide Radical Anions. *The Journal of Physical Chemistry B*, 2015. **119**(24): p. 7275-7282.

199.   Fujita, M., A. Ishida, T. Majima, and S. Takamuku, Lifetimes of Radical Anions of Dicyanoanthracene, Phenazine, and Anthraquinone in the Excited State from the Selective Electron-Transfer Quenching. *The Journal of Physical Chemistry*, 1996. **100**(13): p. 5382-5387.

200.   Hall, K.F., M. Boggio-Pasqua, M.J. Bearpark, and M.A. Robb, Photostability via Sloped Conical Intersections: A Computational Study of the Excited States of the Naphthalene Radical Cation. *The Journal of Physical Chemistry A*, 2006. **110**(50): p. 13591-13599.

201.   Tokmachev, A.M., M. Boggio-Pasqua, M.J. Bearpark, and M.A. Robb, Photostability via Sloped Conical Intersections: A Computational Study of the Pyrene Radical Cation. *The Journal of Physical Chemistry A*, 2008. **112**(43): p. 10881-10886.

202.   Tokmachev, A.M., M. Boggio-Pasqua, D. Mendive-Tapia, M.J. Bearpark, and M.A. Robb, Fluorescence of the Perylene Radical Cation and an Inaccessible D/D1 Conical Intersection: An MMVB, RASSCF, and TD-DFT Computational Study. *The Journal of chemical physics*, 2010. **132**(4).

203.   Zinchenko, K.S., F. Ardana-Lamas, I. Seidu, S.P. Neville, J. van der Veen, V.U. Lanfaloni, M.S. Schuurman, and H.J. Wörner, Sub-7-Femtosecond Conical-Intersection Dynamics Probed at the Carbon K-Edge. *Science*, 2021. **371**(6528): p. 489-494.

204.   Herse, C., D. Bas, F.C. Krebs, T. Burgi, J. Weber, T. Wesolowski, B.W. Laursen, and J. Lacour, A Highly Configurationally Stable [4] Heterohelicenium Cation. *Angewandte Chemie International Edition*, 2003. **42**(27): p. 3162-3166.

205.   Mei, L., J. Moutet, S.M. Stull, and T.L. Gianetti, Synthesis of CF3-Containing Spirocyclic Indolines via a Red-Light-Mediated Trifluoromethylation/Dearomatization Cascade. *The Journal of Organic Chemistry*, 2021. **86**(15): p. 10640-10653.

206.   Sørensen, T.J., M.F. Nielsen, and B.W. Laursen, Synthesis and Stability of N, N′-Dialkyl-1, 13-dimethoxyquinacridinium (DMQA+): A [4] Helicene with Multiple Redox States. *ChemPlusChem*, 2014. **79**(7): p. 1030-1035.

207. Shaikh, A.C., J. Moutet, J.M. Veleta, M.M. Hossain, J. Bloch, A.V. Astashkin, and T.L. Gianetti, Persistent, Highly Localized, and Tunable [4] Helicene Radicals. *Chemical Science*, 2020. **11**(40): p. 11060-11067.

208. Weinert, C., B. Wezisla, J. Lindner, and P. Vöhringer, Ultrafast Primary Processes of the Stable Neutral Organic Radical, 1,3,5-triphenylverdazyl, in Liquid Solution. *Physical Chemistry Chemical Physics*, 2015. **17**(20): p. 13659-13671.

209. Li, Q., W. Hou, F. Peng, H. Wang, S. Zhang, D. Dong, S. Wu, and H. Zhang, Photothermal Conversion Performance of Perylene Diimide Radical Anion Salts Modified with Tunable Moieties. *Journal of Materials Science*, 2019. **54**(1): p. 217-227.

210. Teki, Y., Excited-State Dynamics of Non-Luminescent and Luminescent π-Radicals. *Chemistry – A European Journal*, 2020. **26**(5): p. 980-996.

211. Rieth, A.J., M.I. Gonzalez, B. Kudisch, M. Nava, and D.G. Nocera, How Radical Are "Radical" Photocatalysts? A Closed-Shell Meisenheimer Complex Is Identified as a Super-Reducing Photoreagent. *Journal of the American Chemical Society*, 2021. **143**(35): p. 14352-14359.

212. Beckwith, J.S., A. Aster, and E. Vauthey, The Excited-State Dynamics of the Radical Anions of Cyanoanthracenes. *Physical Chemistry Chemical Physics*, 2022. **24**(1): p. 568-577.

213. Renner, R., M. Stolte, J. Heitmüller, T. Brixner, C. Lambert, and F. Würthner, Substituent-Dependent Absorption and Fluorescence Properties of Perylene Bisimide Radical Anions and Dianions. *Materials Horizons*, 2022. **9**(1): p. 350-359.

214. Heitmüller, J., R. Fröhlich, R. Renner, F. Würthner, and T. Brixner, Intersystem Crossing of Perylene Bisimide Neutral, Radical Anion, and Dianion Derivatives Compared via Ultrafast Spectroelectrochemistry. *Physical Chemistry Chemical Physics*, 2023. **25**(26): p. 17214-17229.

215. Wu, S., J. Žurauskas, M. Domański, P.S. Hitzfeld, V. Butera, D.J. Scott, J. Rehbein, A. Kumar, E. Thyrhaug, J. Hauer, and J.P. Barham, Hole-Mediated Photoredox Catalysis: Tris(p-substituted)biarylaminium Radical Cations as Tunable, Precomplexing and Potent Photooxidants. *Organic Chemistry Frontiers*, 2021. **8**(6): p. 1132-1142.

216. Kumar, A., P. Malevich, L. Mewes, S. Wu, J.P. Barham, and J. Hauer, Transient Absorption Spectroscopy Based on Uncompressed Hollow Core Fiber White Light Proves Pre-Association Between a Radical Ion Photocatalyst and Substrate. *The Journal of Chemical Physics*, 2023. **158**(14).

217. Mena, L.D., J.L. Borioni, S. Caby, P. Enders, M.A. Argüello Cordero, F. Fennel, R. Francke, S. Lochbrunner, and J.I. Bardagi, Quantitative Prediction of Excited-State Decay Rates for Radical Anion Photocatalysts. *Chemical Communications*, 2023. **59**(64): p. 9726-9729.